Structural Studies on the Viral Attachment of *Adenoviridae* and *Reoviridae*

DISSERTATION

der Mathematisch-Naturwissenschaftlichen Fakultät
der Eberhard Karls Universität Tübingen
zur Erlangung des Grades eines
Doktors der Naturwissenschaften
(Dr. rer. nat.)

vorgelegt von
M. SC. MICHAEL STREBL
aus Landshut

Tübingen
2022

Gedruckt mit Genehmigung der Mathematisch-Naturwissenschaftlichen Fakultät der Eberhard Karls Universität Tübingen.

Tag der mündlichen Qualifikation: 20.06.2022

Dekan:	Prof. Dr. Thilo Stehle
1. Berichterstatter:	Prof. Dr. Thilo Stehle
2. Berichterstatter:	Prof. Dr. Dirk Schwarzer

Abstract

Viruses are a global threat, causing a large variety of diseases and numerous deaths. Individual viral strains have the ability to emerge rapidly and adapt to the host, hence there is a constant danger, sometimes more in the background of public interest, and sometimes, as at present, more visible. Detailed knowledge about viral spread and proliferation is still limited and as a consequence, research efforts are continuously increasing to tackle this shortage. The attachment of a virus particle to the host cell is the first and as such crucial step during viral replication. Structural biology analysis of the interaction between host cell receptors and viral proteins provides not only a better understanding of the viral tropism, but also possible targets to interfere.

Human adenoviruses (HAdVs) are a wide-spread species of double-stranded DNA viruses that can cause infections in various areas of the body. Depending on the virus type, they bind via the fiber knob (FK) domain to various attachment receptors, for example sialic acid-containing glycans or surface proteins such as CAR or CD46.

One of several HAdVs covered in this thesis is type 56 (HAdV56), which has a low seroprevalence among humans and was shown to require CD46 binding for subsequent infection. Using X-ray crystallography, the atomic structure of the HAdV56 FK was determined and a binding site for sialic acid was confirmed. However, binding of CD46 in comparison to established CD46-binding HAdVs at the respective position is excluded due to significant structural differences, indicating an alternative binding mechanism.

HAdV37 is a cause of epidemic keratoconjunctivitis, a severe infection of the eye. The attachment to the host cell is mediated by sialic acid and can be blocked by trivalent, sialic acid-based inhibitors. In this work, a new generation of inhibitor molecules was, for the first time, fully resolved by X-ray crystallography in complex with the HAdV37 FK. Additionally, binding was confirmed to HAdV26 in structural studies and an adapted version of the inhibitor molecule was shown to bind HAdV36, which expands the potential target range for a medical application.

Orthoreoviruses (ReoVs) are double-stranded RNA viruses that are mostly harmless for humans, but can lead to severe diseases and death in mice. Apart from being a model subject, ReoVs are studied for the targeted treatment of cancer cells. The detailed understanding of the virus-host cell interaction is essential for developing such therapeutics. Recently, the human Nogo receptor-1 (NgR1) was discovered as an

additional attachment factor for ReoVs. In contrast to the well-established receptors sialic acid and JAM-A, NgR1 is not binding to the σ1 spike protein, but to the outer capsid protein σ3. Using cryogenic electron microscopy (cryoEM) analysis, the interaction of an intact virion liganded with NgR1 was structurally characterized. A novel binding mode of one NgR1 protomer in a canyon in between two σ3s was confirmed and two unique interaction areas were identified. This low-affinity but high-avidity binding of a neural receptor with a non-primary attachment capsomer is unique among yet described virus-host interactions and will greatly enhance the understanding of ReoV pathogenesis.

In summary, this work provides novel findings to better understand the host cell attachment of adenoviruses and reoviruses. This will contribute to developing strategies for preventing viral infections and exploiting viruses for therapeutic applications.

Kurzfassung

Viren sind eine globale Bedrohung, welche eine Vielzahl an Erkrankungen und zahlreiche Todesfälle verursachen. Einzelne Virenstämme haben die Fähigkeiten, rapide aufzutreten und sich dem Wirt anzupassen, wodurch eine stete Gefahr lauert, mal mehr im Hintergrund oder, wie in der aktuellen Zeit, sehr prominent in der Öffentlichkeit. Detailliertes Wissen über die Ausbreitung und Vermehrung von Viren ist immer noch nur begrenzt vorhanden, weshalb mehr und mehr Forschung in dieser Richtung betrieben wird. Die Anheftung eines Viruspartikels an die Wirtszelle ist der erste und daher essentielle Schritt in der Replikation von Viren. Die strukturbiologische Analyse der Interaktion von Wirtszellrezeptor und Virusproteinen ermöglicht nicht nur besseres Verständnis für die Ausbreitung von Viren, sondern legt auch mögliche Angriffspunkte offen, um diese zu unterbinden.

Humane Adenoviren (HAdVs) sind eine weit verbreitet Spezies von doppelsträngigen DNA-Viren, die zu Infektionen in verschiedensten Bereichen des Körpers führen können. Je nach Virustyp binden sie mittels der Fiber Knob (FK) Domäne an verschiedene Rezeptoren zur Anheftung an die Wirtszelle, beispielsweise sialinsäurehaltige Glykane oder Oberflächenproteine wie CAR oder CD46.

Einer von mehreren HAdVs innerhalb dieser Arbeit ist Typ 56 (HAdV56), welcher eine niedrige Seroprävalenz beim Menschen aufweist und Bindung an CD46 für eine erfolgreiche Infektion benötigt. Mittels Röntgenstrukturanalyse wurde die atomare Struktur des HAdV56 FK bestimmt und eine Rezeptorbindestelle für Sialinsäure bestätigt. Allerdings ist eine Bindung von CD46 im Vergleich mit etablierten HAdVs, die CD46 binden, an entsprechender Position ausgeschlossen aufgrund signifikanter struktureller Unterschiede, was auf einen alternativen Bindemechanismus hinweist.

HAdV37 ist ein Verursacher von epidemischer Keratokonjunctivitis, einer schweren Augeninfektion. Die Anheftung an die Wirtszelle erfolgt mittels Sialinsäure und kann durch trivalente, Sialinsäure-basierte Inhibitoren verhindert werden. Eine neue Generation an Inhibitormolekülen wurde, im Komplex mit dem HAdV37 FK, erstmals vollständig durch Röntgenkristallographie aufgelöst. Zudem wurde die Bindung an HAdV26 in der Strukturanalyse bestätigt und die Bindung eines angepassten Inhibitormoleküls an HAdV36 gezeigt, wodurch das potentielle Spektrum für die medizinsche Anwendung erweitert wird.

Orthoreoviren (ReoV) sind für den Menschen meist harmlose, doppelsträngige RNA-Viren, die allerdings zu schwerwiegenden Erkrankungen in Mäusen bis hin zum Tod führen können. Neben dem Einsatz als Modellobjekt werden Reoviren zur gezielten Anwendung gegen Krebszellen untersucht. Daher ist ein detailliertes Verständnis der Virus-Wirtszell-Interaktion essentiell für die Entwicklung solcher Medikamente. Kürzlich wurde der humane Nogo receptor-1 (NgR1) als zusätzlicher Anheftungsfaktor für ReoV nachgewiesen. Im Gegensatz zu gut erforschten Rezeptoren wie Sialinsäure und JAM-A bindet NgR1 nicht an das Fiberprotein σ1, sondern an das äußere Kapsidprotein σ3. Mittels Kryoelektronenmikroskopie wurde die Interaktion von intakten Viren mit NgR1 strukturell charakterisiert. Ein neuartiger Bindemechanismus, bei welchem ein NgR1 Protomer in einer Kluft zwischen zwei σ3 Einheiten bindet, wurde bestätigt und zwei spezifische Interaktionsbereiche identifiziert. Die Bindung zwischen einem neuralen Rezeptor und einem nicht-primären Anheftungskapsomer mit niedriger Affinität, aber großer Avidität, ist einzigartig unter den Virus-Wirt Interaktionen, die bis heute charakterisiert sind, und werden das Verständnis von reoviraler Krankheitsentwicklung deutlich verbessern.

Zusammenfassend liefert diese Arbeit neue Erkentnisse für ein besseres Verständnis der Anheftungsmechanismen von Adenoviren und Reoviren. Diese werden dazu beitragen, geeignete Strategien zur Verhinderung viraler Infektionen zu entwickeln und Viren für therapeutische Anwendungen zu nutzen.

Abbreviations

3'SL	3'Sialyllactose
4-O-Ac-3'SL	4-O-acetyl-3'sialyllactose
6'SL	6'Sialyllactose
ACE2	Angiotensin-converting Enzyme 2
CAR	Coxsackie and Adenovirus Receptor
CD46	Cluster of Differentiation 46
CoV	Coronavirus
cryoEM	Cryogenic Electron Microscopy
CTF	Contrast Transfer Function
CV	Column Volumes
DMP	Dimethyl Pimelimidate
DMS	Dimethyl Suberimidate
DNA	Deoxyribonucleic Acid
dNTPs	Deoxynucleoside Triphosphate
ds	Double-stranded
DSG	Desmoglein-2
DTT	Dithiothreitol
EDC	1-Ethyl-3-(3-Dimethylaminopropyl)Carbodiimide Hydrochloride
EDTA	Ethylendiamintetraacetic Acid
EKC	Epidemic Keratoconjunctivitis
FBS	Fetal Bovine Serum
Fc	Fragment Crystallizable
FK	Fiber Knob
GAG	Glycosaminoglycans
GalNAc	*N*-acetylgalactosamine
HAdV	Human Adenovirus
HBGA	Histo-blood Group Antigen
HEPES	4-(2-Hydroxyethyl)-1-Piperazineethanesulfonic Acid
HIC	Hydrophobic Interaction Chromatography
HIV	Human Immunodeficiency Virus
ICTV	International Committee on Taxonomy of Viruses
IEX	Ion Exchange Chromatography
IMAC	Immobilized Metal Affinity Chromatography
IPTG	Isopropyl β-D-1-Thiogalactopyranoside
JAM-A	Junctional Adhesion Molecule A
kDa	Kilodalton
kb	Kilobase Pairs

LRR	Leucine-rich Repeat
mAB	Monoclonal Antibody
MCS	Multiple Cloning Site
MERS-CoV	Middle East Respiratory Syndrome-related Coronavirus
MES	2-N-Morpholino)Ethanesulfonic Acid
MOI	Multiplicity Of Infection
MPD	2-Methyl-2,4-pentanediol
mRNA	Messenger RNA
MW	Molecular Weight
MWCO	Molecular Weight Cutoff
NCS	Non-Crystallographic Symmetry
Neu5Ac	*N*-acetylneuraminic Acid
NgR1	Nogo Receptor-1
NHS	*N*-hydroxysuccinimide
NTA	Nitrilotriacetic Acid
OD	Optical Density
PBS	Phosphate-buffered Saline
PCR	Polymerase Chain Reaction
PDB	Protein Data Bank
PEI	Polyethylenimine
pfu	Plaque Forming Units
P/S	Penicillin/Streptomycin
PVDF	Polyvinylidene Difluoride
ReoV	Mammalian Orthoreovirus
RFU	Relative Fluorescence Unit
RMSD	Root Mean Square Deviation
RNA	Ribonucleic Acid
rpm	Rounds Per Minute
RT	Room Temperature
SARS	Severe Acute Respiratory Syndrome
SDS-PAGE	Sodium Dodecyl Sulphate-Polyacrylamide Gel Electrophoresis
SEC	Size Exclusion Chromatography
SEM	Scanning Electron Microscopy
SFM	Serum Free Medium
SLS	Swiss Light Source
SPA	Single Particle Analysis
SPR	Surface Plasmon Resonance Spectroscopy
ss	Single-stranded
TAE	Tris Base, Acetic Acid and EDTA
TBS	Tris-buffered Saline
TEM	Transmission Electron Microscopy
TMV	Tobacco Mosaic Virus
WHO	World Health Organisation
X-Gal	5-Bromo-4-Chloro-3-Indolyl-β-D-Galactopyranoside

Contents

Abstract **iii**

Kurzfassung **v**

Abbreviations **vii**

1 Introduction **1**

1.1 A Brief History of Virology 1

1.2 Definition and Classification of Viruses 3

1.3 Siblings in Crime - Similarities and Differences between *Adenoviruses* and *Reoviruses* 5

1.3.1 Genome & Capsid Structure 5

1.3.2 Viral Replication Cycle 8

1.3.3 Tropism and Diseases 11

1.4 Viral Attachment Factors 12

1.4.1 Attachment Factors of *Adenoviridae* 12

1.4.2 Attachment Factors of *Reoviridae* 15

1.5 Structural Biology Approaches 18

1.5.1 X-ray Crystallography 18

1.5.2 Cryogenic Electron Microscopy 20

1.5.3 Advantages and Drawbacks of Each Approach 22

1.6 Why Do We Need Structural Virology? 24

2 Objectives **26**

3 Materials & Methods **27**

3.1 Materials 27

3.1.1 Chemicals 27

3.1.2 Bacterial Strains . . . 27
3.1.3 Cell Lines . . . 27
3.1.4 Plasmids . . . 28
3.1.5 Buffers . . . 28
3.1.6 Commercial Crystallization Screens . . . 31
3.2 Methods . . . 32
3.2.1 Molecular Biology . . . 32
3.2.2 Cell Culture . . . 35
3.2.3 Protein Biochemistry . . . 37
3.2.4 X-ray Crystallography . . . 43
3.2.5 Cryogenic Electron Microscopy . . . 45

4 Structural Analysis of HAdV56 FK Binding Sites for CD46 and Sialic Acid 47
4.1 Results . . . 47
4.1.1 Purification of HAdV56 Fiber Knob . . . 47
4.1.2 Crystallization and Structure Determination . . . 48
4.1.3 Structural Analysis of the Putative CD46 Binding Site . . . 49
4.1.4 Structural Analysis of the Sialic Acid Binding Site . . . 51
4.2 Discussion . . . 53
4.2.1 HAdV56 FK Does Not Bind CD46 . . . 53
4.2.2 CD46 Interaction is Mediated by the HAdV56 Hexon . . . 53
4.2.3 Novelty of a Second Attachment Receptor Binding Site . . . 55

5 Adapting Trivalent Sialic Acid Inhibitors to HAdV37, HAdV36, and HAdV26 56
5.1 Results . . . 56
5.1.1 Crystallization, Data Collection, and Data Processing . . . 58
5.1.1.1 Crystallization of HAdV37 FK . . . 58
5.1.1.2 Crystallization of HAdV36 FK . . . 58
5.1.1.3 Crystallization of HAdV26 FK . . . 59
5.1.2 Structures of C2-linked Inhibitors . . . 59
5.1.3 Structures of C4-linked Inhibitors . . . 61
5.1.4 Steric Influence of the Linker Switch . . . 62
5.1.5 Zinc Chelating Ability of ME1146 . . . 64

5.2 Discussion . . . 66
5.2.1 Structural Comparison of the Inhibitor Binding Modes . . . 66
5.2.2 Biological Inhibition Efficacy Depends on HAdV Type . . . 67
5.2.3 Zinc Binding . . . 70

6 Novel Binding Mode of the Neural Receptor NgR1 to the Reovirus Capsid 71
6.1 Results . . . 71
6.1.1 Purification of NgR1 . . . 71
6.1.1.1 Purification of His-tagged NgR1 . . . 71
6.1.1.2 Purification of Fc-tagged NgR1 . . . 72
6.1.1.3 Glycoslation of NgR1 . . . 73
6.1.2 Purification of $\mu1_3\sigma3_3$ . . . 73
6.1.3 Attempts to Obtain a NgR1 and $\mu1_3\sigma3_3$ Complex . . . 75
6.1.3.1 Gel Filtration . . . 75
6.1.3.2 Pulldown Assays . . . 77
6.1.3.3 Crosslinking Assays . . . 78
6.1.3.4 Surface Plasmon Resonance Spectroscopy . . . 79
6.1.4 CryoEM Analysis of ReoV T3D Virion in Complex with NgR1 80
6.1.4.1 CryoEM Data Processing . . . 80
6.1.4.2 Molecular Docking in Asymmetric Unit . . . 82
6.1.4.3 NgR1 Features in Difference Density Map . . . 84
6.1.4.4 NgR1 Arrangement on ReoV Capsid . . . 84
6.1.4.5 Binding Interfaces of NgR1 and σ3 . . . 86
6.2 Discussion . . . 86
6.2.1 Protein Purification and Analysis . . . 86
6.2.2 Challenges at Protein-based Complex Formation . . . 87
6.2.3 CryoEM Data Processing and Refinement . . . 88
6.2.4 Structural Analysis of the 3D Reconstructions . . . 89
6.2.5 Concave and Convex NgR1 Binding Interfaces . . . 90

7 Conclusion 95

Bibliography 97

List of Tables 115

List of Figures **117**

Acknowledgments **119**

Appendix **121**

Publications and Unpublished Manuscripts **129**

1. Introduction

1.1 A Brief History of Virology

The documented history of viruses since their discovery is rather short compared to that of their potential hosts: Barely 130 years ago, Dmitri Iwanowski in 1892 and Martinus Beijerinck in 1898 discovered independently of each other a ”contagium vivum fluidum”, a ”contagious living fluid”. It was still capable of infecting proliferating tobacco plant cells, although being filtered in advance [1, 2]. At that time, they did not realize what they had just discovered, but nowadays this pathogen is known as *tobacco mosaic virus* (TMV), a much-studied model virus. The first ”contagium vivum fluidum” infecting humans was described by Walter Reed in 1901 [3]. It was the *yellow fever virus*, which is transmitted by mosquitoes and hence spatially limited to the tropical regions of Africa and South America [4]. Félix d'Herelle, who later on discovered bacteriophages, concluded in early plaque assays that viruses are neither fluids nor a chemical substance causing the disease. The virus-containing sample formed colonies of dead cells on an agar plate in these assays instead of an evenly distributed layer in a concentration-dependent manner [5]. Later in 1935, Wendell Stanley was able to generate TMV crystals and discovered that they consisted mostly of proteins, thereby confirming the particular composition of viruses [6]. The invention of the electron microscope by Ernst Ruska and Max Knoll [7], also called ”Übermikroskop” at that time, enabled the first visualization of a virus and a more precise determination of size, shape, and appearance of the TMV [8].

Viruses have been a major cause of pandemics and death throughout history. During the great influenza pandemic of 1918–1919, 500 million people or one third of the world's population were infected, causing 25–100 million deaths [9]. Formerly called ”Spanish flu”, the disease occurred in three waves within a short 12-month period and affected an unusually large number of young adults between 20 and 40 years of age compared with previous and also future influenza pandemics. The first isolation of the human influenza virus was described in 1933 [10]. Since then, several strains have

emerged from the 1918 subtype A/H1N1 by recombination of the hemagglutinin (H) and neuraminidase (N) encoding genes [11]. In the absence of preexisting immunity to the new subtypes, influenza viruses have caused several outbreaks, for example in Asia (1957–1958), Hongkong (1968–1969) [12], Russia (1977) [13], and also the global swine flu in 2009 [14]. Advances in virology and drug discovery have led to the availability of potent influenza vaccines today. However, due to the frequent recombination of the subtypes, the vaccine is revised twice a year by the World Health Organization (WHO) to match the currently circulating influenza strains, and annual vaccine boosters are required [15].

In the second half of the 20$^{\text{th}}$ century the *human immunodeficiency virus* (HIV) has become a major threat and cause of morbidity worldwide. Currently there are 37 million people estimated to be infected and an equal number have died of HIV since the start of the pandemic [16]. The first known HIV infection was retroactively dated to 1959 in Léopoldsville, nowadays Kinshasa, Democratic Republic of Congo [17]. It became more widely known in 1981, with several reported cases of atypical pneumonia among homosexual men in California [18, 19, 20]. Soon after the number of cases increased, HIV was firstly isolated in 1983 by Barré-Sinoissi and Montagnier [21], who were later awarded with the Nobel Prize. Robert Gallo confirmed their findings one year later [22]. Only a few more years later in 1987, the first antiretroviral drug Zidovudine, a nucleoside analog reverse-transcriptase inhibitor synthesized by Jerome Horwitz, was approved as treatment for HIV in the USA [23]. Scientific advances have eventually led to combinatorial antiretroviral drugs that tackle multiple steps in the viral replication cycle. Combining several drugs reduces the risk of resistant mutants, increases efficacy and results in long-lasting suppression of viral proliferation [16].

In the past two decades, there have been several other viral outbreaks that have shaken the world: The severe acute respiratory syndrome coronavirus (SARS-CoV-1) outbreak in 2002 (8,096 reported cases in 27 countries [24]), the 2012 Middle East respiratory syndrome-related coronavrius (MERS-CoV) outbreak (1,728 cases and 624 deaths [24]), the Western African Ebola virus epidemic (2013–2016 in West Africa with $\sim$28,000 infections and $\sim$11,000 deaths [25] and 2018–2020 in Kongo and Uganda with $\sim$3,500 cases and $\sim$2,200 deaths [26]), and the 2015–2016 Zika virus epidemic (predominantly in Brazil with 220,200 confirmed cases and severe defects in form of microcephaly in newborns [27, 28]). All of this culminate in the still ongoing and unprecedented Covid-19 pandemic. What all these outbreaks share is the cross-species transition from animals

to humans. This makes these emerging viruses not only difficult to predict, but also dangerous, as there is no existing immunity to known and similar pathogens [29].

Interestingly, the first successful attempt to combat a virus-borne disease was reported long before the discovery of viruses themselves, by Edward Jenner in 1796: he recognized that convalescents of cowpox were significantly less susceptible to smallpox. To test his hypothesis, he infected a young boy with cowpox (from an infected milkmaid) and later with smallpox. The boy survived and was the first person to be inoculated with "Variolae Vaccinae" ("smallpox of the cow"), which gave rise to the term vaccination [30]. It took more than 100 years until Louis Pasteur developed the rabies vaccine from live attenuated virus from rabbits and cured the 9-year old Joseph Meister post-exposure [31].

The advancement of cell culture techniques facilitated working with pathogens *in vitro*, for example with the human poliovirus in 1949 [32]). Starting with a living, attenuated virus polio vaccine in 1950 [33], moving to an inactive virus in 1955 [34, 35], a very effective live oral vaccine was developed by Albert Sabin in 1961 [36]. Unlike previous vaccines, the oral vaccine prevents the poliovirus from replicating in the intestine, thus inhibiting transmission to non-immunized individuals [35]. Continuous research and global vaccination efforts have succeeded in nearly eradicating wildtype polio, which is now endemic in Afghanistan and Pakistan only [37, 38], and completely eradicating smallpox [39]. To fight the current Covid-19 pandemic, several vaccines have been developed at an unparalleled pace from Biontech/Pfizer [40], Moderna [41], Johnson&Johnson [42], and AstraZeneca [43].

1.2 Definition and Classification of Viruses

A virus is generally not considered a living organism and there are a few properties distinguishing it from other small biologically active agents such as viroids and prions: Viruses are infectious, intracellular parasites with their own genome (either RNA or DNA) and a protein shell (capsid), but they are absolutely dependent on a host organism for proliferation. An appropriate host is required for genome replication and the synthesis of all viral components, which are necessary for the assembly of a new infectious viral particle, called a virion. The progeny virion is released from the host and transmitted to a new one. After cell entry and particle disassembly, a new infectious cycle starts [44].

As more and more viruses were discovered by the 1960s, the International Committee on Taxonomy of Viruses (ICTV) was founded in 1966, then called International Committee on Nomenclature of Viruses, aiming for a consistent nomenclature and classification of viruses [45]. A hierarchical scheme from realm to species was established (based on [46]) using four main criteria: (i) the nucleic acid type, (ii) the capsid symmetry, (iii) the presence of an enveloped or non-enveloped capsid, (iv) and the dimension of the virus particle [44]. The current ICTV Report on Virus Classification and Taxon Nomenclature covers 6 realms, 39 classes, 189 families, 2,224 genera, and 9,110 viral species [47, 48].

The second common scheme is the Baltimore classification, developed by Nobel Prize winner David Baltimore, which is based on the mode of mRNA synthesis [49, 50]. This is directly related to the genome type of the virus in question, i.e. DNA or RNA, double-stranded or single-stranded, the sense of single-stranded genome, and whether a reverse-transcribed intermediate is involved in replication. This results in seven classes of viruses, which are listed in Table 1. However, both classification systems are not mutually exclusive, but complement each other quite well.

Table 1) Baltimore classification of viruses

Class	Genome
I	dsDNA
II	ssDNA
III	dsRNA
IV	(+)ssRNA
V	(-)ssDNA
VI	ssRNA-RT
VII	dsDNA-RT

The first family of viruses covered in this thesis is the *Adenoviridae* family, a Baltimore class 1 dsDNA virus of the realm *Varidnaviria* and the class of *Tectiliciricetes* [47], which was first isolated almost 70 years ago [51]. All human adenoviruses belong to the genus *Mastadenovirus* and are grouped into seven species A–G, based on neutralization data as well as genomic analysis. At present, 113 types are known (see Table 2), of which 80 are assigned to species D, including Human Adenovirus 26 (HAdV26), Human Adenovirus 36 (HAdV36), Human Adenovirus 37 (HAdV37) and Human Adenovirus 56 (HAdV56), which will all be covered in this thesis [52].

Table 2) Human adenovirus types

Species	Serotype
A	12, 18, 31, 61
B	3, 7, 11, 14, 16, 21, 34, 35, 50, 55, 66, 68, 76–79, 106
C	1, 2, 5, 6, 57, 89, 104, 108
D	8–10, 13, 15, 17, 19, 20, 22–30, 32, 33, 36–39, 42–49, 51, 53, 54, 56, 58–60, 62–65, 67, 69–75, 80–88, 90–103, 105, 107, 109–113
E	4
F	40, 41
G	52

The second virus family of interest in this thesis, the *Reoviridae*, is a dsRNA virus of the Baltimore class III viral family and belongs to the realm of *Riboviria* and the class

of *Resentoviricetes* [47]. It is divided into two subfamilies, one having a smooth particle surface (*Sedoreovirinae*), while the other has turrets or spikes on the 12-fold vertices (*Spinareovirinae*). The latter contains the *Orthoreoviruses*, a genus only infecting vertebrates, including humans through the species *mammalian Orthoreovirus* (ReoV). Three major serotypes with various isolates have been classified according to hemagglutination and antibody neutralization properties: Type 1 Lang (T1L), type 2 Jones (T2J), and type 3 Dearing (T3D). A fourth minor serotype isolated from mouse was added based on its sequence similarity: Type 4 Ndelle [53]. The serotypes mainly differ in the σ1 sequence, which greatly influences their tropism [54, 55].

1.3 Siblings in Crime - Similarities and Differences between *Adenoviruses* and *Reoviruses*

At first glance, *Adenoviruses* and *Reoviruses* differ in various aspects, such as genome organization, tropism, related diseases, and danger to humans. Despite belonging to different virus families, even a different class and realm, they share a very similar capsid structure as well as a strikingly comparable attachment strategy to infect host cells, which will be discussed in the following sections.

1.3.1 Genome & Capsid Structure

Human Adenoviruses have a linear, double-stranded DNA genome of ca. 35 kb encoding 37–39 proteins, depending on the species [56]. In species D, most of the genes exhibit a high nucleotide conservation, while the major structural proteins hexon, penton base and fiber are far more diverse due to homologous recombination, which is also the main distinguishing criteria between different HAdV types [57]. The icosahedral symmetry of the capsid makes $\frac{1}{60}$ of the protein shell sufficient to describe the whole virus using five-, three-, and two-fold rotational symmetry axes [58]. Most of the capsid is covered by 240 hexon trimers, complemented by 12 pentameric penton bases at the vertices, and as many trimeric fibers, which are protruding from the vertices (see Figure 1 A). This gives the HAdV capsid a pseudo T=25 icosahedral symmetry [59, 60] and a diameter of 89 nm without the fibers [61]. The fiber is thereby the most important capsid component for viral attachment, and it is divided into the tail, which interacts with the penton base,

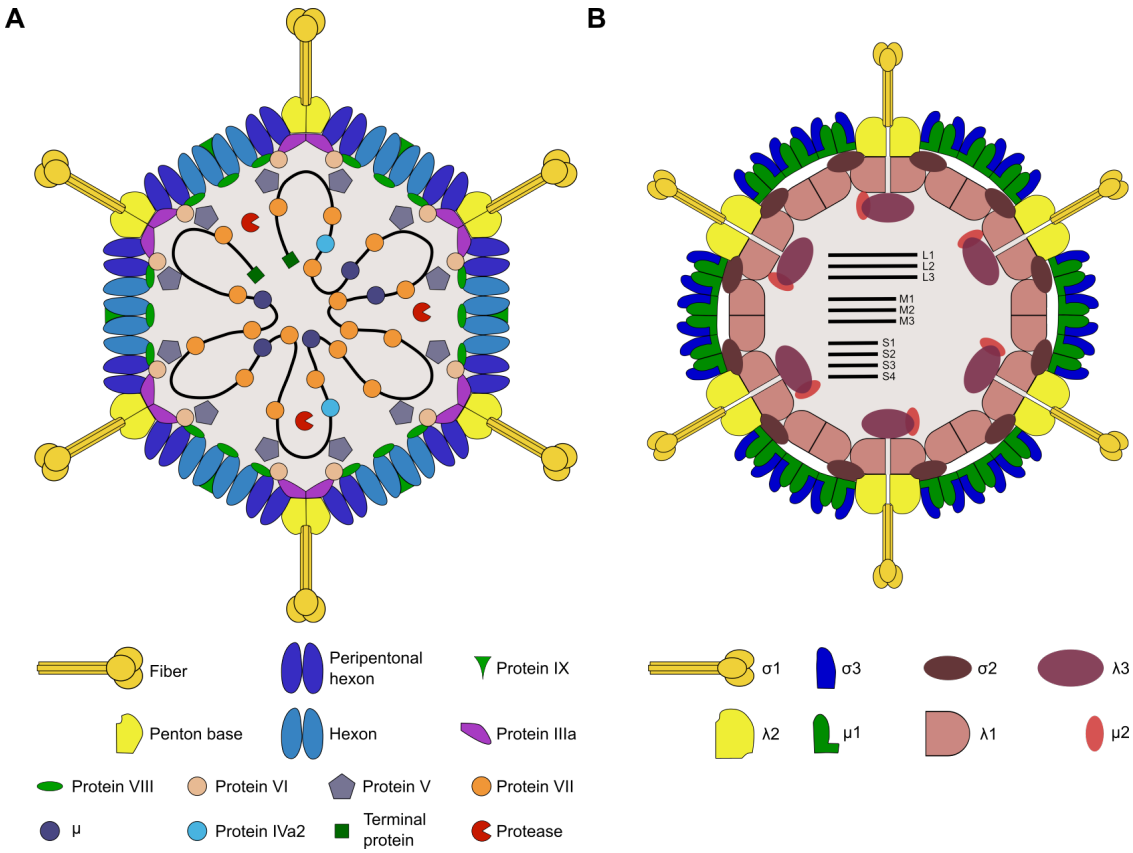

Figure 1) **Overview of ReoV and HAdV capsid structures. A:** Scheme of the HAdV capsid adapted from Rafie et al. [66] and ViralZone [67]. **B:** Scheme of the ReoV capsid adapted from ViralZone [68].

a long shaft, and the knob domain, which can bind various attachment receptors (see subsection 1.4.1). The shaft contains a varying number of β-spiral repeats that define the length of the fiber ranging from 13–33 nm [62]. After the third β-spiral repeat, a 2–4 residue insertion allows the fiber to bend, which might facilitate receptor engagement. However, fibers of species D HAdVs lack the ability to bend, making them very rigid.

Interestingly, there is a symmetry mismatch between the five-fold symmetric penton base and the three-fold symmetric fiber tail. The penton base has five grooves in between monomers for interacting with the fiber tail N'-termini, which was shown by crystal complex structures of the penton base with peptides of the tail's N'-terminus [63]. However, only three out of the five grooves can be occupied at the same time by the trimeric fiber tail, presumably in a configuration where two N'-termini bind in adjacent grooves, while the third binding groove is separated by one unoccupied groove each [64, 65].

Further minor capsid proteins are stabilizing the interaction of the penton base with the peripentonal hexons (protein IIIa) or the hexon assembly, either on the outer surface (protein IX) or from the inside (proteins VI and VIII), and are thus completing the viral capsid [66, 69]. The core proteins IVa2, V, VII, μ, and the terminal protein are involved in complexing the DNA genome and protein V connects the genome to the capsid via interaction with protein VI (shown for HAdV41 [66]) [70]. Additionally, a cysteine protease is encoded in the viral genome for processing precursor proteins [56].

The *mammalian Orthoreovirus* has a double-stranded RNA genome of ca. 24 kb comprising ten linear segments, which are named according to their size: L(arge), M(edium), and S(mall). Each of the segments encodes for one protein, except S1, which encodes for two proteins in different reading frames [44]. Among non-mammalian reoviruses, the number of RNA segments can vary from 9–12 [53]. The capsid, which has a diameter of 80 nm without spikes, consists of two layers: the inner core, which has T=1 symmetry and contains the genome, and the outer capsid, which has T=13 symmetry [53, 71]. The core with an internal diameter of 50–60 nm is mainly formed by the main core shell protein λ1 as well as λ3, σ2, and μ2. Apart from its structural importance, λ3 is an RNA-dependent RNA polymerase, which forms the transcribing enzyme complex together with the nucleoside triphosphatase and helicase μ2. The vertices of the capsid are built of λ2, which forms pentamers and is a guanylyl transferase involved in mRNA capping. Despite being actually an outer capsid protein, it is still associated with the core, thus connecting both shells. The remaining outer capsid is formed by μ1, which is also required for subsequent core penetration, and the capping protein σ3 on top. Both μ1 and σ3 assemble to a hexameric complex, the $\mu1_3\sigma3_3$ heterohexamer [72]. The trimeric spike protein σ1 protrudes from the vertices and is a crucial factor for host cell attachment. It can undergo major structural changes during viral disassembly from a compact form in virions to an extended conformation in ISVPs [71, 73]. Fully extended σ1 protrudes up to 40 nm from the viral capsid according to EM images [74]. However, the exact mechanism of these structural rearrangements is still not fully understood [75].

Both HAdV and ReoV share striking similarities. The outer capsid architecture is amazingly similar in both viruses, not only due to the icosahedral symmetry. The most frequent capsomer is a three-fold symmetric protein complex, covering the majority of the outer capsid surface. Both exhibit a five-fold to three-fold symmetry mismatch from

the pentameric vertex to the spike protein. While structural data, describing local one-on-one interactions with peptide fragments, have been available for HAdV for several years [63], this potential interaction pattern for ReoV has only recently been determined by asymmetric, sub-particle cryoEM reconstruction of this area [76]. Also, the spike proteins have a very similar domain organization with the globular head, respective knob domain, the body, respective shaft, and the tail domain. Both σ1 head and FK domain are crucial for host cell attachment and are structurally alike. They consist of eight antiparallel β-strands, which circularize to form a β-barrel at the σ1 head, while the HAdV FK has two opposing β-sheets. The topology of the individual β-strands is the same for both viruses. The HAdV FK is slightly larger (ca. 30 amino acids) due to longer loops and a more elaborated loop structure. These loops are the major determinant of receptor binding, and are discussed in more detail in section 1.4. Below the attachment domains, both spikes have a somewhat flexible hinge region, which allows movement of the head/knob domain versus the body/shaft domain [77]. While the σ1 body is formed of β-spiral repeats followed by a long α-helical coiled-coil tail, the whole HAdV shaft and tail consists of a varying number of β-spiral repeats, from six (HAdV3) to 21 (HAdV5) [64, 78, 79].

1.3.2 Viral Replication Cycle

The viral propagation and replication can be summarized in three fundamental principles according to *Principles of Virology*[1]:

- All viral genomes are packed inside particles that mediate their transmission from host to host.
- The viral genome contains the information for initiating and completing infectious cycle within a susceptible, permissive cell. An infectious cycle includes attachment and entry of the particle, decoding of the genome information, translation of viral mRNA by host ribosomes, genome replication, and assembly and release of particles containing the genome.
- All viruses are able to establish themselves in a host population so that virus survival is ensured.

[1] *Principles of Virology: Molecular Biology, Pathogenisis, and Control of Animal Viruses.* S. J. Flint, L. W. Enquist, V. R. Rancaniello, and A. M. Skalka (2004), American Society for Microbiology, second edition; p. 21

However, within these boundaries the individual strategies of different viruses are rather diverse. In the following, the replication cycles of adenoviruses and reoviruses will be elucidated briefly.

Adenovirus Replication Cycle

Human adenoviruses rely on clathrin-dependent endocytosis to infiltrate the host cell. Several uncoating steps of the viral capsid are required until the genomic DNA is released into the nucleus. Initial attachment of the viral capsid to the host cell surface is mediated by various receptors binding to the fiber knob domain (see subsection 1.4.1). To initiate entry of the virus into the cell, additional interactions between the penton base via a conserved motif of the three amino acids arginine, glycine, and apsartate, called RGD motif, to the $\alpha v\beta 3$ or $\alpha v\beta 5$ integrin is required [80, 81]. Integrin binding presumably induces subtle conformational changes in the vertex region, which lead to an untwisting of the penton base out of the viral capsid, and hence softening of the vertex region [80, 82]. This facilitates the shedding of the vertex proteins, which is mechanically induced by drifting of attachment receptors along the cell membrane, thus pulling the fiber out of the vertex [83]. After removal of fiber, penton base and peripentonal hexons from the capsid [84, 85], the membrane lytic protein VI is able to dissociate from the inside of the capsid [85, 86]. The initially limited exposure of protein VI leads to small lesions or pores in the plasma membrane, which triggers lysosomal exocytosis to repair the lesions. Subsequent secretion of acid sphingomyelinase increases the ceramide lipid level, which enhances clathrin-dependent endocytosis and thus the uptake of the capsid into endosomes. [87, 88]. Upon further disassembly of the capsid, more protein VI is released into the endosome, binds to the endosomal membrane, and leads to a subsequent rupture of the endosome. The remainder of the viral capsid is released into the cytoplasm. Interestingly, the protein VI lytic activity is pH independent and thus does not require acidification of the endosome for subsequent lysis [85].

The remainder of the capsid is transported to the core via microtubules. Dynein binds to the hexon via the dynein intermediate chain (IC) and light intermediate chain 1 (LIC1) for transport [89] and docks onto the nuclear pore complex (NPC) [90]. The Kinesin heavy chain 5C (Kif5C) is tethered to the capsid by the Kinesin light chain 1 (Klc1), which binds to protein IX. Upon activation of Kif5C, a motor movement along the microtubules is ongoing and a pulling force disassembles the capsid [91, 92]. Protein

VII, which still binds to the genomic DNA, contains a nuclear localization signal (NLS) and is recognized by e.g. importin α, importin β, importin 7 [93], and transportin [94] for import into the nucleus. Furthermore, protein VII functions as protection of the viral DNA from double-strand break repair [95]. After nuclear import, which lasted for approximately 30 min beginning from the attachment [44], the viral transcription begins. New virus particles are assembled in the nucleus, where also the viral DNA is synthesized. All structural proteins are transported from the cytoplasm to the nucleus, where new particles mature and subsequently cluster together [96]. After nuclear and plasma membrane rupture, the virus particles are released to infect further cells [97, 98].

Reovirus Replication Cycle

The ReoV cell entry mechanism is, similar to HAdVs, based on clathrin-dependent endocytosis [99, 100]. The attachment is mediated by multiple receptor interactions: First, sialic acid is recognized with low-affinity, enabling subsequent lateral diffusion on the cell surface, until junctional adhesion molecule A (JAM-A) is reached and recognized with higher affinity (details see subsection 1.4.2) [75, 101, 102]. Afterwards, binding to a β1 integrin is required for internalization into endosomes [103]. In the endocytic compartment, a transition of the virion to an infectious subviral particle (ISVP) takes place: σ3 is removed proteolytically, autocleavage turns μ1 into μ1N and μ1C, and σ1 changes its conformation from a compact form to an extended fiber [104, 105]. In ISVPs, μ1C is further processed by proteases (e.g. trypsin or chymotrypsin) to δ and φ, which is thought to be involved in membrane penetration afterwards [106]. At the same time, σ1 is removed from the remaining capsid to generate activated ISVP* particles. The ISVP*s induce endosomal membrane penetration and, along with a loss μ1, the core particle is released from the endosome, followed by activation of transcription. The replication and assembly of virus particles happens in special intracellular compartments, the viral factories. In a first round of transcription, ssRNA is generated for each viral gene fragment. This is used as a template for minus-strand synthesis to generate the genomic dsRNA. A second round of transcription is necessary for subsequent viral protein synthesis to assemble the virus particle [107]. Upon release of the μ1 φ fragment to the cytosol, cell death by apoptosis is triggered and the viral particles can exit the cell [108]. However, viral release is also possible in a non-lytic manner, depending on the type of infected cell [109].

1.3.3 Tropism and Diseases

HAdVs show a very broad tropism, disease, and receptor spectrum that is specific for each serotype. Usually, infections of the gastrointestinal tract are mainly caused by species F and G, of the respiratory tract by species B, D, and E, and of the ocular tract by species B, D, and E, leading to conjunctivitis [110]. Most infections happen during early childhood, but HAdVs can persist in a latent state [110, 111]. Some HAdVs can be clearly associated with specific diseases: HAdV8, HAdV19, and HAdV37 cause a severe ocular infection, epidemic keratoconjunctivitis (EKC) [112] and use sialic acid as main attachment receptor [113]. More recently, HAdV53 [114], HAdV54 [115], and HAdV56 [116] were also found to be a causative agent of EKC, while the latter can also lead to pneumonia in newborns. Species F HAdV40 and HAdV41 are related to the gastroenteric tract, causing diarrhea especially in children [44, 66]. Along with species G HAdV52, they are the only HAdVs with two fibers of different length, which could be the reason for their different tissue tropism [117, 118, 119]. Species B HAdV serotypes 11, 34, and 35 can cause renal infections, which are potentially fatal for immunocompromised patients [120]. For other HAdVs, the specific role in disease mechanisms is not fully evident yet. HAdV36 could be linked to obesity in several mammalian species and was also detected in human adipose tissue, but the receptor specificity is still unknown [121, 122, 123].

The name ”reovirus” is derived from ”respiratory - enteric - orphan”, the putative sites of infection as well as the misbelief that it is unrelated to any disease [124]. While clinical symptoms of ReoV infections in humans are rarely severe, it can cause lethal diseases in many mammalian species, for example young mice [125]. ReoV transmission mainly occurs via oral-fecal routes [126]. The primary infection site is the intestinal epithelium and lymphoid tissue [127, 128]. ReoV uptake by intestinal M cells is followed by primary replication in lymphoid tissue of Peyer’s patches [127]. In the course of an infection, the virus spreads into the central nervous system (CNS) of mice, although via different routes depending on the serotype: T1L spreads hematogeneously into the CNS and infects ependymal cells [129, 130], resulting in hydrocephalus [131], while T3D spreads into the CNS via neural routes and infects neurons, causing lethal encephalitis. This difference in preferred transmission route is linked to σ1, as T1L σ1 preferentially binds to ependymal cells [132], while T3D σ1 prefers neuronal cells [133]. Interestingly, the non-sialic acid binding variant T1L SA- induces far less severe hydrocephalus compared to T1L SA+, although reaching similar titers in the brain, maybe due to reduced

transmission capabilities through brain vesicles [134]. A similar effect is seen for T3D SA- compared to T3D SA+ [135]. One possible explanation is that sialic acid binding enhances the replication kinetics at the primary infection site. This goes along with the finding that T3D SA+ has a much higher viral yield at one replication cycle in HeLa cells compared to T3D SA- [136] and induces more apoptosis [137]. In animal models, ReoV showed symptoms of biliary inflammation, pneumonia, hydrocephalus, myocarditis, meningitis, and encephalitis [125, 138]. Only recently, ReoV was also linked to the loss of tolerance for dietary gluten and triggering celiac disease [139].

1.4 Viral Attachment Factors

The major attachment proteins of ReoV and HAdV are the top domains of the spike proteins, the σ1 head and the fiber knob (FK), respectively. Several crystal structures and cryoEM reconstructions are available, describing the interaction at atomic resolution. The most important data will be summarized in the following sections.

1.4.1 Attachment Factors of *Adenoviridae*

Due to the large number of HAdV serotypes, far more attachment receptors are known and characterized compared to ReoV. All of the interactions published so far involve the FK domain, but interestingly the interaction areas are distributed all over the FK surface (see Figure 2). The FK is a symmetric homotrimer, wherein each monomer consists of an eight-stranded antiparallel β-sandwich comprising of two β-sheets each [140, 141]. The connecting loops are the main determinants of the FK surface and thus define receptor binding. Various cell surface protein receptors bind to the HAdV FK domain, for example the coxsackie and adenovirus receptor (CAR) [142], CD46 or Desmoglein-2 (DSG2).

CAR, which is a member of the JAM family and mediates cell-cell adhesion [141], is engaged by species A, C, D, E, and F HAdVs. Structural data are available for CAR bound to HAdV12 [143] and HAdV37 [144]. Both show a comparable binding mode at the side of the FK trimer in between two adjacent monomers. CAR itself consists of two IgV-like domains [145], however only the D1 domain is required for HAdV FK binding. The largest patch of interactions is situated at the AB loop of the FK, further smaller ones at the DE loop, the F strand, and the FG loop, whereas the latter is part of the opposite

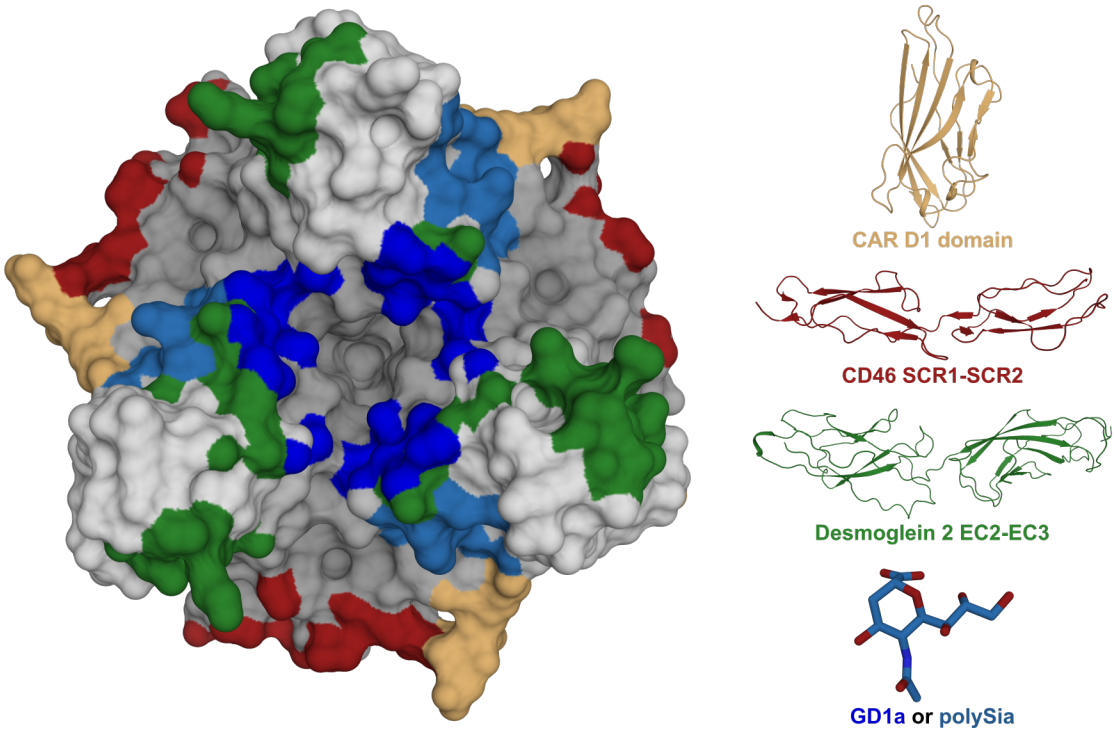

Figure 2) **Overview of HAdV FK receptor binding sites.** Three-fold symmetric binding sites of CAR (light orange), CD46 (red), DSG2 (green) and the sialic acid-based glycans GD1a (blue) or α-2,8-polysialic acid (light blue) projected on the HAdV37 FK surface viewed from the top.

monomer. Two cavities are formed by this interaction, which are accessible for solvent molecules.

CD46 is a human glycoprotein, which acts as complement response inhibitor by cofactor activity of C3b cleavage, which results in the C3bi fragment that is incapable of continuing complement activation. Furthermore, C4 is cleaved into C4c and C4d, the latter being again unable to continue the complement cascade [146, 147]. Additionally, CD46 is involved in adaptive immunity regulation and fertilization [141]. The protein interacts as a pathogen receptor for human herpesvirus 6 [148], measles virus [149] and most species B HAdVs [150, 151]. The extracellular domain consists of four short consensus repeat domains (SCR), out of which only SCR1 and SCR2 are involved in binding of HAdV11 [152] and HAdV21 [153]. The binding site is located on the side of the FK, in between two adjacent monomers (see Figure 2), but at a different site compared to CAR. The binding mode in both HAdV11 and HAdV21 is similar, and it involves the four loops HI, DG, IJ, and GH. While the HI and GH loops share a very similar conformation, there is a clear structural difference between the DG and IJ loops

of HAdV11 and HAdV21, and the DG loop of HAdV21 even changes its conformation upon CD46 binding [153]. The need for a structural rearrangement upon CD46 binding correlates well with a 20-fold lower affintiy of HAdV21 towards the SCR1-SCR2 fragment of CD46 (284 nM) compared to HAdV11 (13 nM).

Desmoglein-2 (DSG2) is a transmembrane protein localized at desmosomes, which are intracellular adhesive junctions that stabilize the vertebrate tissue [154]. The DSG2 ectodomain consists of four extracellular cadherin domains (EC1–EC4). Recently, DSG2 was found to be an attachment receptor for some species B HAdVs [155]. EC2 and EC3 are interacting with two monomers of the FK trimer simultaneously, however not from the side, but rather on top of the FK and closer to the three-fold axis (see Figure 2). EC2 is contacting the AB and CD loop of one monomer, while EC3 is interacting with the GH loop of the adjacent FK monomer [156]. Interestingly, cryoEM reconstructions of the HAdV3-DSG2 complex revealed an unusual binding ratio with either one or two DSG2 molecules per HAdV FK trimer [157].

Apart from the described protein receptors, sialic acid was shown to be a carbohydrate attachment receptor for the EKC-causing HAdV37, HAdV19, and HAdV8 [158, 159, 160]. Sialic acids in general are highly negatively charged α-keto acid sugars with a 9-carbon backbone and various substitution possibilities at the C4, C5, C7, C8, and C9 position. *N*-acetylneuraminic acid (Neu5Ac) is the most abundant form and commonly referred to as sialic acid [161, 162]. Recently, HAdV36 [Liaci et al., unpublished] and HAdV26 [163] were shown to bind sialic acid. They all share a very similar, three-fold symmetric binding site at the very top of the FK domain in close proximity to each other [164, 165]. A single sialic acid moiety is bound in a groove between two adjacent monomers (see Figure 2). Interestingly, HAdV52 recognizes sialic acid at a different binding site and it shows a preference for α-2,8-linked polysialic acid [166]. For HAdV37, the GD1a ganglioside was determined as the biological receptor that mediates infectivity [167]. GD1a has a branched hexasaccharide group with two terminal sialic acids, which is capable of occupying two of the three sialic acid binding sites of the HAdV37 FK simultaneously [167].

Since there is still no treatment against HAdV37-caused EKC available, a strategy was developed to block viral attachment by occupying multiple binding sites with a single molecule. Inspired by the pentavalent Shiga-like toxin inhibitor STARFISH [168], a trivalent HAdV37 inhibitor with a central tris(2-aminoethyl) amine group as *core*, a flexible *spacer*, and three terminal *sialic acid* moieties was designed, synthesized, and

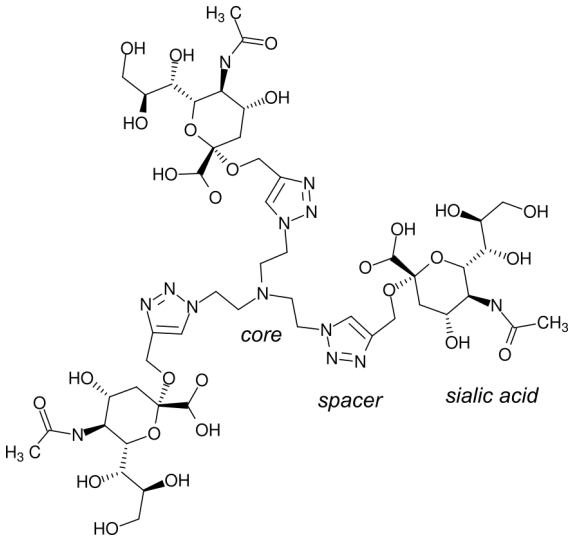

Figure 3) Structure of 2nd generation compound ME0462. The tertiary amine *core*, triazole-based *spacer* and terminal *sialic acid* moiety are labeled.

proven to bind all three sialic acid binding sites at the same time by X-ray crystallography [169]. Infection inhibition assays showed a four orders of magnitude increase in potency compared to monovalent sialic acid. However, probably due to high flexibility of the *spacer*, no electron density and no potential interactions were observed for linker parts of these compound structures. An adapted second generation of inhibitors uses a tertiary amine as *core* and triazole-based *spacers*, which allowed synthesis by simple click chemistry. This resulted in a further significant increase in potency for the compound ME0462 (see Figure 3) and a large part of the *spacer* and *core* structure could be visualized [170]. A similar strategy in inhibitor design was also applied for divalent polyomavirus inhibitors [171] and pentavalent sialic acid conjugates targeting Coxsackievirus A24 variant [172].

1.4.2 Attachment Factors of *Reoviridae*

Three different attachment receptors are currently known for ReoV: Junction Adhesion Molecule A (JAM-A), sialic acid, and the Nogo receptor 1 (NgR1).

JAM-A is a transmembrane protein with two extracellular, Ig-like domains [173] that is mainly expressed in human hematopoietic, endothelial, and epithelial cells [174, 175]. Upon homodimerization, JAM-A is thought to regulate tight junction permeability between adjacent cells. Furthermore, JAM-A forms heterophilic interactions with the

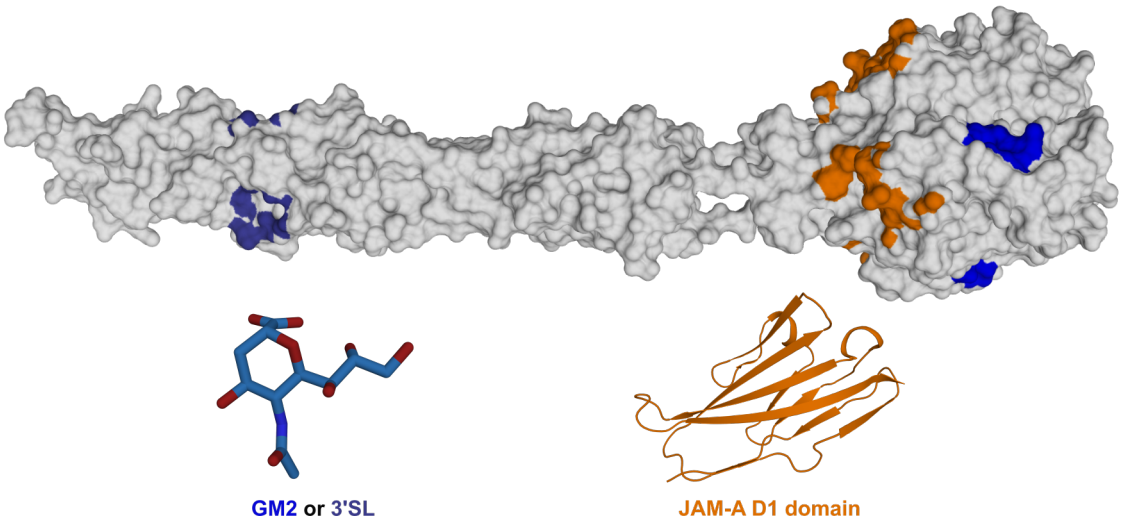

Figure 4) **Overview of ReoV receptor binding sites.** Three-fold symmetric binding sites of the JAM-A D1 domain (orange) and the sialic acid-based glycans GM1 at T1L (blue) or α-2,3-sialyllactose at T3D (dark blue) projected on the T1L σ1 body and head domain depicted as surface view.

αLβ2 integrin to regulate leukocyte interactions with endothelial cells and mediate leukocyte trafficking [174, 176, 177]. JAM-A was also determined to be a serotype-independent ReoV receptor, binding to the σ1 head domain [136, 178]. The binding site is, in both T1L and T3D, very similarly located at the lower end of the σ1 head involving numerous contacts with the 3_{10} helix of the DE loop (see Figure 4) [179, 180]. Interestingly, σ1 has a significantly higher affinity to JAM-A than JAM-A to itself, which might facilitate breaking the homodimer for subsequent ReoV attachment [179]. However, JAM-A is not required for replication in intestinal cells nor neural transmission, but it is necessary for hematogenous dissemination [181].

The second type of ReoV attachment receptor that is structurally characterized is sialic acid [182, 183]. It also binds to σ1, but has two distinct binding epitopes for serotypes 1 and 3. T3D binds various α-linked sialic acids, however not at the σ1 head domain, but near the N'-terminus of the body domain, which is approximately at the center of full-length σ1. Interestingly, additional residues were shown to be required for functional glycan recognition, although being slightly distant and thus not interacting with any of the sialic acids. The actual attachment receptor is probably a more complex, maybe branched sialylated glycan [184, 185]. In contrast, for T1L the GM2 ganglioside was identified as the biological attachment receptor, and this glycan binds at the σ1 head domain, close to the JAM-A binding site. The branched GM2 glycan has a terminal

Neu5Ac and a terminal *N*-acetylgalactosamine (GalNAc), which are both contacting the σ1 surface [186]. Nevertheless, binding of both JAM-A and GM2 should sterically be possible.

More recently, NgR1 was discovered as attachment factor for ReoV [187]. The single-pass transmembrane protein is expressed on the cell surface of neurons in a pattern that overlaps with T3D virus tropism in cortex, hippocampus, thalamus, and cerebellum [125, 181, 188]. NgR1 binds various ligands like Nogo-A or myelin-associated glycoprotein (MAG) [189], inhibits neuron outgrowth, and prevents axonal regeneration in the adult vertebrate CNS [190, 191]. The crystal structure of the extracellular domain of NgR1 reveals an overall banana-like shape including ten leucine-rich-repeat motifs (LRR) and two *N*-glycosylation sites at N82 and N179 (see Figure 5) [192, 193]. The known NgR1 ligands mostly bind at the concave NgR1 interface [194]. A striking difference to the previously characterized JAM-A and sialic acid is that NgR1 does not seem to follow the usual binding mechanism to σ1. While JAM-A binds to both virions and ISVPs, NgR1 is only capable of binding to virions, but not ISVPs [187]. Hence, NgR1 must either bind to σ3, which is removed during the transition of virions to ISVPs, or is incapable of binding to the altered σ1 conformation of ISVPs. However, the discrete interaction partner and mechanism is still unclear and will be targeted in this thesis.

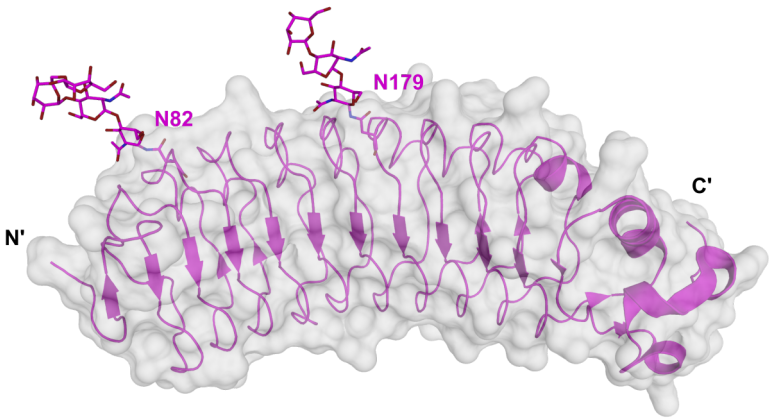

Figure 5) Crystal structure of NgR1. NgR1 has a banana-like shape and consists of ten LRR domains and two glycosylation sites at N82 and N179 (shown in stick representation). N'- and C'-termini are labeled in black.

1.5 Structural Biology Approaches

Structural biology is a powerful tool to visualize molecules at atomic resolution and to identify interaction mechanisms of binding partners, for example protein-protein-interactions or small molecule binding to proteins. Depending on the type of interaction, different methodologies are advantageous. Two of those techniques are X-ray crystallography and cryogenic electron microscopy (cryoEM), which will be described in the following chapters.

1.5.1 X-ray Crystallography

X-ray crystallography is based on the diffraction of X-rays at electrons of protein crystals. A crystal is a translationally periodic, finite assembly of unit cells, where each unit cell contains the same number of identically arranged molecules. Depending on the unit cell axes and corresponding angles, the crystal system can be triclinic, monoclinic, orthorhombic, tetragonal, rhombohedral, hexagonal or cubic. In combination with the centering of the next unit cell relative to the previous one, which can be either primitive (P), base-centered (C), face-centered (F), body-centered (I) or rhombohedral-centered (R), this results in the Bravais lattice of the crystal.

The molecules within a unit cell can be related by internal symmetry, either rotationally or translationally. Either two-, three-, four-, or six-fold rotational symmetry is possible within a unit cell. N-fold rotation with a subsequent translation along the respective axis is called a screw axis and is the second type of symmetry operation possible. Together, the Bravais lattice and symmetry operators define the space group of the crystal. The asymmetric unit is thereby the smallest subunit of a unit cell and contains all necessary information to describe the whole unit cell by applying symmetry operations. As there are no mirror planes allowed for protein crystals due to the chiral nature of amino acids, there are 65 possible space groups for proteins, from the low-symmetric triclinic P1 (where the asymmetric unit is equivalent to the unit cell) to the high-symmetric cubic F432 (where the unit cell comprises 96 copies of the asymmetric unit).

During a diffraction experiment, 99 % of all X-ray photons just pass through the crystal without scattering. However, a small number of photons is scattered by electrons within the crystal. Thereby a single photon induces oscillations at all electrons within the coherence length of the photon, which leads to virtual emanating waves. These waves

can interfere either constructively or destructively in reciprocal space, depending on their scattering angle. However, scattering of a single molecule is insufficient to be detected, which is why crystals are required to amplify the diffraction signal by constructive interference. The sum of all constructive scattering effects of multiple photons is called diffraction. This occurs only at crystal lattice planes (described by the Miller indices h, k, and l) with a certain distance d and scattering angle θ at the wavelength λ, so that Bragg's law (see Equation (1.1)) is fulfilled:

$$n\lambda = 2d\sin(\theta) \tag{1.1}$$

This results in a diffraction pattern in reciprocal space with discrete reflections, whose amplitudes can be measured with a detector and attributed to the crystal lattice planes by the Miller indices. However, at a single orientation of the crystal, only a small fraction of reflections fulfills the Laue condition (which can be visualized by the Ewald's sphere, see Figure 6). By rotating the crystal, which also rotates the reciprocal lattice, further reflections can be detected that now fulfill the Laue condition.

The diffraction pattern is centrosymmetric, i.e. each reflection [h, k, l] has a symmetry mate [-h, k, -l] in reciprocal space with the same intensity, both together called a Friedel pair. Furthermore, the crystal symmetry is displayed in the diffraction pattern. Hence, not a full 360° rotation is required to record a complete set of reflections, but only a fraction of it, depending on symmetry of the space group. After a complete set of reflection data has been recorded, the position of the scattering electrons within the crystal can be calculated.

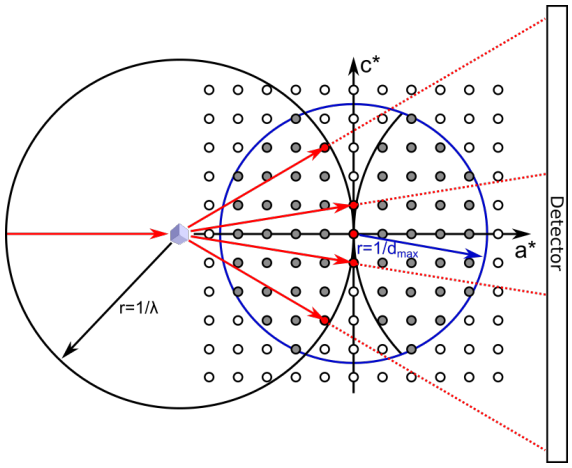

Figure 6) Ewald sphere. The reflection conditions for constructive interference are fulfilled for those reciprocal lattice points (red) that are within the diffraction limit d_{max} of the crystal (blue sphere) and intersect the Ewald sphere at wavelength λ (black sphere).

However, there is one major challenge in X-ray crystallography that must be overcome: the phase problem. While the detected reflections still contain the information about the scattered wave's amplitude, which correlates with the intensity of the reflection, the wave's phase information is lost during the transition from real to reciprocal space. There

are several techniques to solve this issue, for example using phases of a homologous protein structure, which allows for calculating an initial electron density map (Molecular replacement). Another option is to introduce anomalous scatterers into the protein crystal, e.g. compounds like uranyl acetate, potassium gold cyanide, mercury chloride, or selenium in form of selenomethionine, but also a regular bound zinc ion or sulfur from cysteines can be sufficient. Heavy atoms scatter anomalously, which means that the Friedel mates do not have the same intensity at a specific λ value. The anomalous part of the diffraction signal can be extracted from the reflection data and, as the number of anomalous scatterers is usually rather small, their location within the unit cell can be calculated using just the anomalous scattering data. This allows to generate initial phases and to calculate an initial electron density map using all scattering data.

Subsequently an atomic model is placed into the electron density map. The theoretical phase information of this model is then used to improve the calculated phase information of the experimental data. In iterative cycles of model fitting and map recalculation, the electron density map is further improved and allows for placing atomic coordinates that best describe the experimental electron density map.[2]

1.5.2 Cryogenic Electron Microscopy

Cryo-electron microscopy is a form of transmission electron microscopy (TEM), where particles are analyzed at cryogenic temperatures in a vitreous ice layer. In contrast to scanning electron microscopy (SEM), which analyzes the sample surface by reflected electrons, TEM detects transmitted electrons and allows for determining the inner structure of the sample. It has significantly improved over the past years, mainly due to advances in computational and instrumental technology. Structures at near-atomic resolution, which result in maps comparable to X-ray crystallography structures, can be obtained by single particle analysis (SPA), especially for large proteins or protein complexes above 100 kDa.

To prepare the sample for subsequent cryoEM analysis, the purified protein is applied to a metal grid with a holey carbon film, blotted with filter paper to remove excess protein solution and frozen in liquid ethane. This vitrification process aims for a thin layer of vitreous ice in the holes of the carbon film, which ideally contains a single layer of

[2] For a much more detailed explanation of X-ray crystallography see Bernhard Rupp's book *Biomolecular crystallography: principles, practice, and application to structural biology* [195]

particles with random orientations. Amorphous rather than crystalline ice is important to minimize background noise.

A high-resolution electron microscope collects images using a direct electron detector at a very low electron dose to minimize radiation damage, especially regarding high-resolution information. Cryocooling during data collection also helps to protect the protein from radiation damage. As low-dose imaging takes more time to achieve reasonable signal, each image suffers from slight particle movement during the data collection, induced by the electron beam. To counteract this, each image is collected as a large number of subframes, making a micromovie. The individual subframes are aligned to correct for the particle motion and subsequently summarized to a single micrograph. Nevertheless, the micrographs have a rather low signal-to-noise ratio. By averaging a large number of particle images of the same orientation, more contrast and thus details can be obtained.

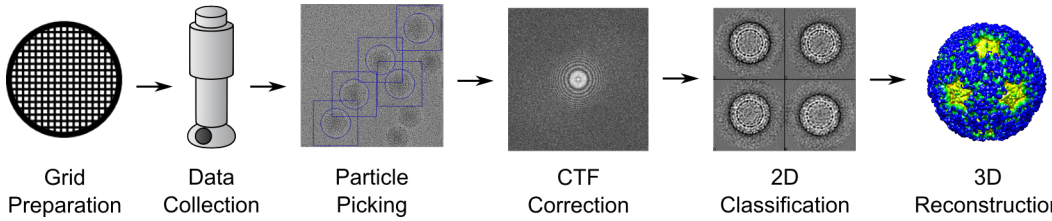

Figure 7) **CryoEM workflow.** The general cryoEM workflow consists of sample preparation by vitrification, data collection at an electron microscope and subsequent processing, particle picking from individual micrographs, CTF correction, 2D classification of the particles and finally a 3D reconstruction (inspired by [196]).

An important step is the selection of suitable particles from the micrographs. This can be performed either manually (feasible for large particles like viruses and a small number of micrographs) or computationally, for example by training a neural network for automated particle picking. The quality of the picked particles, i.e. the exclusion of icy, contaminated or otherwise unsuitable particles, is crucial for the final reconstruction quality.

Equally important to achieve high resolution reconstructions is the CTF correction. The electron wavefunction undergoes Fourier transformations while passing through the sample and the microscope's magnetic lens system for magnification. Hence, the final image is aberrated and has lost contrast, i.e. information, at certain spatial frequencies, i.e. resolution shells. This is known as contrast transfer function (CTF) and knowledge of the relevant spatial frequencies is necessary to extract the correct information from each micrograph. For this, the estimation and subsequent correction of the CTF is obligatory

to gain high-resolution reconstructions. To calculate the CTF for each micrograph, instrument parameters like acceleration voltage and spherical aberration along with the defocus, astigmatism, and amplitude contrast are required [197]. Defocus and astigmatism are becoming more accurate by fitting a calculated CTF, hence the CTF is also refined during SPA. To obtain information over a broad range of spatial frequencies, the defocus is slightly varied during data collection, which results in a shift of the CTF high-contrast peaks over different spatial frequencies.

The first step in obtaining a 3D particle model is the 2D classification of all particle images. An algorithm groups all particles into a certain number of 2D classes in a way that all particles within a class are similar to each other, while the class averages differ as much as possible [197]. By this, particles with the same orientation are grouped and averaging of all particles within a class results in a sharp, representative image of one particle orientation. This 2D class average image has a significantly improved signal-to-noise ratio and gives a first hint on the shape of the particle.

For the subsequent 3D reconstruction, a sufficient number of 2D classes with diverse particle orientations is required. The 2D class averages represent 2D projections of a single particle orientation. If there are enough projections of different particle orientations, these 2D projections allow the generation of a 3D particle model. Iterative refinement of the 2D classification and subsequently the 3D reconstruction results in a final map, into which atomic coordinates can be modeled.

To validate the quality and reliability of the 3D reconstruction, the entire dataset is split into two half sets at the beginning. The two resulting final maps are analyzed for their correlation per resolution shell in Fourier space (Fourier Shell Correlation = FSC) at a threshold level of 0.143. Further, the model-to-map FSC gives evidence about the fit of the atomic coordinates, describing the reconstruction, and thus also indirectly informing about the quality of the reconstruction .[3]

1.5.3 Advantages and Drawbacks of Each Approach

Both X-ray crystallography and cryoEM have quite different approaches to gather structural information, which come along with certain limitations. The biggest difference is the preparation of the proteins to be studied. One major bottleneck of X-ray crystallography

[3] A lot of information and knowledge from this brief summary is gathered from the online lecture *"Getting started in cryo-EM"* by Prof. Grant Jensen from the California Institute of Technology [198]

is the crystallization of the protein of interest. Usually, large amounts of protein, a long screening process, and time are required to optimize crystals, and in some cases crystals are never obtained. The protein also needs to be very pure and in a single conformation to grow a monocrystal, which is required for diffraction. SPA cryoEM analysis can distinguish among different conformational states or liganded and unliganded species at later stages of refinement, if sufficient data have been collected. However, this is still challenging and should be avoided if possible. Also the protein is still in solution prior to vitrification, which is closer to its physiologic state than the crystalline form. Additionally, smaller amounts of proteins are sufficient for cryoEM sample preparation.

However, currently only structures of species larger than 100 kDa can routinely be solved to reasonably high resolution ($\sim$ 3 Å), while it is much more difficult for smaller proteins. The currently smallest single specimen, whose structure was solved by cryo-EM, is the 40 kDa S-adenosylmethionine (SAM) riboswitch to a resolution of 3.7 Å. Streptavidin (52 kDa) is one of the smallest single proteins to be structurally characterized by cryoEM [199]. It is however possible to artificially enlarge the protein by using a scaffold of nanobodies [200] or DARPINs [201], which form a complex with the protein of interest and increase the size of the species to be structurally characterized. In contrast, X-ray crystallography is not only possible, but sometimes even easier for low molecular weight proteins. Usually, crystals do not need to grow as large for sufficient diffraction. Processing and refinement steps are less time consuming and also require less computational power.

The resolution of X-ray structures is better on average (the median resolution of PDB-deposited X-ray structures is between 2.0–2.5 Å [202]), although cryoEM is catching up fast (3.5–4.0 Å [203]). The high-resolution limit depends mostly on crystal quality, therefore developments in the experimental setup and software algorithms only facilitate solving difficult structures, but do not increase the achievable resolution much. The current high-resolution record is 0.48 Å for crambin [204]. The cryoEM resolution is mostly limited by mechanical or computational bottlenecks: the blotting quality, microscope magnification, detector resolution, and mostly by available software, although all of these limitations are steadily being improved. Currently, a reconstruction of apo-ferritin with a resolution of 1.22 Å is the highest resolution structure available [205]. However, one major limitation is the particle orientation on the grid, which can severely hamper data processing.

Depending on the aim of the project, the one or the other method can be advantageous.

For detailed structural information on smaller proteins or the interaction of low molecular weight compounds to target proteins, X-ray crystallography is favorable. Especially in cases of several very similar structures such as a set of mutants or drug compounds, data analysis is facilitated. For large proteins, protein complexes, or identifying the interface of protein-protein interactions, single particle cryoEM is the preferred method of choice.

1.6 Why Do We Need Structural Virology?

Even before the coronavirus pandemic drastically boosted the interest of non-virologists in the world of viruses, a major focus of scientific research was on shedding light on how viruses work. *Reoviruses* and *adenoviruses* are both widespread pathogens, either directly linked to severe diseases (EKC for HAdV37) or with a yet unknown causality (obesity for Ad36, celiac disease for ReoV). To understand the basic molecular mechanisms of viral infection, tropism, and propagation is essential to facilitate the development of effective treatments for disease prevention and cure. Structural biology approaches are a powerful tool to visualize important steps during a viral infection, e.g. docking of the virus to the host cell and subsequent interaction with the attachment receptor. This knowledge can be exploited to design drugs targeting the attachment mechanism, e.g. the trivalent sialic acid based inhibitors, which will be discussed later in this thesis.

Structural analysis can also provide valuable information on the evolution of viruses, which is generally determined by looking at amino acid conservation. In some cases however, the conservation of a certain motif is not clearly visible in the viral genome, but becomes obvious by looking at the three-dimensional protein structure. Hence, in this case only a structural comparison can reveal the ancestral relationship of two proteins and thus virus species.

Viruses are not only dangerous pathogens, but some of their features can also be used for medical applications, e.g. as vaccine vector. A replication-defective variant of HAdV26 is used for the SARS-CoV-2 vaccine from Johnson&Johnson, which has also flown through my veins [42]. Furthermore, distinct receptor specificities make some viruses suitable as oncolysins for targeting cancer cells. ReoV proliferates preferentially in Ras-activated tumor cells [206]. Reolysin is a replication-competent formulation of T3D ReoV that is currently in combinatorial clinical trials for treatment of various

cancers [207]. Also several clinical trials are ongoing for adenoviral oncolysins. Due to their great variance in genome, tissue distribution, and receptor specificity, they provide a large set of tools for engineering a suitable oncolysin, although liver toxicity is still a major downside of oncoviral treatment [208]. Structural biology can be a major contribution by identifying potential attachment sites and thus also potential targets for the viral vector. Structure-guided mutations can help to adapt the vector and improve its affinity for specific target cells, e.g. cancer cells.

Last but not least, structural virology is important simply for the scientific interest of understanding viruses. Why do viruses use a certain attachment factor? Why do different species share attachment factors, although they infect different tissues? Why are some receptor binding sites conserved, although they seem not necessary at all for successful cell entry as far as we know? And why are adenoviruses and reoviruses so similar in capsid organization, attachment strategies, and receptor usage, although being a completely different class of virus? To answer all these questions will take at least an incredible amount of experiments, scientists, and time, if it is ever possible at all. This work shall provide a small piece to support solving this puzzle in the future.

2. Objectives

The aim of this thesis is to shed more light on the attachment mechanisms of *adenoviruses* and *reoviruses*. Three topics will be covered in the following chapters.

Structural Analysis of HAdV56 FK Binding Sites for CD46 and Sialic Acid

HAdV56 has a low seroprevalence in humans and is a promising viral vector candidate. Preliminary experiments showed CD46 as potential attachment receptor and sequence analysis revealed a conserved sialic acid-binding motif. Therefore, one topic of this thesis is the crystallization and structural evaluation of the HAdV56 FK domain to shed light on the HAdV56 receptor engagement.

Adapting Trivalent Sialic Acid Inhibitors to HAdV37, HAdV36, and HAdV26

Viral attachment via a three-fold symmetric sialic acid binding site is well described for the EKC-causing HAdV37. Tailor-made inhibitors that prevent the virus from binding to host cells are a major step in containing this threat. Based on established trivalent sialic acid compounds, a new generation of inhibitors is analyzed by X-ray crystallography and adapted to other sialic acid binding serotypes HAdV36 and HAdV26 to lay the foundation for future inhibitor design strategies.

Structural Analysis of NgR1 Binding to the ReoV Capsid

NgR1 was determined as a novel attachment receptor for ReoV, however the distinct binding partner and mechanism are still unclear. Presumably, not the common attachment protein σ1, but the outer capsid protein σ3 is the interaction partner, which would indicate a second capsid protein to be involved in viral attachment, a novelty among known attachment mechanisms. Therefore, the σ3-containing heterohexameric capsomer $\mu 1_3 \sigma 3_3$ and NgR1 are purified and stable complex formation is evaluated. Subsequent structural analysis will provide a deeper understanding of ReoV attachment to the host cell.

3. Materials & Methods

3.1 Materials

3.1.1 Chemicals

All chemicals used in this work were of analytical grade and obtained from Merck (Darmstadt, Germany), Roth (Karlsruhe, Germany), Sigma-Aldrich (Taufkirchen, Germany), Thermo Fisher Scientific (Dreireich, Germany), Cytiva (Uppsala, Sweden), Molecular Dimensions (Sheffield, UK), New England Biolabs (Frankfurt, Germany) or Hampton Research (Aliso Viejo, USA). All buffers were prepared using Milli-Q water, sterile-filtered (0.22 µm), degased and stored at 4 °C. Reducing agents such as β-mercaptoethanol and DTT were added freshly prior to usage.

3.1.2 Bacterial Strains

The *Escherichia coli* (*E.coli*) cell strain DH5α (Thermo Fisher Scientific) was used for plasmid amplification, strain BL21(DE3) (Novagen, Darmstadt, Germany) for protein expression, and DH10Bac (Thermo Fisher Scientific) for bacmid generation.

MAX Efficiency™ DH5α	F– Φ80*lac*ZΔM15 Δ(*lac*ZYA–*arg*F) U169 *rec*A1 *end*A1 *hsd*R17 (rk^-, mk^+) *pho*A *sup*E44 λ^- *thi*$^-$1 *gyr*A96 *rel*A1
BL21(DE3)	F– *omp*T *hsdS*$_B$ (r_B- m_B-) *dcm gal* (DE3)
MAX Efficiency™ DH10Bac	F$^-$ *mcr*A Δ(*mrr*–hsdRMS–*mcr*BC) Φ80*lac*ZΔM15 Δ*lac*X74 *rec*A1 *ara*D139 Δ(*ara*, *leu*)7697 *gal*U *gal*K λ^- *rps*L *nup*G/pMON14272/pMON7124

3.1.3 Cell Lines

Sf9 insect cells (Thermo Fisher Scientific) were used for Baculovirus production, High Five™ insect cells and mammalian Freestyle 293-F cells (both Thermo Fisher Scientific)

for protein expression.

3.1.4 Plasmids

Table 3) List of plasmids.

Vector	Insert	Feature
pPROEX Htb	HAd37FK (residues 177–365)	N-terminal His6-tag, TEV cleavage site
pPROEX Htb	HAd36FK (residues 168–373)	N-terminal His6-tag, TEV cleavage site
pET15b	HAd26FK (residues 178–373)	N-terminal His6-tag, Thrombin cleavage site
pQE-30 XA	HAd56FK (residues 167–362)	N-terminal His6-tag
pcDNA3.1+	NgR1 (residues 1–310)	C-terminal His7-tag
pcDNA3.1+	NgR1 (residues 1–310)	C-terminal Fc-tag
pFastBac™ Dual	ReoV T1L μ1 & ReoV T1L σ3	simultaneous expression of both proteins

3.1.5 Buffers

HAdV37 IMAC Buffer A	30 mM Tris-HCl, pH 7.4 20 mM imidazole 150 mM NaCl
HAdV37 IMAC Buffer B	30 mM Tris-HCl, pH 7.4 500 mM imidazole 150 mM NaCl
HAdV37 Lysis Buffer	HAd37 IMAC Buffer A + 1 mM PMSF + 1 mM $MgCl_2$
HAdV36 IMAC Buffer A	30 mM Tris-HCl, pH 7.5 20 mM imidazole 150 mM NaCl
HAdV36 IMAC Buffer B	30 mM Tris-HCl, pH 7.5 500 mM imidazole 150 mM NaCl
HAdV36 Lysis Buffer	HAd36 IMAC Buffer A + 1 mM PMSF + 1 mM $MgCl_2$

HAdV26 IMAC Buffer A	25 mM Tris-HCl, pH 7.4 20 mM imidazole 150 mM NaCl
HAdV26 IMAC Buffer B	25 mM Tris-HCl, pH 7.4 500 mM imidazole 150 mM NaCl
HAdV26 Lysis Buffer	HAd26 IMAC Buffer A + 1 cOmplete™ EDTA-free protease inhibitor cocktail
HAdV26 SEC Buffer	25 mM Tris-HCl, pH 7.4 150 mM NaCl
HAdV56 IMAC Buffer A	30 mM Tris-HCl, pH 7.4 20 mM imidazole 150 mM NaCl
HAdV56 IMAC Buffer B	30 mM Tris-HCl, pH 7.4 500 mM imidazole 150 mM NaCl
HAdV56 Lysis Buffer	HAd56 IMAC Buffer A + 1 mM PMSF + 1 mM $MgCl_2$
HAdV56 SEC Buffer	30 mM Tris-HCl, pH 7.4 150 mM NaCl
NgR1 IMAC Buffer A	10 mM HEPES, pH 7.2 10 mM imidazole 150 mM NaCl
NgR1 IMAC Buffer B	10 mM HEPES, pH 7.2 500 mM imidazole 150 mM NaCl
NgR1 Fc Buffer A	100 mM glycine, pH 8.0 150 mM NaCl

NgR1 Fc Buffer B	100 mM glycine, pH 2.7 150 mM NaCl
NgR1 Fc Buffer C	1 M Tris-HCl, pH 8.8 150 mM NaCl
NgR1 SEC Buffer	10 mM HEPES, pH 7.4 150 mM NaCl
$\mu 1_3\sigma 3_3$ Buffer A	20 mM TRIS, pH 8.5 2 mM $MgCl_2$ 2 mM β-mercaptoethanol
$\mu 1_3\sigma 3_3$ IEX Buffer A	$\mu 1_3\sigma 3_3$ Buffer A + 100 mM NaCl
$\mu 1_3\sigma 3_3$ IEX Buffer B	$\mu 1_3\sigma 3_3$ Buffer A + 500 mM NaCl
$\mu 1_3\sigma 3_3$ HIC Buffer	$\mu 1_3\sigma 3_3$ Buffer A + 700 mM $(NH_4)_2SO_4$
$\mu 1_3\sigma 3_3$ SEC Buffer	20 mM BICINE, pH 9.0 2 mM $MgCl_2$ 150 mM NaCl 2 mM β-mercaptoethanol
SPR Running Buffer	10 mM HEPES, pH 7.4 at RT 150 mM NaCl 0.005 % TWEEN 20 50 µM EDTA
SPR Washing Buffer	10 mM HEPES, pH 7.4 at RT 150 mM NaCl 0.005 % TWEEN 20 3 mM EDTA

SPR Nickel Buffer	10 mM HEPES, pH 7.4 at RT 150 mM NaCl 0.005 % TWEEN 20 50 µM EDTA 500 µM $NiSO_4$
SPR His Regeneration Buffer	10 mM HEPES, pH 8.3 at RT 150 mM NaCl 0.005 % TWEEN 20 350 mM EDTA
SPR Fc Regeneration Buffer	10 mM glycine, pH 1.5 at RT
Crosslinking Buffer A	100 mM MES, pH 6.0 at RT 500 mM NaCl
Crosslinking Buffer B	100 mM Na_2HPO_3, pH 7.3 at RT 150 mM NaCl
Western Blot Transfer Buffer	3.025 g Tris-base 14.4 g glycine 0.2 L methanol 0.8 L H_2O

3.1.6 Commercial Crystallization Screens

Crystal Screen 1–2	Hampton Research
JBScreen Wizard 1–4	Jena Bioscience (Jena, Germany)
Morpheus®	Molecular Dimensions
PEG/Ion HT	Hampton Research
JCSG Plus	Molecular Dimensions

3.2 Methods

3.2.1 Molecular Biology

Transformation of chemically competent *E. coli* cells

Chemically competent DH5α cells were used for plasmid amplification and BL21(DE3) cells for protein expression and purification.

A 50 µL aliquot of frozen cells was thawed on ice, carefully mixed with 2 µL plasmid ($>$100 ng µL^{-1} plasmid concentration), and incubated on ice for 2 min. After a 42 °C heat shock for 90 s, the cells were cooled on ice and 900 µL antibiotic-free LB medium was added to the cells prior to incubation at 37 °C, 750 rpm for 60 min. For DH5α cells, the transformation mix was plated on LB agar containing 50 µg mL^{-1} ampicillin and incubated at 37 °C for 16 h, before a 20 mL pre-culture was inoculated containing 50 µg mL^{-1} ampicillin and incubated at 37 °C, 150 rpm for 16 h. For BL21(DE3) cells, the transformation mix was directly used to inoculate the pre-culture.

For bacmid recombination, 15 ng of pFastBac™ Dual plasmid was added to DH10Bac cells and the mixture was incubated on ice for 30 min. After a 90 s heat shock at 42 °C, the cells were incubated on ice for 2 min, 900 µL SOC medium was added, and the transformation mix was incubated at 37 °C, 750 rpm for 6 h. The mixture was centrifuged gently (500 g for 3 min), 800 µL supernatant was discarded, and the pellet was resuspended in approximately 200 µL. The sample was plated on LB Agar containing 50 µg mL^{-1} kanamycin, 7 µg mL^{-1} gentamycin, 10 µg mL^{-1} tetracycline, 20 µg mL^{-1} X-Gal, and 40 µg mL^{-1} IPTG and then incubated at 37 °C for 48 h. White colonies were restreaked on a fresh agar plate, incubated at 37 °C for 16 h and then a 20 mL pre-culture containing 50 µg mL^{-1} kanamycin, 7 µg mL^{-1} gentamycin, and 10 µg mL^{-1} tetracycline was inoculated and incubated for 16 h at 37 °C, 150 rpm.

Plasmid DNA Preparation

Plasmid DNA preparation was carried out using either the PureYield™ Plasmid Miniprep System (Promega, Walldorf, Germany), the GenElute™ Plasmid Miniprep-Kit (Sigma Aldrich), or the GenElute™ Plasmid Maxiprep-Kit (Sigma Aldrich) according to the manufacturer's instructions with the following modifications: A 20 mL *E. coli* overnight culture was used for the Miniprep Kits and a 500 mL culture for the Maxiprep Kit. DNA

was eluted from the column in two steps using Milli-Q H_2O with 1 min pre-incubation. The DNA concentration was determined by measuring the absorbance at a wavelength of 260 nm using a Nanodrop ND-1000 Spectrophotometer (Peqlab).

Protein Expression in *E. coli*

LB medium supplemented with 50 µg mL^{-1} ampicillin was inoculated using a BL21(DE3) pre-culture at a ratio of 1:150 and incubated at 37 °C, 130 rpm. At an OD_{600} of approximately 0.6 the expression was induced using 1 mM IPTG for HAdV37 and HAdV56, 0.5 mM IPTG for HAdV36, and 0.2 mM IPTG for HAdV26. The expression was either carried out for 5 h at 37 °C for HAdV56 and HAdV26, or for 16 h at 20 °C for HAdV37 and HAdV36. Cells were harvested using a Sorvall RC6 centrifuge and a Fiberlite™ F9-4 x 1000y rotor at 7,000 rpm for 15 min. The cell pellet was resuspended in the respective lysis buffer and lyzed on ice using a Branson Digital Sonifier 450 for two times 90 s at 40 % amplitude and an on/off pulse rate of 3 s/4 s for HAdV37, HAdV36, and HAdV56 or 1 s/1 s for HAdV26. The cell lysate was cleared by centrifugation using a SS-34 rotor at 17,000 rpm, 4 °C for 45 min and subsequently used for protein purification.

Bacmid DNA Preparation

Bacmid DNA preparation was carried out using the PureLink™ HiPure Plasmid Miniprep Kit (Invitrogen) according to the manufacturer's manual with the following modifications: A 20 mL overnight culture was used and after ethanol precipitation the DNA pellet was air-dried for 30 min.

Bacmid PCR analysis

To verify successful recombination of the bacmid DNA, PCR analysis was performed using the ExactRun High Fidelity proofreading DNA polymerase (Genaxxon) and standard pUC/M13 forward and reverse primers according to the reaction scheme in Table 4. The resulting DNA fragments were analyzed by agarose gel electrophoresis.

Agarose Gel Electrophoresis

For gel electrophoresis a 1 % agarose gel in TAE buffer supplemented with GelRed® (Genaxxon) was used. Samples were premixed with 6x Gel Loading Dye, purple (New

Table 4) Pipetting scheme and PCR program for bacmid PCR.

(a) **Pipetting scheme.**

Bacmid DNA (100 ng)	2 µL
pUC/M13 fwd (10 µM)	1 µL
pUC/M13 rev (10 µM)	1 µL
dNTPs (10 µM)	1 µL
5x ExactRun Reaction Buffer	10 µL
ExactRun Polymerase (0.5 U µL^{-1})	0.5 µL
H_2O	34.5 µL

(b) **PCR program.**

Step	Temperature	Time	Cycles
Initial Denaturation	94 °C	180 s	1x
Denaturation	94 °C	45 s	35x
Annealing	55 °C	45 s	
Elongation	72 °C	330 s	
Final Elongation	72 °C	420 s	1x
End	8 °C	∞	

England Biolabs) and the GeneRuler 1 kb Plus DNA Ladder (Thermo Fisher Scientific) was used as a reference. The gel electrophoresis was performed at 120 V for 45 min and subsequently the gel was analyzed using a UV transilluminator.

SDS-PAGE

SDS-PAGE analysis was used to investigate the purity of protein samples by separating individual protomers according to their molecular weight. A discontinuous 0.75 mm gel consisting of a 15 % resolving gel and a 4 % stacking gel was prepared as described in Table 5a. Protein samples were mixed in a 1:4 ratio with 4x Protein Sample Buffer (see Table 5b), boiled for 5 min at 95 °C and centrifuged for 2 min at 16,100 rpm. As a reference for regular SDS-PAGEs, the PageRuler™ Unstained Protein Ladder (Thermo Fisher Scientific) was used, in case of subsequent Western Blotting analysis the PageRuler™ Prestained Protein Ladder (Thermo Fisher Scientific) instead. For cross-linking assays, the Spectra™ Multicolor Broad Range Protein Ladder was used. SDS-PAGEs were performed at 250 V for 47 min and afterwards the gel was stained for at least 15 min in Instant*Blue*™ (Expedeon) and destained in Milli-Q H_2O overnight.

Table 5) Pipetting schemes for SDS-PAGE gels and 4x Protein Sample Buffer.

(a) **Pipetting scheme for 12x SDS-PAGE gels.**

	Resolving gel	Stacking gel
Acrylamide, 30 %	30.2 mL	3.9 mL
1.5 M Tris, pH 8.8	15.1 mL	-
1.5 M Tris, pH 6.8	-	7.3 mL
10 % SDS	603 µL	293 µL
10 % APS	603 µL	293 µL
TEMED	60.3 µL	29.3 µL
H_2O	13.8 mL	17.5 mL

(b) **4x Protein Sample Buffer.**

Glycerol	20 mL
1 M Tris, pH 6.8	20 mL
10 % SDS	10 mL
0.5 M EDTA, pH 8.0	1.63 mL
β-mercaptoethanol	4 mL
Bromphenol Blue	20 mg
H_2O	13 mL

Western Blotting

To verify the expression or purification of the correct protein, Western Blotting analysis was performed. First, a PVDF membrane was cut to the size of a SDS-PAGE resolving gel and equilibrated in methanol for 10 min, H_2O for 5 min, and Transfer Buffer for 10 min. The unstained SDS-PAGE gel was equilibrated for 15 min in Transfer Buffer and eight nitrocellulose filter papers at the size of the membrane were moistened with Transfer Buffer. The gel and the PVDF membrane were stacked in between four filter papers each and blotted at 20 V for 1 h. The PVDF membrane was blocked by incubation for 1 h at RT in TBS (20 mM Tris, pH 7.5, 150 mM NaCl) supplement with 5 % milk powder. The primary antibody (α-NgR1 goat mAB, AF1208, R&D Systems, Minneapolis, USA, or rabbit αT1L/T3D reovirus serum, Cocalico Biologicals, Pennsylvania, USA) was dissolved 1:2,000 or 1:10,000, respectively, in TBS supplemented with 5 % milk powder and the blotted membrane was incubated rotating at 4 °C overnight. Subsequently the membrane was washed with TBS-T (TBS supplemented with 0.5 % TWEEN-20) three times for 10 min, 15 min, and 10 min. Afterwards it was incubated for 1 h rotating at RT with the secondary antibody (rabbit α-goat IgG, H&L chain specific peroxidase conjugate, Calbiochem, or α-rabbit HRP conjugate, Jackson Immuno research) dissolved in TBS supplemented with 5 % milk powder at a ratio of 1:10,000 each. After four additional washing steps with TBS-T for 5 min, 10 min, 10 min, and 10 min, the Western Blot was evaluated using the Amersham ECL Plus Western Blotting Detection Kit (Cytiva) according to the manufacturer's instructions and a BioRad ChemiDoc™ MP Imager. For this, a colorimetric image to visualize the prestained protein ladder and a chemiluminescent image were acquired and subsequently merged for analysis.

3.2.2 Cell Culture

Transfection of Freestyle 293-F Cells

Freestyle™ 293-F cells were cultivated in suspension in Freestyle™ 293 Expression medium (Gibco™) at cell densities between 0.1×10^6 and 3×10^6 cells/mL on an orbital shaker in a humidified incubator at 37 °C, 150 rpm, and 8 % CO_2 atmosphere. One day prior to transfection, the cells were split to a cell density of 0.6×10^6 cells/mL and at the day of transfection they were diluted to a cell density of 1×10^6 cells/mL if necessary.

For transfecting 1 µg DNA per mL culture, the DNA was diluted in OptiPro™ SFM to a final concentration of 40 µg mL^{-1}, mixed with an equal volume of 120 µg mL^{-1} polyethylenimine (PEI 25K™, Polysciences), and incubated at 37 °C for 15 min. The transfection mix was added drop-wise to the cells and expression was carried out for 7 d. Afterwards, the supernatant was harvested using the Fiberlite™ F9-4 x 1000y rotor at 7,000 rpm for 15 min, supplemented with one tablet of cOmplete™ EDTA-free protease inhibitor cocktail (Roche) and immediately used for protein purification.

Transfection of Sf9 Cells

For transfection of Sf9 insect cells with bacmid DNA, the cells were cultivated adherently in SF900-II-SFM medium supplemented with 10 % FBS and 1 x P/S at 27 °C. Prior ro transfection, 8×10^5 cells were seeded in one well of a 6-well plate and allowed to attach for 15 min at RT. Afterwards, the medium was exchanged to 2.5 mL plating medium (SF900-II-SFM + 1.5 % FBS). 8 µL Cellfectin-I (expired for 10 years) were premixed with 100 µL plating medium, 1 µg bacmid DNA in 100 µL plating medium was added, and the transfection mix was incubated for 30 min at RT. Subsequently, the transfection mix was added drop-wise onto the cells and incubated for 4 h at 27 °C. Thereafter, the medium was exchanged to 2.5 mL SF900-II-SFM supplemented with 10 % FBS and 1 x P/S, and incubated for 72 h at 27 °C. Finally, the supernatant was harvested, centrifuged at 500 g for 5 min to remove any insect cells and the P1 baculovirus stock was stored at 4 °C in the dark.

Amplification of Baculovirus Stocks

For amplification of the baculovirus stock, Sf9 cells were cultivated in suspension in SF900-II-SFM with 1 x P/S. To generate a P2 viral stock, a 40 mL culture was inoculated with 1.2 mL P1 viral stock and incubated for 4 d at 27 °C. The supernatant was harvested, centrifuged for 5 min at 500 g to remove remaining insect cells, supplemented with 0.2 % FBS to prevent degradation by proteases, and stored at 4 °C in the dark. For amplification of the P2 viral stock to a P3 viral stock, a 500 mL culture was inoculated with 30 mL P2 viral stock and incubated for 5 d at 27 °C. The supernatant was harvested, centrifuged for 5 min at 1,500 g, supplemented with 0.2 % FBS and stored at 4 °C in the dark.

Infection of HighFive™ cells

For protein expression, HighFive™ insect cells were cultivated in suspension using Express Five® SFM medium in a shaking incubator at 27 °C and 130 rpm. At a cell density of 2×10^6 cells/mL, they were infected with P3 baculovirus stock according to Equation (3.1), targeting an MOI of 5 and assuming a viral titer of 1×10^8 pfu/ml.

$$\text{inoculation volume}[ml] = \frac{\text{number of total cells}}{\text{titer of viral stock}[\frac{pfu}{ml}]} \times \text{MOI}[pfu] \tag{3.1}$$

Infected cells were supplemented with 0.1 % FBS to prevent degradation by proteases and incubated for 96 h at 27 °C and 130 rpm. Afterwards, the supernatant was harvested by centrifugation at 3,500 g for 10 min and either stored at −20 °C or immediately used for protein purification.

3.2.3 Protein Biochemistry

Bioinformatics

Molecular weight, isoelectric point, and extinction coefficient predicitions were carried out using Expasy ProtParam [209]. Signal peptide and cleavage site prediction was carried out using the SignalP v. 5.0 server [210]. Multiple sequence alignments were performed with Clustal Omega [211, 212] and visualized with Jalview 2 [213].

Immobilized Metal Affinity Chromatograpy

For His-tagged proteins, immobilized metal affinity chromatography (IMAC) using pre-packed HisTrap FF crude 5 mL columns (Cytiva) was performed. The column was pre-equilibrated with 5 CV IMAC Buffer A by a peristaltic pump and the sample was loaded at a flow rate of 0.5–1 mL min^{-1}. Using an Äkta Prime system, the column was washed afterwards with 5 CV of 5–10 % IMAC buffer B and the protein was eluted either by step elution (20 %, 40 %, 60 %, and 100 % Buffer B) or 15 CV gradient elution up to 100 % IMAC buffer B. The UV absorption at 280 nm was observed, peak fractions were analyzed by SDS-PAGE, and fractions containing the recombinant protein were pooled.

Protein A Affinity Chromatography

Protein A affinity chromatography was applied for Fc-tagged NgR1 using a prepacked HiTrap Protein A HP 1 mL column (Cytiva). The column was pre-equilibrated with 5 CV NgR1 Fc Buffer A using a peristaltic pump, and the sample was loaded at a flow rate of 0.5–1 $mL\,min^{-1}$. Using an Äkta Prime system, the column was washed with 10 CV NgR1 Fc Buffer A, and the protein was eluted with 15 CV 100 % NgR1 Fc Buffer B. Fractions were immediately diluted 9:10 in pre-dispensed NgR1 Fc Buffer C to adjust the pH. The UV absorption was observed at 280 nm, peak fractions were analyzed by SDS-PAGE, and fractions containing the recombinant protein were pooled.

Ion Exchange Chromatography

As the recombinant $\mu1_3\sigma3_3$ heterohexamer does not have an affinity tag, an ion exchange chromatography (IEX) using a HiTrap Q FF 5 mL column (Cytiva) was performed as the first purification step. First, the column was pre-equilibrated with 5 CV $\mu1_3\sigma3_3$ IEX Buffer A and the HighFive™ insect cell supernatant was sterile filtered (0.2 µm) and loaded on the column at a flow rate of 0.3 $mL\,min^{-1}$ overnight. Using an Äkta Prime system, the column was washed with 150 mM NaCl in $\mu1_3\sigma3_3$ IEX Buffer and eluted with a 24 CV gradient from 100–550 mM NaCl. Protein-containing fractions were analyzed by SDS-PAGE and $\mu1_3\sigma3_3$-containing fractions were pooled and concentrated to a volume of 10 mL using an Amicon® Ultra-15 Centrifugal Filter Unit with a 100 kDa molecular weight cutoff (MWCO).

Hydrophobic Interaction Chromatography

For further purification of $\mu1_3\sigma3_3$, a hydrophobic interaction chromatography (HIC) using a HiTrap Phenyl HP 5 mL column (Cytiva) was performed. The concentrated protein sample was supplemented with $\mu1_3\sigma3_3$ Buffer A + 4 M $(NH_4)_2SO_4$ to a final concentration of 700 mM $(NH_4)_2SO_4$. The column was equilibrated with $\mu1_3\sigma3_3$ HIC Buffer and the sample was loaded at a flow rate of 0.5 $mL\,min^{-1}$. The column was washed with 4 CV of $\mu1_3\sigma3_3$ HIC Buffer and the protein was eluted with a 15 CV gradient from 700–0 mM $(NH_4)_2SO_4$. Peak fractions were analyzed by SDS-PAGE and fractions containing the recombinant protein were pooled.

Affinity Tag Cleavage

To remove cleavable His-tags from recombinant HAdV37 FK and HAdV36 FK, 1 mg TEV protease per 10 mg protein was added, supplemented with 1 mM DTT, and incubated at 4 °C overnight. The His-tag of the HAdV26 FK was removed by incubation with Trypsin in a 1:100 trypsin to protein ratio overnight at 4 °C, supplemented with 5 mM EDTA. Uncleaved protein and His-tagged TEV protease were removed by IMAC, where the flowthrough containing cleaved protein was collected and further purified.

Preparative Size Exclusion Chromatography

As final purification step for all proteins, a preparative size exclusion chromatography (SEC) was performed. The column was chosen according to the molecular weight of the protein and was equilibrated with 1 CV of the respective SEC buffer at a flow rate of 0.5 mL min^{-1} for the Superdex 75 Increase 10/300 GL column, 1 mL min^{-1} for HiLoad® 16/60 columns, and 3 mL min^{-1} for the HiLoad® 26/60 column (see Table 6). Protein was concentrated using Amicon® Ultra-15 Centrifugal Filter Units according to its molecular weight, sterile filtered, and SEC was performed at the respective flow rate. Peak fractions were analyzed by SDS-PAGE and subsequently pooled, concentrated to the desired concentration, aliquoted, flash-frozen in liquid nitrogen, and stored at −80 °C until further usage.

Table 6) Preparative size exclusion chromatography overview.

Protein	Buffer	Column
Ad37 FK	Ad37 SEC Buffer	HiLoad® 16/600 SD200 prep grade
Ad36 FK	Ad36 SEC Buffer	HiLoad® 16/600 SD200 prep grade
Ad26 FK	Ad26 SEC Buffer	HiLoad® 26/600 SD200 prep grade
Ad56 FK	Ad56 SEC Buffer	HiLoad® 16/600 SD200 prep grade
NgR1-His	NgR1 SEC Buffer	HiLoad® 16/600 SD75 prep grade
NgR1-fc	NgR1 SEC Buffer	Superdex® 75 Increase 10/300 GL
$\mu 1_3 \sigma 3_3$	$\mu 1_3 \sigma 3_3$ SEC Buffer	HiLoad® 16/600 SD200 prep grade

Analytical Size Exclusion Chromatography

To assess the purity of the proteins in more detail, analytical SEC was performed. The column was chosen according to the molecular weight of the protein or desired protein complex and was pre-equilibrated with 1 CV of the respective SEC buffer at a flow rate

of 0.055 mL min^{-1} (columns overview see Table 7). The proteins were sterile filtered and 35 µL sample were applied for analytical SEC. The absorption was recorded at wavelengths of 215 nm, 254 nm, and 280 nm.

Table 7) Analytical size exclusion chromatography overview.

Column	MW range [kDa]
Superdex® 75 Increase 3.2/300	3–70
Superdex® 200 Increase 3.2/300	10–600
Superose® 6 Increase 3.2/300	5–5,000

Complex Formation Assay

For complex formation trials of NgR1 and $\mu1_3\sigma3_3$, the proteins were dialyzed either in $\mu1_3\sigma3_3$ SEC buffer adapted to pH 7.4, or NgR1 SEC Buffer supplemented with 2 mM $MgCl_2$ and 2 mM β-mercaptoethanol using Slide-A-Lyzer™ MINI Dialysis Devices (Thermo Fisher Scientific) with a 10 kDa MWCO at 4 °C overnight. The proteins were mixed at different ratios of NgR1:$\mu1_3\sigma3_3$, incubated for various time ranges from 15 min to 16 h, at 4 °C, RT, or 37 °C and with or without the addition of 0.33 mM $CaCl_2$. Subsequently samples were analyzed by analytical SEC.

Surface Plasmon Resonance Spectroscopy

Surface plasmon resonance spectroscopy (SPR) was performed to analyze the interaction between NgR1 and $\mu1_3\sigma3_3$ using a Biacore X100 and a Sensor Chip NTA for immobilizing His-tagged NgR1, Sensor Chip Protein A for immobilizing Fc-tagged NgR1, and a Sensor Chip CM5 for amino coupling of $\mu1_3\sigma3_3$. Prior to SPR analysis, the proteins were dialyzed into SPR Running Buffer using Slide-A-Lyzer™ MINI Dialysis Devices with a 10 kDa MWCO at 4 °C overnight.

All experiments were performed according to the instructions of the Biacore software. In short, the Sensor Chip NTA was activated by SPR Nickel Buffer and various concentrations of ligand protein were applied to the active cell for 60 s or 180 s to identify a suitable concentration for ligand coupling. For binding experiments, the chip was activated with SPR Nickel buffer, ligand protein was injected to the active cell followed by a washing step using the SPR Washing Buffer. Various concentrations of the analyte protein were injected for 60 s for association, followed by 60 s dissociation time with SPR Running Buffer. Finally, the chip was regenerated using SPR His Regeneration

Buffer. As a negative control, cleaved HAdV37 FK or BSA were used. The signal of the reference cell was subtracted from the active cell to exclude unspecific binding effects. For better visualization, all samples were normalized against the baseline signal 10 s prior to sample injection.

The Sensor Chip Protein A was equilibrated with SPR Running Buffer and various concentrations of NgR1-Fc were applied to the active cell to determine a suitable concentration for ligand coupling. For subsequent binding experiments, 15 nM NgR1-Fc were immobilized to the chip surface and various concentrations of the analyte protein were injected for 60 s for association, followed by 60 s dissociation time with SPR Running Buffer. Finally, the chip was regenerated using SPR Fc Regeneration Buffer. For a negative control, cleaved HAdV36 FK was used. For analysis of the binding assay, the signal of the reference cell was subtracted from the active cell to exclude unspecific binding effects. For better visualization, all samples were normalized against the baseline signal 10 s prior sample injection.

For the Sensor Chip CM5 the Amine Coupling Kit (Cytiva) was used as described in the manual and as instructed by the Biacore software for coupling of $\mu 1_3\sigma 3_3$. A final concentration of 400 nM was immobilized on the CM5 chip surface and both His-tagged and Fc-tagged NgR1 were injected at a concentration range of 1.6–1,000 nM for 60 s, followed by 150 s dissociation time. For analysis of the binding assay, a buffer only run was subtracted from the sample run to exclude unspecific binding effects. For better visualization, all samples were normalized against the baseline signal 10 s prior to sample injection.

Pulldown Assay

The Pierce™ Protein A/G UltraLink™ Resin was used for a pulldown assay of Fc-tagged NgR1 and $\mu 1_3\sigma 3_3$. The proteins were mixed in a 1:1 ratio (w/w), diluted with 5x NgR1 SEC buffer in a 1:5 ratio of buffer to proteins to a total volume of 135 µL, and incubated at 4 °C overnight. Thereafter, 25 µL Protein A/G slurry was added and incubated for 2 h at RT. The sample was washed nine times by adding 200 µL NgR1 SEC Buffer, mixing, centrifuging for 2 min at 13,200 rpm, and removing the supernatant. For elution, 100 µL NgR1 Fc Buffer B was added, mixed, centrifuged for 2 min at 13,200 rpm, and the supernatant was collected. Finally, all washing steps as well as the final Protein A/G slurry were analyzed by SDS-PAGE.

For Pulldown Assays of His-tagged NgR1 and $\mu1_3\sigma3_3$, Ni-NTA Agarose (Qiagen) was used analogously with the following modifications: The proteins were mixed in a 5:2 ratio (w/w) with an excess of NgR1, the sample was washed six times after adding Ni-NTA Agarose, and the protein was subsequently eluted with NgR1 IMAC Buffer B.

Crosslinking Assay

Crosslinking assays were performed to analyze the possible formation of a complex of NgR1 and $\mu1_3\sigma3_3$. Dimethyl pimelimidate (DMP), dimethyl suberimidate (DMS), and glutaraldehyde were used for coupling of primary amines. For this, $\mu1_3\sigma3_3$ was mixed with His-tagged NgR1 (1:1 M/M) or Fc-tagged NgR1 (1:1.7 M/M) and incubated for 2 h at RT. The samples were diluted 1:10 and a 30-fold molar excess of either DMP or DMS (freshly dissolved in a 1:1 (v/v) mix of $\mu1_3\sigma3_3$ SEC Buffer and NgR1 SEC Buffer) was added and incubated for 1 h at RT. The reaction was quenched using 20 mM Tris-HCl and the samples were analyzed by SDS-PAGE.

Glutaraldehyde crosslinking was performed analogously with the following modifications: $\mu1_3\sigma3_3$ was mixed with His-tagged NgR1 in an 1:12 molar ratio and with Fc-tagged NgR1 in a 1:6 molar ratio and the samples were not diluted after initial incubation to increase the signal strength at SDS-PAGE analysis.

EDC and NHS were used to couple primary carboxyl groups of one protein to primary amines of the opposite protein. Fc-tagged and His-tagged NgR1 were dialyzed in Crosslinking Buffer A each and $\mu1_3\sigma3_3$ in Crosslinking Buffer B overnight at 4 °C. A 10-fold molar excess of EDC was added to the NgR1 samples and incubated for 15 min at RT. Subsequently, a 10-fold molar excess of NHS was added and incubated for another 15 min at RT. 20 mM β-mercaptoethanol was added to inactivate EDC and a sufficient amount Crosslinking Buffer B was added to adjust the pH. Finally, $\mu1_3\sigma3_3$ was added for crosslinking and incubated for 2 h at RT. The reaction was quenched by the addition of 33 mM Tris-HCl and the samples were analyzed by SDS-PAGE.

Deglycosylation Assay

For removal of *N*-linked glycans from NgR1 expressed in mammalian cell culture, a deglycosylation assay was performed. For this, 20 µg of protein was mixed with 2.5 µL of PNGase F (New England BioLabs) and 2 µL 10x Glycobuffer. The samples were incubated at 37 °C at 110 rpm overnight and subsequently analyzed by SDS-PAGE.

3.2.4 X-ray Crystallography

Crystallization of HAdV37 FK

The HAdV37 FK was crystallized as described previously [164]. Briefly, purified and sterile-filtered HAdV37 FK at a concentration of 12–13 $\mathrm{mg\,mL^{-1}}$ was crystallized at 20 °C using hanging drop vapour diffusion in a crystallization condition containing 26–29 % (w/v) polyethylene glycol 8,000, 50 mM zinc acetate, and 100 mM HEPES (pH 6.9–7.2). The inhibitor compounds ME1123, ME1145, and ME1146 were dissolved in the crystallization condition at a concentration of 20 mM, and crystals were soaked for 1.5–16 h and subsequently flash-frozen in liquid nitrogen without adding cryoprotectant.

Crystallization of HAdV36 FK

The HAdV36 FK was crystallized as described previously [214]. Briefly, purified and sterile-filtered HAdV36 FK at a concentration of 8 $\mathrm{mg\,mL^{-1}}$ was cocrystallized at 4 °C using hanging drop vapour diffusion in a crystallization condition containing 24–28 % (w/v) polyethylene glycol 3,350, 180–205 mM ammonium acetate, and 100 mM BIS-TRIS (pH 5.5), supplemented with 1–10 mM ME1123, ME1145, or ME1145, and 1:1,000 diluted seed stock from HAdV36 FK-4-*O*-Ac-3'SL cocrystals. Crystals were flash-frozen in liquid nitrogen using 20 % MPD as the cryoprotectant.

Crystallization of HAdV26 FK

The HAdV26 FK was crystallized according to an existing protocol [Karolina Cupelli, personal communication [215]]. Purified and sterile-filtered HAdV26 FK at a concentration of 1.3 $\mathrm{mg\,mL^{-1}}$ was crystallized at 20 °C using hanging drop vapour diffusion in a crystallization condition containing 3–6 % (w/v) polyethylene glycol 6,000 and 1.8–2.0 M NaCl. The inhibitor compounds ME0462, ME1015, ME1123, ME1145, and ME1146 were dissolved at a concentration of 20 mM in the crystallization condition and crystals were soaked for 1.5–4 h. Crystals were flash frozen in liquid nitrogen using 22.5 % (w/v) polyethylene glycol 8,000 as the cryoprotectant.

Crystallization of HAdV56 FK

For crystallization of the HAdV56 FK, various commercial crystallization screens were tested using the Crystal Gryphon LCP (Art Robbins Instruments) liquid handling robot

in a sitting drop vapor diffusion setup. Protein concentrations of 12, 14, and 21 mg mL^{-1} were screened at 4 °C and 20 °C. Best-diffracting crystals were obtained at 21 mg mL^{-1} and 4 °C in PEG/Ion HT condition 16, containing 200 mM magnesium nitrate hexahydrate and 20 % (w/v) polyethylene glycol 3,350 at pH 5.9 after 14 d. Crystals were either directly flash-frozen in liquid nitrogen using 20 % glycerol as cryoprotectant or soaked with 3'SL or 6'SL in reservoir solution for 4 h before freezing.

Data Processing, Refinement and Analysis

Diffraction data were collected at the Swiss Light Source (SLS), beamline X06DA (PXIII) at a wavelength of 1 Å using a Pilatus 2M detector. Indexing, integration, and scaling were carried out using XDS [216]. The phase problem was solved by molecular replacement using Phaser [217], implemented either in the CCP4 software suit [218] or in PHENIX [219]. Search models were derived using the published coordinates of HAdV37 FK (PDB ID: *1uxe*), HAdV26 FK (*6fjn*), the unpublished coordinates of HAdV36 FK [Manuel Liaci, personal communication], or, for HAdV56 FK, a CHAINSAW model of the HAdV37 FK [220]. Refinement was carried out in alternating rounds of manual model building in COOT [221] and restraint refinement using *phenix.refine* [222], including an initial simulated annealing refinement to remove model bias, three-fold NCS restraints (for HAdV37 FK, HAdV36 FK, and HAdV56 FK), and either TLS refinement or, for high resolution data, anisotropic B-factor refinement [223]. BKChem was used to compile a SMILES code for the inhibitor molecules and atomic coordinates and restraints were generated using *phenix.elbow* [224, 225]. For HAdV26 FK data, only one arm of the trivalent ligands was modeled, as the asymmetric unit only contains one monomer of the trivalent FK.

To calculate an anomalous double difference electron density map for confirming the presence of a zinc ion in the inhibitor binding site, two additional data sets at the high remote end of the zinc absorption edge (1.2821 Å) and at the low remote end (1.2848 Å) were collected of HAdV37 FK crystals soaked with ME1146 [226]. The data were processed using XDS with *FRIEDEL'S_LAW=TRUE* and the fully refined high resolution data set as reference data set. *Cad* from the CCP4 software suit was used to merge the anomalous intensity data from the high remote dataset and the low remote dataset as well as phase information from the high resolution dataset [227]. Subsequently *fft* [228] was used to calculate an anomalous double difference electron density map.

All figures were prepared using PyMol [229]. For surface charge analysis, the APBS Tool2.1 plugin for PyMol was used [230]. Refinement statistics and PDB accession codes are listed in Tables 8, S1, S2, and S3.

3.2.5 Cryogenic Electron Microscopy

Sample preparation and Vitrification

For preparing the sample for cryoEM analysis, purified T3D virions (prepared by Danica Sutherland, Department of Pediatrics, University of Pittsburgh School of Medicine, Pittsburgh, Pennsylvania, USA) were incubated with $8\,\mathrm{mg\,mL^{-1}}$ His-tagged NgR1 in a 1:4 (V/V) ratio or with PBS as unliganded control for 4 h at 4 °C. Quantifoil R3.5/1 copper grids were glow-discharged and 4 µL sample were applied, blotted for 3.5 s at 18 °C and 90 % humidity, and plunge-frozen in liquid ethane using a Vitrobot Mark IV (Thermo Fisher Scientific).

Data Collection and Processing

The specimens were imaged at 300 kV on a JOEL 3200 FSC cryo-electron microscope and a direct detector K2 summit camera (Gatan) in the NIH-funded National Center for Macromolecular Imaging at Baylor College of Medicine, Houston, Texas, USA. SerialEM was used to collect movie stacks at 20,000x magnification, corresponding to a pixel size of 1.71 Å [231]. Each movie stack was fractioned in 50 subframes with a total dose of 0.55 electrons/$\mathrm{Å}^2$. Image alignment and beam induced motion correction was carried out using the *alignframes* script from the IMOD software package [232]. For subsequent image processing and 3D-refinement, various algorithms from EMAN2.3 were used [233, 234]. To evaluate the micrograph quality based on their power spectra, *e2evalimage.py* was used and bad micrographs were sorted out manually. Initially, 7,182 ReoV-NgR1-complex particles and 11,046 unliganded ReoV particles were picked by a combination of the convolutional neural network particle picker and visual particle selection using *e2boxer.py* [235]. For CTF correction *e2ctf.py* was used, and reference-free two-dimensional (2D) class averages were calculated using *e2refine2d.py*. Good class averages, which were clearly representing a virus particle, were selected to generate an inital three-dimensional (3D) model using *e2initialmodel.py* with icosahedral symmetry restraints. The initial reconstruction was randomized to approximately 30 Å and used

as starting model for 3D refinement using *e2refine_easy.py*. *E2evalrefine.py* was used to sort out low-quality particles for further rounds of 3D refinement. Finally, 1,648 ReoV-NgR1-complex and 5,954 unliganded ReoV particles of high quality were selected and the 3D reconstructions were refined to final resolutions of 8.9 Å and 7.2 Å, respectively, according to the Gold Standard Resolution FSC plot of EMAN2.3 at a threshold of 0.143.

Structural Analysis

The 3D reconstructions were visualized using UCSF Chimera [236]. Atomic coordinates for NgR1 (PDB ID: *1ozn*) [193], σ2 (*1ej6*) [237], and the σ3 subunits of $\mu1_3\sigma3_3$ (*1jmu*) [72] from published crystal structures as well as for μ1 and λ2 (*7ell*), and λ1 (*7elh*) from a cryoEM reconstruction [76] were fitted into the asymmetric unit of the virus particle using the *Fit in Map* tool from Chimera. To improve the fit and reduce intermolecular clashes, a single real space refinement run using *phenix.real_space_refine* including simulated annealing was performed [238]. The ReoV map was subtracted from the ReoV-NgR1-complex map using the *vop* command in UCSF Chimera to calculate a difference density map. For calculating RMSDs, the *align* and *rms_cur* command in PyMol were used. All figures were prepared using either PyMol or UCSF Chimera.

4. Structural Analysis of HAdV56 FK Binding Sites for CD46 and Sialic Acid

Contribution of others

The expression plasmid was provided and SPR and infection inhibition assays were performed by Dr. David Persson, Lars Frängsmyr, and Prof. Dr. Niklas Arnberg, Department of Virology, Umeá University, Sweden. Katja Mindler assisted during her lab rotation project with protein purification, crystallization, and structure refinement under my supervision.

4.1 Results

Preliminary infection assays of the viral vector candidate HAdV56 have determined CD46 as attachment factor [Niklas Arnberg, personal communication]. However, the CD46 binding site on HAdV56 is unknown. Other HAdVs such as HAdV11 and HAdV21 bind CD46 via their fiber knob domain. Therefore, the aim of this project was to crystallize the HAdV56 FK, determine the atomic structure, and evaluate whether the CD46 binding site is conserved over the various serotypes of HAdVs.

4.1.1 Purification of HAdV56 Fiber Knob

The pQE-30 XA expression vector (provided by Dr. David Persson) encodes for amino acids 167–362 of the HAdV56 FK domain and an additional N'-terminal His6-tag for affinity chromatography. The protein was expressed in BL21(DE3) *E. coli* cells, which were subsequently lyzed by sonication. His-tagged HAdV56 FK was purified from the cleared supernatant via nickel affinity chromatography (see Figure 8) in order to remove most of the impurities. A final size exclusion chromatography was performed to remove soluble aggregate.

SDS-PAGE analysis of the SEC peak fraction revealed bands for the monomer at

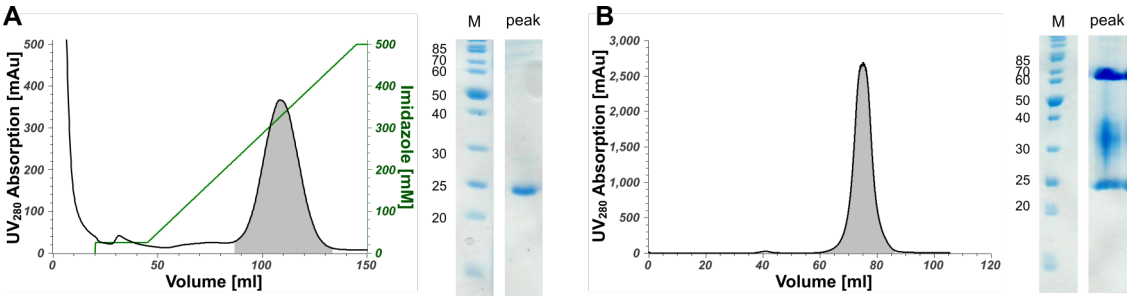

Figure 8) **Purification of HAdV56 FK. A:** IMAC chromatogram of HAdV56 FK purification showing a single peak during gradient elution and a single band at 24 kDa at SDS-PAGE analysis. **B:** The subsequent SEC chromatogram reveals a single peak, and SDS-PAGE analysis reveals bands at 24 kDa and 65 kDa corresponding to the HAdV56 FK monomer and trimer, respectively. Additionally, a smeary band between 30 kDa and 40 kDa is visible.

24 kDa, the trimer at approximately 65 kDa, and a smeary band between 30 kDa and 40 kDa, presumably displaying an artifact of sample preparation. Analytical size exclusion chromatography revealed a sharp, monomeric peak at an elution volume of 1.58 mL, which corresponds to a molecular weight of 47 kDa (see Figure 9 A).

4.1.2 Crystallization and Structure Determination

For crystallization of HAdV56 FK, various commercial crystallization kits were screened and resulted in crystals in PEG/Ion HT condition 16 containing 200 mM magnesium nitrate hexahydrate and 20 % (w/v) polyethylene glycol 3,350 at pH 5.9 at 21 mg mL^{-1} HAdV56 FK (see Figure 9 B).

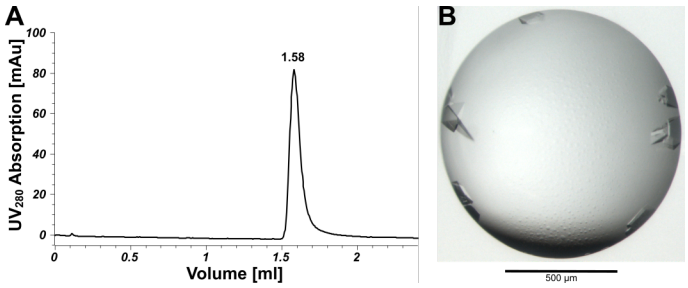

Figure 9) **Crystallization of HAdV56 FK. A:** Analytical SEC chromatogram of HAdV56 FK showing a single peak at an elution volume of 1.58 ml corresponding to a molecular weight of 47 kDa. **B:** Crystals at 21 mg mL^{-1} HAdV56 FK in PEG/Ion Ht condition 16.

Data were collected to a high resolution limit of 1.38 Å at the SLS beamline X06DA (PXIII) and processed using XDS. Crystals grew in space group C 1 2 1 comprising four HAdV56 FK trimers per asymmetric unit at a solvent content of 49.0 %. The

phase problem was solved by molecular replacement using a HAdV37 FK model (76 % sequence identity), which was truncated to contain only atoms that are identical for HAdV37 and HAdV56. Subsequently, the structure was refined using COOT and *phenix.refine* (data processing and refinement statistics see Table 8).

Table 8) Data processing and refinement statistics of HAdV56 FK structures.

	HAdV56 FK	HAdV56 FK + 3'SL
Data processing		
Space group	C 1 2 1	C 1 2 1
Cell dimensions		
a, b, c [Å]	132.2, 182.1, 116.8	132.4, 181.9, 117.1
α, β, γ [°]	90.0, 118.6, 90.0	90.0, 118.5, 90.0
Resolution (high resolution bin) [Å]	49.1–1.38 (1.46–1.38)	44.9–1.75 (1.85–1.75)
Reflections overall	3,352,647 (507,196)	1,684,422 (259,199)
Reflections unique	491,039 (77,802)	244,391 (39,186)
Redundancy	6.8 (6.5)	6.9 (6.6)
Completeness [%]	98.9 (97.0)	99.7 (99.1)
I/σ (I)	12.41 (1.15)	11.35 (1.29)
R_{meas}	8.6 (146.1)	14.9 (148.0)
$CC_{1/2}$	99.9 (47.9)	99.8 (51.4)
Wilson B [$Å^2$]	23.7	30.4
Refinement		
No. of atoms total	20,234	19,556
protein	18,081	17,301
ligand	-	148
solvent	2,153	2,107
R_{work} / R_{free} [%]	13.4 / 16.7	17.3 / 20.9
R.m.s.d bonds [Å]	0.010	0.011
R.m.s.d angles [°]	1.09	1.11
B factor overall [$Å^2$]	27.6	32.7
protein	25.7	31.5
ligand	-	45.4
solvent	41.6	41.0
Ramachandran [%]		
favored	96.21	95.38
allowed	3.79	4.33
outlier	0	0.09

4.1.3 Structural Analysis of the Putative CD46 Binding Site

The HAdV56 FK adopts a fold that is very similar to existing FKs, with a central β-sandwich at each protomer and various surface loops that define the receptor interactions (see subsection 1.4.1). Existing crystal structures of CD46 in complex with HAdV11

[152] or HAdV21 [153] show a noticeably conserved binding motif at the side of the knob domain involving the HI, DG, GH, and IJ loops. To compare the sequence conservation of crucial residues, a sequence alignment of HAdV56, the high-affinity CD46-binders HAdV35, HAdV21, HAdV11, and the low-affinity CD46-binder HAdV7 was performed (Figure 10 A). Interestingly, critical residues at HAdV11 (N247, R280, N283, D284, Q305) and HAdV21 (R247, Y263, T280, N304) are also partly conserved for HAdV35 and HAdV7, but completely missing at HAdV56. Furthermore, there are gaps of 3–6 residues in the GH, DI, and IJ loops, while the DG loop is elongated by two additional amino acids. In summary, the sequence alignment reveals significant differences at the crucial loop sections.

Superposition of the HAdV56 crystal structure with species B liganded HAdV11, unliganded HAdV11, and HAdV7 FKs depicts significant structural differences (Figure 10

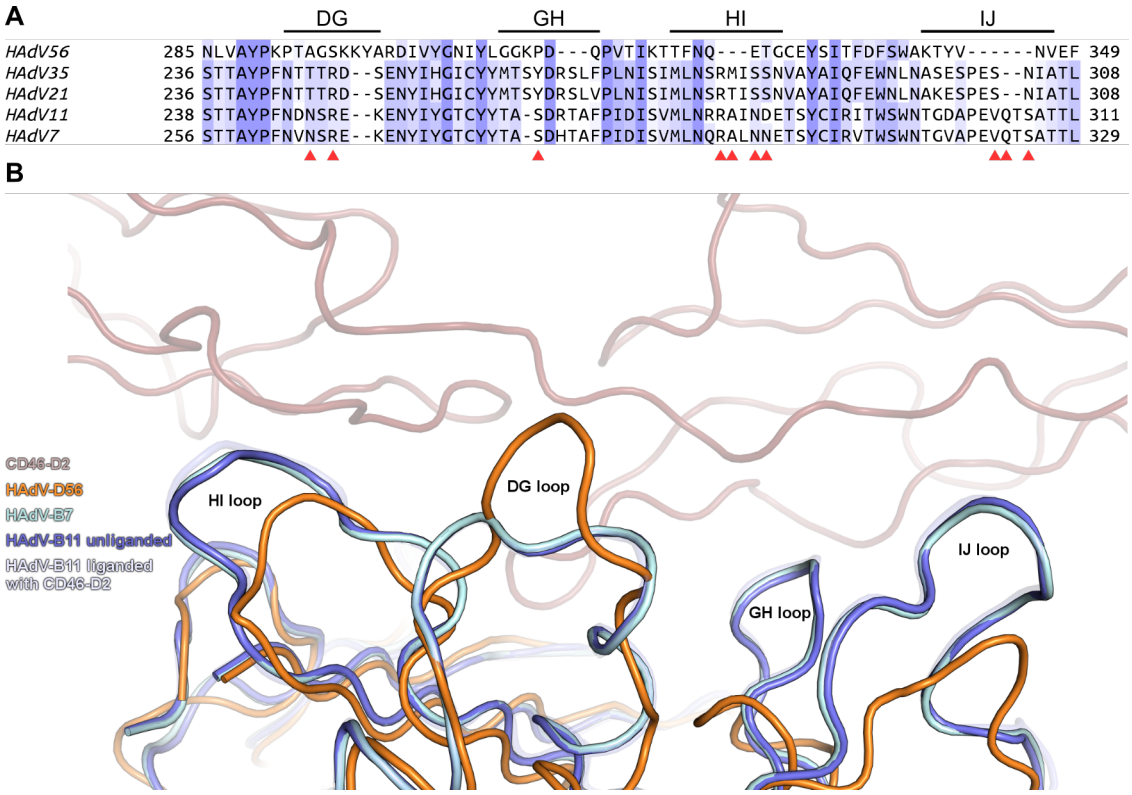

Figure 10) **Sequence alignment and structural superposition of the loops involved in CD46 binding at HAdV11, HAdV7 and HAdV56. A:** Sequence alignment of HAdV56, HAdV35, HAdV21, HAdV11, and HAdV7 performed with Clustal Omega [211] and visualized using JalView [213]. Amino acid conservation is colored in blue according to the BLOSUM62 matrix, critical residues for CD46 interaction are marked by red arrowheads. **B:** Superposition of the main interacting HI, DG, GH, and IJ loops of HAdV11 (blue) in complex with CD46-D2 (red), unliganded HAdV11 (faint blue), HAdV7 (cyan) and HAdV56 (orange). Modified from "*Human species D adenovirus hexon capsid protein mediates cell entry through a direct interaction with CD46*", Persson et al., Proceedings of the National Academy of Sciences, 118(3):e2020732118 [239].

B). The DG loop conformation of CD46-binding FKs was observed as either retracting, resulting in a more stable conformation (HAdV11), or protruding, which provides slightly more flexibility (HAdV21). However, the HAdV56 DG loop is elongated by two amino acids and as a consequence turned upwards in a way that the corresponding amino acids are out of reach for CD46. In contrast, the remaining loops HI, GH, and IJ are significantly shorter compared to HAdV11 and HAdV7, and are likewise not accessible for CD46 interaction. The overall structural conformation of the relevant HAdV56 FK loops in combination with the sequence difference of key residues makes CD46 binding at the known binding site unlikely.

4.1.4 Structural Analysis of the Sialic Acid Binding Site

Another common attachment receptor of species D HAdVs is sialic acid. Sequence alignment of the HAdV56 FK with known sialic acid binding HAdV serotypes 37, 36, and 26 shows a strong conservation of distinct residues involved in binding, namely N307, Y309, and K342 (see Figure 11 A). The electrostatic surface potential at the top of the HAdV56 FK is significantly positive, similar to HAdV37, and especially the grooves between single protomers, where sialic acid binds, are highly positively charged. In contrast, non-sialic acid binding HAdV19 and HAdV3 FKs have a clearly negative electrostatic surface potential at the top of the fiber knob, which prevents binding of the alike negatively charged sialic acid.

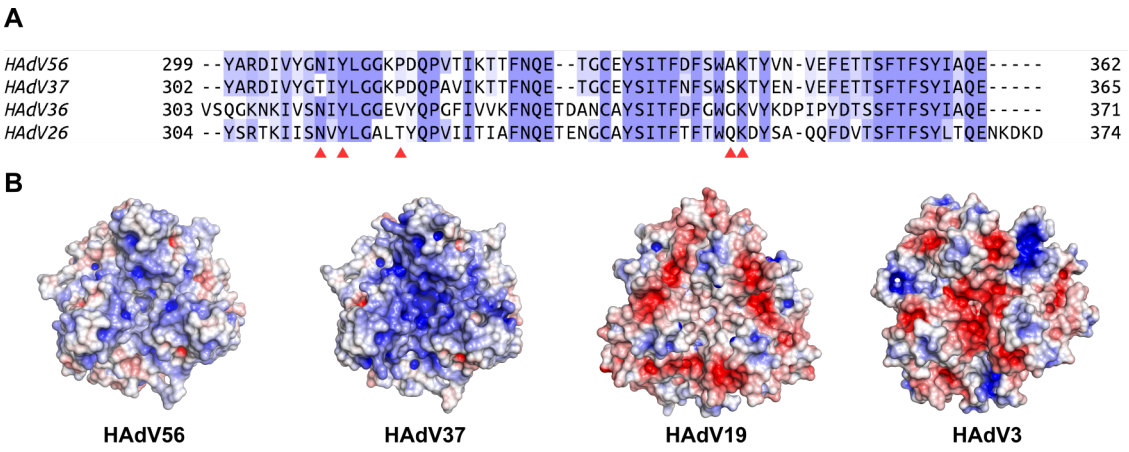

Figure 11) **Sequence alignment and surface charge analysis. A:** Sequence alignment of HAdV56 FK with the FKs of sialic acid-binding HAdV37, HAdV36, and HAdV26. Amino acid conservation is colored in blue according to the BLOSUM62 matrix, critical residues for sialic acid binding of HAdV37 are marked by red arrowheads. **B:** The surface charge of HAdV56 FK, HAdV37 FK, HAdV19 FK, and HAdV3 FK is displayed in a color gradient from −5 kT (red) to 5 kT (blue).

To validate the sialic acid binding, HAdV56 FK crystals were soaked with 3'SL and subsequently the structure was determined. Unambiguous electron density was observed for the sialic acid moieties in two of the four fiber knob trimers within the asymmetric unit. Some additional electron density for the neighboring galactose moieties is visible, however modeling was only possible in two cases. The remaining two trimers in the asymmetric unit are arranged head-to-head, and thus the binding site is not accessible for soaking.

The binding mode of sialic acid is the same as observed for HAdV37. Three direct polar contacts are formed by one protomer via Y309, P314, and K342 to the C3-hydroxyl group, the N-acetyl group, and the C2-carboxyl group, respectively, and they are essentially the same as for HAdV37 (see Figure 12). On the opposite side of the sugar, N307 also forms a direct polar contact to the hydroxyl group of the N-acetyl moiety, while T310 in HAdV37 interacts via a water molecule. The water-mediated interaction of S344 from the HAdV37 I β-strand to the C7-hydroxyl is replaced by T319 from the HAdV56 H β-strand. There are no differing contacts observed and RMSD calculation revealed an average atomic displacement of 0.38 Å of the sialic acid moiety, hence no shift in the binding pocket.

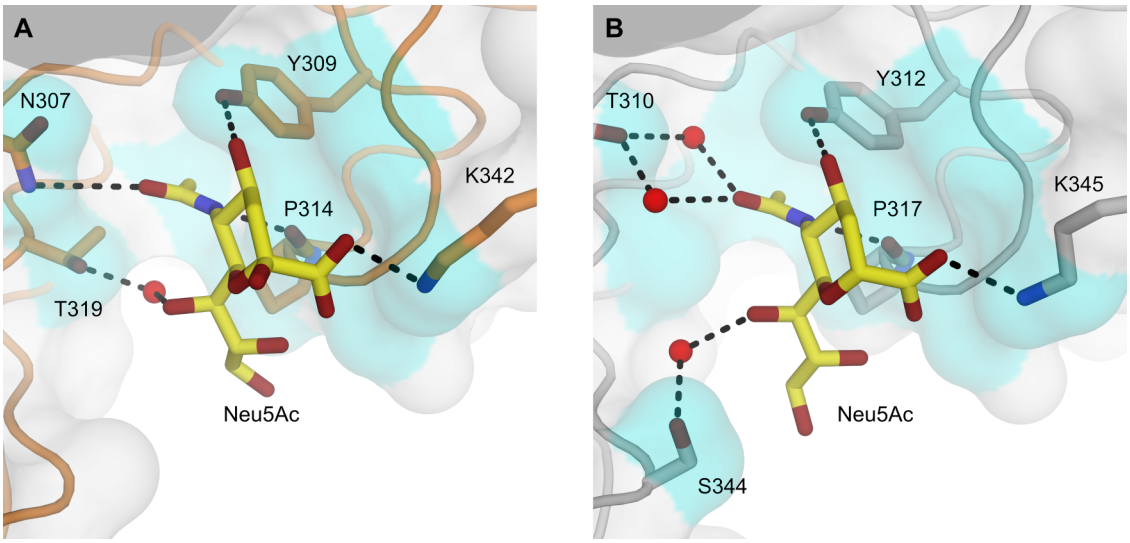

Figure 12) **Structural superposition of sialic acid binding sites of HAdV56 and HAdV37. A+B:** Amino acids of HAdV56 (A) and HAdV37 (B) involved in binding of sialic acid (yellow) are displayed as sticks in orange and gray, respectively, water molecules as spheres (red), and polar interactions as dashed lines (black).

4.2 Discussion

4.2.1 HAdV56 FK Does Not Bind CD46

The expression and purification of the HAdV56 FK domain yielded highly pure protein, as confirmed by analytical SEC, in sufficient quantity for a large-scale crystallization screening. The obtained crystals comprised four trimeric knob domains per asymmetric unit. Although two of the trimers are arranged in a way that blocks the sialic acid binding site, the overall loop geometry is not affected by crystals contacts and thus comparable in all four knobs.

In the published complex structures, the interaction surfaces of CD46 and the respective knob domains complement each other very well, and subtle changes drastically affect the binding affinity. HAdV11 has a K_D of 11 nM for binding CD46-D2 [153]. At this interaction, R280 forms an important salt bridge by changing its orientation from the unliganded state upon CD46-binding [152]. R279 is important for stacking against R280 to stabilize this interaction. In both HAdV7 and HAdV14, R279 is mutated to Q279 and the K_D values drop to 35 µM and 27 µM, respectively, for CD46-D2 [240]. While the overall loop conformation is almost identical, this single amino acid mutation leads to a 1000-fold loss of affinity. As the loop conformation of HAdV56 is clearly altered compared to the CD46-binding HAdV7 and HAdV11, an interaction at this site is unlikely.

To check whether the HAdV56 FK is actually involved in cell attachment, infection assays using soluble protein for competition were performed (by Dr. David Persson) [239]. Preincubation of CHO-CD46 cells with soluble HAdV35 FK inhibits infection, thus the FK competes with HAdV56 virus for the CD46 binding site. In contrast, soluble HAdV56 FK does not block the infection of CHO-CD46 cells. Also SPR experiments confirmed, that soluble HAdV35 FK interacts with CD46, while HAdV56 FK does not (see Figure 13 A) [239]. In summary, the structural and biological data suggest that the HAdV56 FK is not the interaction partner for CD46-mediated attachment.

4.2.2 CD46 Interaction is Mediated by the HAdV56 Hexon

It follows that there must be another HAdV56 capsid protein that interacts with CD46 for cell attachment. Further SPR studies could identify the HAdV56 hexon to interact with CD46 (see Figure 13 B) [239]. The biological relevance of the HAdV56 hexon as attachment receptor was additionally verified by cell-based transduction assays. Preincu-

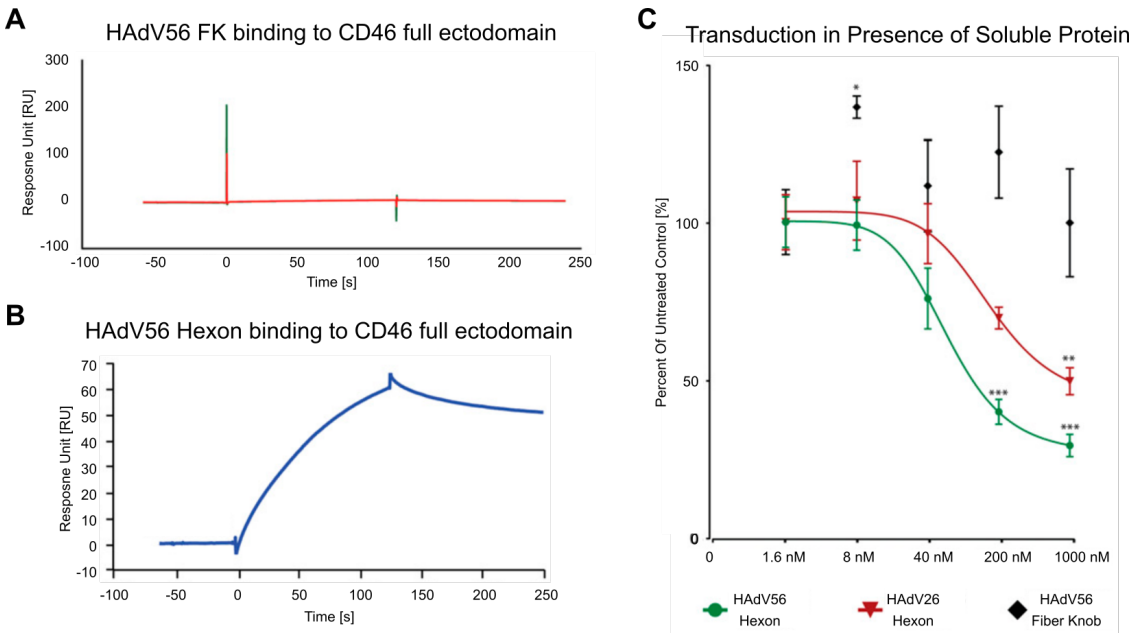

Figure 13) **SPR Analysis and Transduction Assays Confirming CD46 Interaction With HAdV56 Hexon. A–B:** SPR analysis of the HAdV56 FK (A) and the HAdV56 hexon (B) on the immobilized CD46 ectodomain. **C:** HAdV56 transduction assays of A549 cells in the presence of soluble HAdV56 hexon (green), HAdV26 hexon (red), and HAdV56 FK (black) . Modified from "*Human species D adenovirus hexon capsid protein mediates cell entry through a direct interaction with CD46*", Persson et al., Proceedings of the National Academy of Sciences, 118(3):e2020732118 [239].

bation with soluble HAdV56 hexon as well as with HAdV26 hexon inhibits infection of A549 cells, while HAdV56 FK does not (see Figure 13 C). CryoEM analysis of the HAdV56 virion in complex with CD46 revealed a potential CD46 binding site at the center of the hexon. However, the moderate resolution did not allow to propose a detailed interaction mechanism.

Interestingly, soluble CD46 was able to inhibit infection for a large number of species D HAdVs, but never completely. Therefore, either the binding affinity or concentration of soluble CD46 was insufficient. Alternatively, it is possible that the viruses are not depending on a single receptor, but are capable of an alternative attachment pathway, which is independent of CD46. The conserved sialic acid binding site at the FK domain could be involved in this second pathway. New HAdV serotypes are usually emerging by recombination of the three main structural protein encoding genomes - penton, hexon, and fiber. In case of HAdV56 for example, this type has the the almost identical (99%) fiber of HAdV9 [52, 241, 242]. Possibly, the ability to bind sialic acid is rather a recombination artifact and not obligate for infection, but can still be recovered as backup in case CD46-mediated attachment is blocked.

4.2.3 Novelty of a Second Attachment Receptor Binding Site

While it is not uncommon for a virus to utilize different host receptors for cell attachment, this is the first time that the HAdV hexon has been involved in this interaction, and it is also undescribed so far among viruses that two different capsid proteins are capable of viral attachment. Although the penton base is known to bind integrin, similar to the ReoV λ2 capsid protein, this occurs at a later stage of viral uptake and is not required for initial attachment to the host cell.

For most other viruses, so far only a single viral protein is described for being responsible for host cell attachment. SARS-CoV1 and SARS-CoV2 bind the Angiotensin-converting enzyme 2 (ACE2) via the surface spike protein [243]. Polyomaviruses bind to oligosaccharides featuring a terminal sialic acid, either in form of gangliosides or glycoproteins, using the major capsid protein VP1 [244]. Similarly, human influenza viruses only use hemagglutinin to bind α2,3-linked sialic acid [245]. Rotaviruses, which belong to the *reovirus* family, utilize several receptors depending on the serotype, including sialic acid, the heat shock cognate protein hsc70 [246], and HBGAs, which are all recognized by trypsin-cleaved subdomains of the VP4 spike protein [247, 248, 249, 250].

However, within a virus family, the capsid protein can adapt in a species-dependent manner to bind the preferred receptor molecule of the respective target host cell. As described in subsection 1.4.1, the HAdV FK binds to various host receptors depending on the type, and there are even different binding sites for sialic acid in case of HAdV52 and the species D HAdVs. For some viruses, especially smaller ones like polyomaviruses, there is only a single outer capsid protein present for binding an attachment receptor. In other cases, the protruding spike proteins of coronaviruses and reoviruses or the hemagglutinin of influenza viruses are more accessible compared to other capsid proteins. Although binding a receptor does not necessarily require much space or interaction area, the probability of adapting to a new receptor is higher for exposed capsid proteins due to a more frequent contact with the cell surface. In this respect, the discovery of a second capsid protein, which is not protruding as prominent from the virus surface, but still involved in viral attachment, is even more remarkably. The fact that in case of CD46, one receptor is recognized by two different viral proteins within a highly similar group of viruses, highlights the complexity and the need for further research on viral propagation within humans to prepare for upcoming virus pandemics.

5. Adapting Trivalent Sialic Acid Inhibitors to HAdV37, HAdV36, and HAdV26

Contribution of others

The inhibitor compounds were designed by Dr. Manuel Liaci (University of Tuebingen) and designed and synthesized by Dr. Emil Johannson, Dr. Rémi Caraballo and Prof. Mikael Elofsson (Department of Chemistry, Umeá University, Sweden). Affinity and infection assays were performed by Dr. David Persson, Katarina Danskog, and Prof. Niklas Arnberg (Department of Clinical Microbiology, Umeá University, Sweden). Crystallization, data collection, and data processing of HAdV36 in complex with ME0462 was performed by Gregor Wiese and Dr. Manuel Liaci, and of HAdV37 and HAdV36 in complex with ME1015 by Paul Bachmann. Patrick Wörz assisted with the purification of HAdV36 FK protein and refinement of the HAdV37-ME1123 complex structure during his lab rotation.

5.1 Results

The first part of this project aims to further improve the established trivalent inhibitors for HAdV37 [170]. Based on existing structural data, a new generation of molecules was designed and synthesized. In contrast to the 2nd generation inhibitor ME0462, the *spacers's* triazole ring of the novel compounds ME1123 and ME1146 is flipped (see Figure 14 A and B) and directly coupled to the anomeric C2 carbon of the sialic acid group, without intermediate oxygen atom. This results in a shorter linker between *core* and *sialic acid* and an overall more compact structure of the compounds. The linkage via either one or two carbons to the *core* amine (ME1123 and ME1146, respectively) allows for determining the ideal distance of the sialic acid moieties from each other.

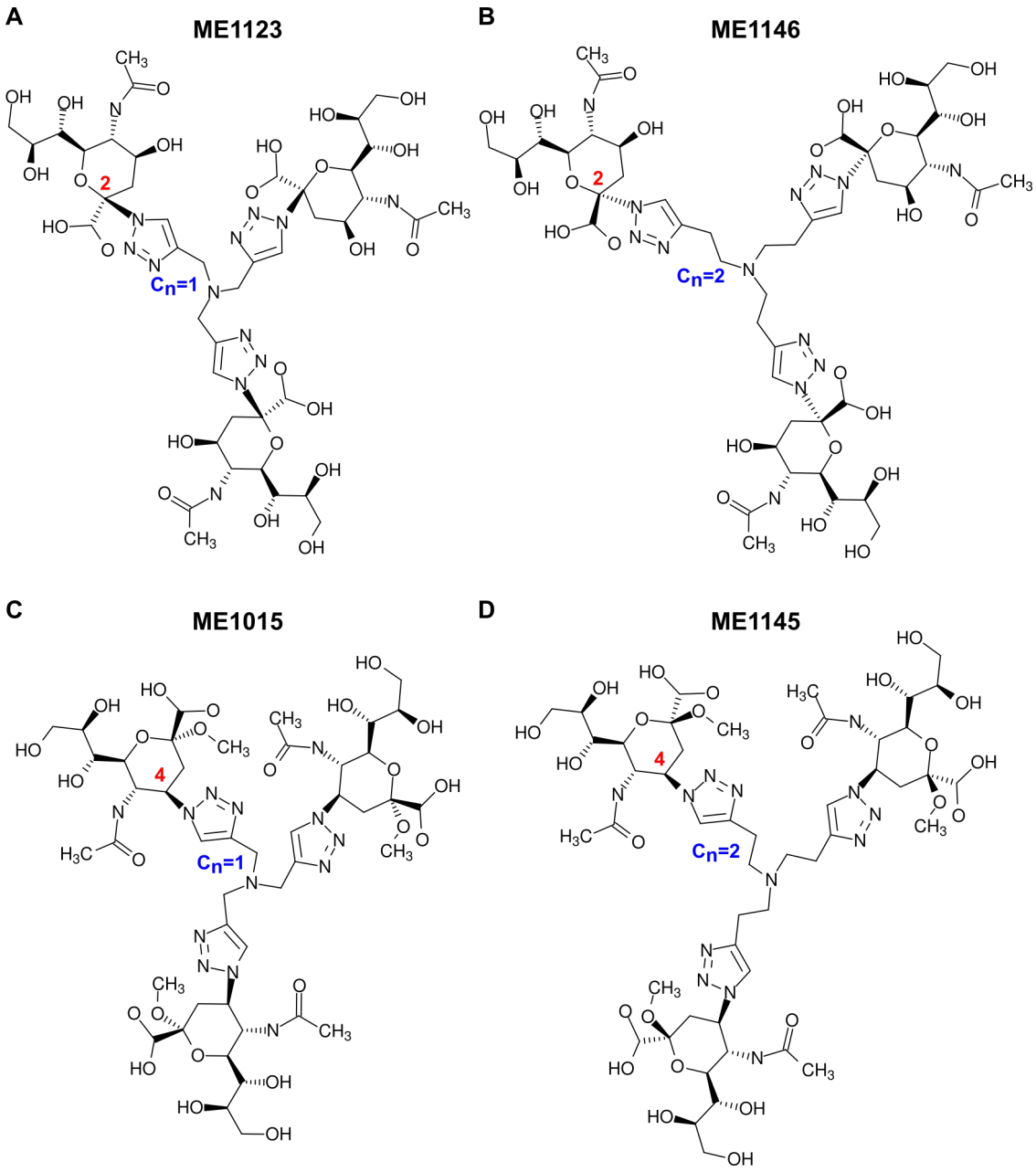

Figure 14) 3rd generation of trivalent sialic acid inhibitors. A–D: Chemical structures of ME1123 (A), ME1146 (B), ME1015 (C), and ME1145 (D). The sialic acid carbon, which is linked to the triazole group, is labeled in red, the spacer length in blue.

Additionally to HAdV37, crystal structures of HAdV36 and HAdV26 in complex with the 3rd generation inhibitors were solved to evaluate binding of these compounds to further HAdV serotypes.

5.1.1 Crystallization, Data Collection, and Data Processing

5.1.1.1 Crystallization of HAdV37 FK

The HAdV37 FK was purified and crystallized as described before (see Figure 15 A and Figure S1) and soaked for 1.5–16 h with 20 mM of each compound prior to data collection at the SLS beamline X06DA (PXIII) [164]. Crystals grew in space group P 21 with one HAdV37 FK trimer per asymmetric unit and diffracted to high resolution in a range of 1.54–2.05 Å. The phase problem was solved by molecular replacement using the published coordinates of the HAdV37 FK (PDB ID *1uxe*). For refinement, three-fold NCS restraints and either TLS or anisotropic B-factor refinement were applied. Data collection and refinement statistics are summarized in Table S1.

5.1.1.2 Crystallization of HAdV36 FK

The HAdV36 FK was purified and crystallized as described previously [214]. In summary, His-tagged HAdV36 FK (amino acids 168–373) was expressed in *E. coli* cells and purified by IMAC from the cleared cell lysate. The affinity tag was removed by TEV cleavage and subsequently a SEC for polishing and a second IMAC to remove uncleaved protein were performed (see Figure S3). The protein was concentrated to approximately 8 mg mL^{-1} and cocrystallized with 1–10 mM of each inhibitor (see Figure 15 B). Crystals grew in space group P 21 21 2 (for ME0462) or P 21 21 21 (all other ligands) containing one HAdV36 FK trimer per asymmetric unit. Data sets were obtained to high resolution of 1.25–2.30 Å and the phase problem was solved by molecular replacement using the coordinates of unliganded HAdV36 FK [Manuel Liaci, personal communication]. Three-

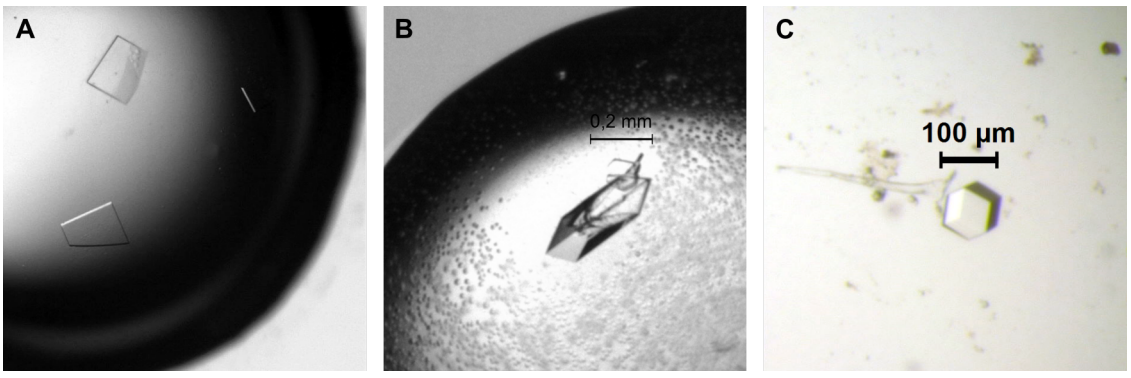

Figure 15) **Representative crystals of HAdV37-, HAdV36-, and HAdV26-inhibitor complexes. A:** HAdV37 FK crystals soaked with ME1146. **B:** Cocrystal of HAdV36 FK with ME1145. **C:** HAdV26 FK crystal soaked with ME1015.

fold NCS restraints and either TLS or anisotropic B-factor refinement were applied for refinement. Data collection and refinement statistics are summarized in Table S2.

5.1.1.3 Crystallization of HAdV26 FK

For purification of HAdV26 FK, amino acids 178–373 with a N'-terminal His-tag were expressed in *E. coli* cells and purified from cleared cell lysate by IMAC. After cleavage of the affinity tag by trypsin overnight, uncleaved protein was removed by a second IMAC step and a final SEC was performed for polishing (see Figure S2). The protein was crystallized at 20 °C overnight, and crystals were soaked with 20 mM inhibitor for 1.5–4 h (see Figure 15 C). Crystals grew in the cubic space group P 21 3 containing one protomer of the HAdV26 FK in the asymmetric unit, where the FK trimer is formed by a crystallographic three-fold axis. Data were collected to high resolution ranging from 1.10–1.65 Å. The phase problem was solved by molecular replacement using the published coordinates of HAdV26 FK (PDB ID *6fjn*), and for refinement three-fold NCS restraints as well as anisotropic B-factor refinement were applied. Data collection and refinement statistics are summarized in Table S3.

5.1.2 Structures of C2-linked Inhibitors

Both ME1123 and ME1146 display comparable electron density in the respective FK crystal structure despite different *spacer* length, hence only data for ME1123 are shown here representatively (see Figure S5 for ME1146). In HAdV37 as well as HAdV26 complexes, complete electron density is observed for each ME1123 and ME1146, which allowed modeling of the whole ligand unambiguously into the difference electron density map. Calculation of a simulated annealing omit difference electron density map omiting the inhibitor and atoms in 5 Å proximity confirmed the ligand density (see Figure 16 A and C). Interestingly, both HAdV37-ME1146 and HAdV26-ME1146 structures showed additional electron density in a cavity at the center of the three triazole rings, which is described in more detail in section 5.1.5.

In contrast, the maps for HAdV36 displayed only partial electron density for both ligands. While for ME1146 at least all three sialic acid moieties could be fully modeled, the ME1123 dataset allowed only modeling of two of the sialic acids (see Figure 16 B). A crystal contact at one of the sites stabilizes the C8- and C9-hydroxyl groups of the sialic acid, resulting in a clearly better resolved glycerol chain at the C6 carbon. From

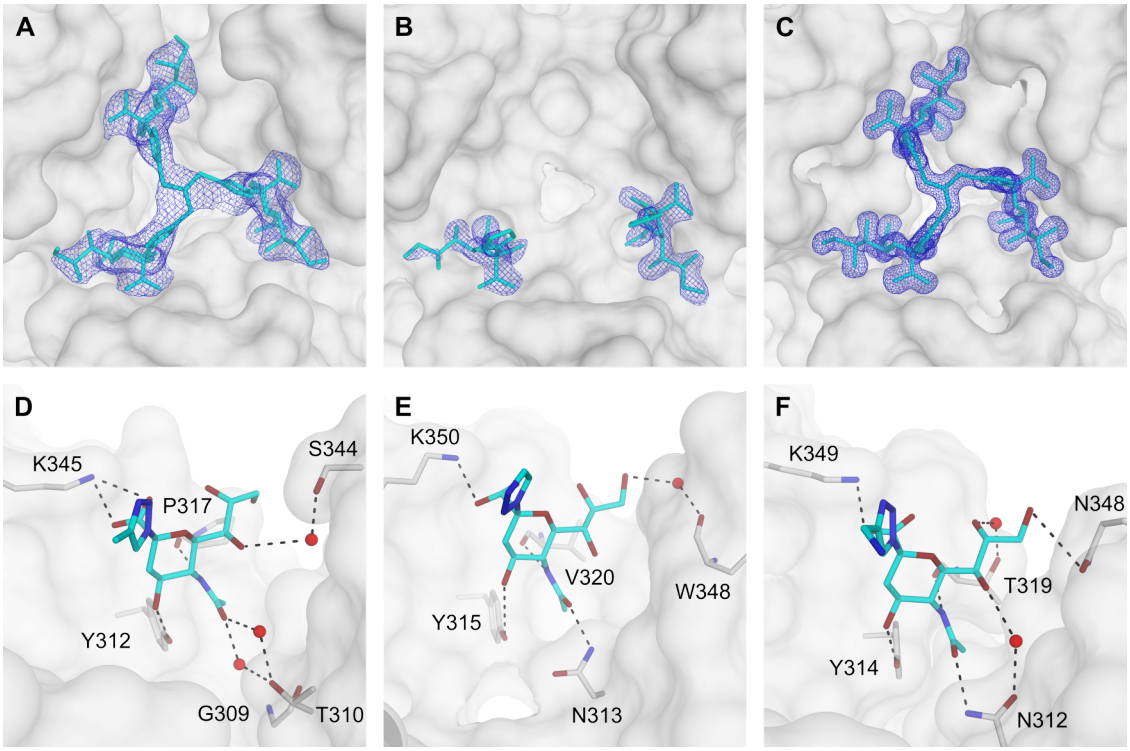

Figure 16) **Difference electron density maps and intermolecular interactions of ME1123 in complex with HAdV37, HAdV36, and HAdV26. A–C:** Simulated annealing omit difference electron density maps of HAdV37 FK (**A**), HAdV36 FK (**B**), and HAdV26 FK (**C**) oF ME1123 depicted as blue meshes at a level of 3 σ and a radius of 1.6 Å around the ligand. **D–F:** Intermolecular interactions of HAdV 37 FK (**D**), HAdV36 FK (**E**), and HAdV26 FK (**F**) with ME1123. Water molecules are displayed as red spheres and hydrogen bonds as black dashed lines.

the *spacer* and *core* segments of ME1123, only the triazole ring atoms could be modeled into the electron density map. However, the distance between the triazole rings is too large to be connected by the remaining *spacer* atoms of a single inhibitor molecule.

The intermolecular interactions between inhibitor and FK are similar for all three HAdVs. Direct hydrogen bonds from one protomer are formed by a lysine, tyrosine, and the backbone of either proline, valine or tyrosine residues to the inhibitors' C2-carboxyl, C4-hydroxyl, or N-acetyl groups, respectively. In HAdV37, the binding groove is slightly wider compared to HAdV36 and HAdV26, therefore water-mediated hydrogen bonds via S344 to the C7-hydroxyl and via G309 as well as T310 to the N-acetyl group are formed from the second protomer. HAdV36 forms a water-mediated hydrogen bond via W348 to the C9-hydroxyl and a direct hydrogen bond via N313 to the N-acetyl. The HAdV26 binding pocket is the narrowest and forms direct contacts to the sialic acid via N348 to the C9-hydroxyl and via N312 to the N-acetyl as well as via a neighboring water molecule to the C7-hydroxyl group.

All of the structures share that the triazole ring is pointing upwards from the sialic acid towards the center of the FK trimer. This results in an elevated position of the *core* amine on top of the fiber knob, leading to a "bell-like" conformation of the whole inhibitor molecule. Unfortunately, this shape seems not suitable for HAdV36, as all three binding sites were never fully occupied by a single inhibitor molecule of either ME0462, ME1123, or ME1146. However, the HAdV36 FK was recently shown to bind a rare 4-O-acetylated sialic acid variant in glycan array experiments as well as in crystal structures [Liaci et al., unpublished manuscript]. Based on these structural data, the new inhibitor variants ME1015 and ME1146 were designed, switching the linkage of the triazole *spacer* from the C2 position of the sialic acid ring to the C4 position (see Figure 14). Thereby, the native O-acetyl group of the 4-O-acetylated sialic acid variant is replaced by the triazole ring of the *spacer*, while a methyl group is attached at the C2-hydroxyl position. Crystal structures of HAdV37 FK, HAdV36 FK, and HAdV26 FK in complex with each inhibitor were solved to evaluate the ability to bind the C4-linked compounds.

5.1.3 Structures of C4-linked Inhibitors

Similar to the C2-linked inhibitors, the *spacer* length did not influence the overall binding mode of ME1146 and ME1015 significantly, hence only data for the first are shown representatively (see Figure S6 for ME1015). All three HAdV maps, including the one for HAdV36, display complete electron density for the ligands, hence they could be modeled unambiguously into the difference electron density maps. In contrast to the C2-linked inhibitors, a complete, single inhibitor molecule is clearly visible in the HAdV36 structures. Simulated annealing omit difference electron density maps confirmed the presence and conformation of the ligands in the crystal structures (see Figure 17 A–C).

The sialic acid moiety is bound similarly to the C2-inhibitor structures, with one altered hydrogen bond from the FK tyrosine, which is now formed to the triazole ring instead of the C4-hydroxyl group. Interestingly, the HAdV26-ME1145 complex is the only exception to this: Here the triazole ring is flipped in a way that no interaction to Y314 is possible (further details see section 5.1.5).

The switch of the *spacer* to the C4 position at the sialic acid ring influences the overall conformation of the inhibitor. The triazole ring is now pointing downwards into the center of the trimeric fiber knob interface, placing the *core* nitrogen slightly

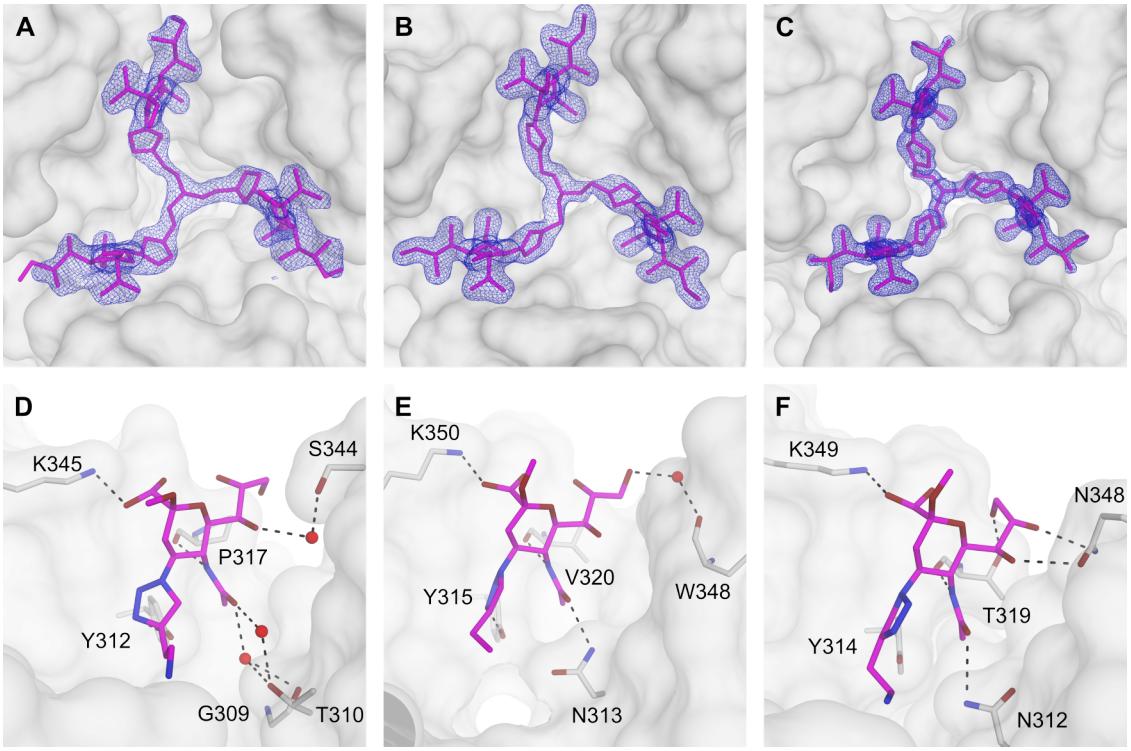

Figure 17) **Difference electron density maps and intermolecular interactions of ME1145 in complex with HAdV37, HAdV36, and HAdV26. A–C:** Simulated annealing omit difference electron density maps of HAdV37 FK (**A**), HAdV36 FK (**B**), and HAdV26 FK (**C**) oF ME1123 depicted as blue meshes at a level of 3 σ and a radius of 1.6 Å around the ligand. **D–F:** Intermolecular interactions of HAdV 37 FK (**D**), HAdV36 FK (**E**), and HAdV26 FK (**F**) with ME1145. Water molecules are displayed as red spheres and hydrogen bonds as black dashed lines.

below the level of the sialic acid moieties. Overall, the inhibitor molecules adopt rather a ”goblet-like” conformation instead of a ”bell”. This conformation allows the inhibitor to occupy all three binding sites of the HAdV36 FK simultaneously. However, apart from the hydrogen bond of the triazole ring, there were no additional interactions to the FK enabled by this conformational switch.

5.1.4 Steric Influence of the Linker Switch

The first step in analyzing the steric influence of the linker switch is the superimposition of the native, monovalent sialic acids in complex structures of HAdV37 (PDB ID *1uxa*), HAdV36 (Manuel Liaci, personal communication), and HAdV26 (PDB ID *6qu8*). This reveals a slightly shifted position of the sialic acids in each FK (see Figure 18 A, left panel). The HAdV36 FK-bound sialic acid (green) is located slightly further outside and, additionally, pushed towards the opposite protomer compared to HAdV37 (blue).

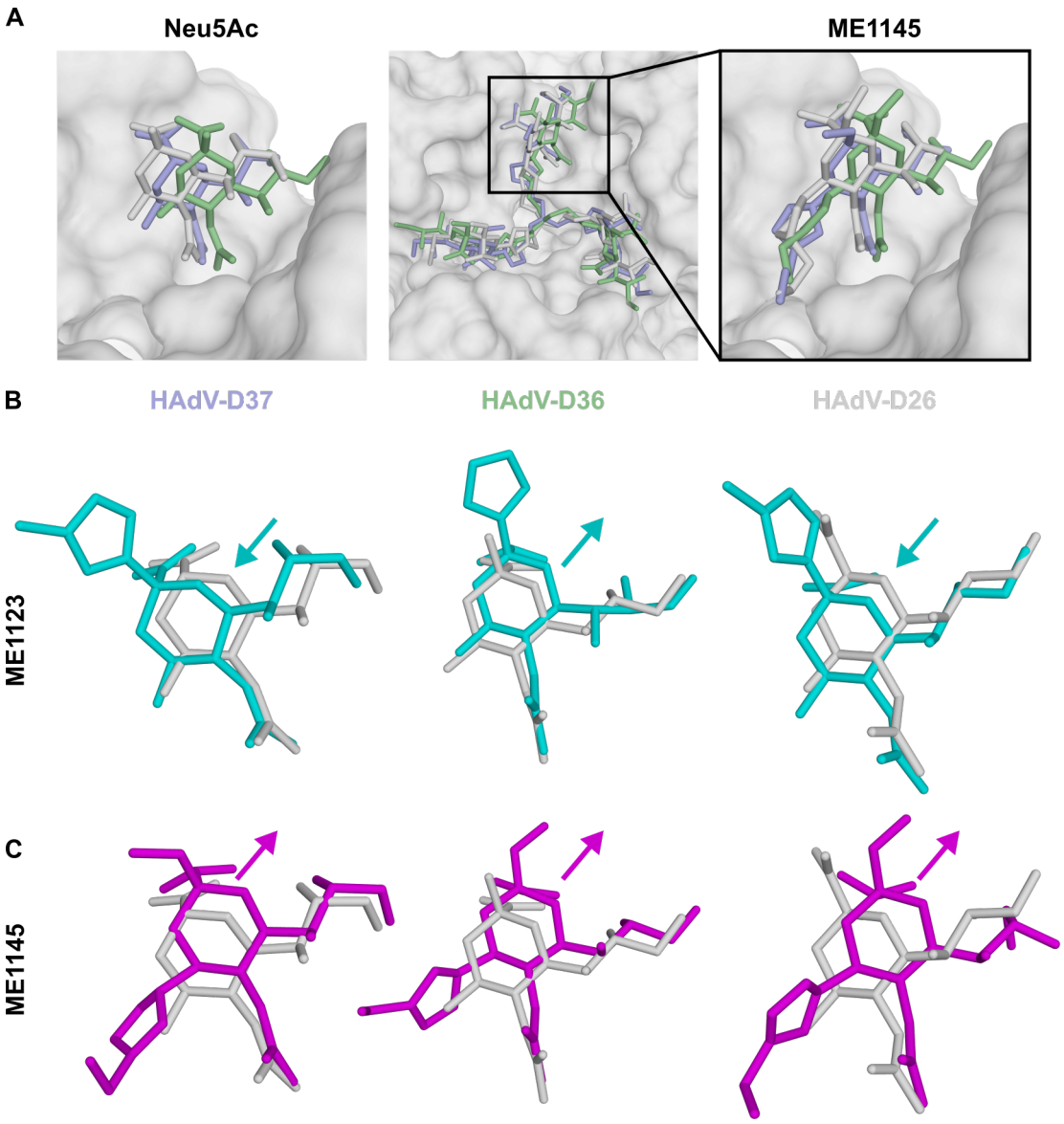

Figure 18) **Sialic acid ring shifts at the binding site. A:** Superimposition of Neu5Ac (left) and ME1145 (middle: overview; right: close-up view) in binding pockets of HAdV37 (blue), HAdV36 (green), and HAdV26 (white). Neu5Ac and ME1145 are displayed in stick representation, HAdV26 trimer in surface representation as orientation. **B:** Relative shift of ME1123 (cyan) compared to Neu5Ac (white) at HAdV37 (left), HAdV36 (middle), and HAdV26 (right) indicated by arrows. **C:** Relative shift of ME1145 (magenta) compared to Neu5Ac (white) at HAdV37 (left), HAdV36 (middle), and HAdV26 (right) indicated by arrows.

At HAdV26 (white), the carbohydrate sits slightly elevated and further inside towards the center of the binding pocket.

A similar placement is also observed upon superimposing the inhibitors in a second step, exemplified at the well-resolved ME1145 (see Figure 18 A, middle and right panel).

The inhibitor's sialic acid group in the HAdV36 binding pocket is positioned further outside and closer to the opposing protomer compared to HAdV37. In HAdV26, it is still located rather towards the center of the FK trimer, but closer to the HAdV37 inhibitor position as in the monovalent sialic acid structures.

Finally, the relative position of the inhibitor's sialic acid group compared to monovalent sialic acid within each FK domain is examined for the C2-linked ME1123 and the C4-linked ME1145 (see Figure 18 B and C). For ME1145, which is completely modeled in all crystal structures, a similar up- and outward shift of the pyranose ring is evident in all three HAdV structures. Importantly, the binding interface of the FKs is not altered significantly, only the inhibitor molecule is displaced. In contrast, the ME1123 pyranose ring is shifted in- and downwards only in the well resolved HAdV37 and HAdV26 crystal structures, while the partial inhibitor molecule at HAdV36 is displaced in the contrary direction. Noticeably, the distance of the amino acids Y315 and N313, which are closest to the center of the FK trimer and interacting with the C4-hydroxyl and N-acetyl at the C5 position of sialic acid, is shorter at HAdV36 (4.1 Å) compared to HAdV26 (4.8 Å) and HAdV37 (6.0 Å)(see Figure 17 D–F), thus making the binding pocket narrower at this position. Especially Y315 is more protruding and a potential obstacle, while HAdV37 and HAdV26 provide a more open and flexible binding cavity towards the center of the FK domain. In summary, the relative position of the inhibitors' sialic acid moieties is clearly linked to the ability of occupying all three binding sites simultaneously with a single molecule.

5.1.5 Zinc Chelating Ability of ME1146

The ligand binding site of the HAdV37-ME1146 crystal structure revealed additional electron density at the center of the triazole ring arrangement, which could not be explained by the ligand or water molecules (see Figure 19 A). Similar density is also present in the HAdV26-ME1146 as well as the HAdV26-ME1145 crystal structures. However, in these cases it is directly located on the crystallographic three-fold axis, therefore a conclusive evaluation remains challenging. The additional electron density at the HAdV37-ME1146 structure after ligand refinement appears well coordinated and resembles a metal ion binding site. Since the crystallization condition of HAdV37 FK contains 50 mM zinc acetate and all published HAdV37 crystal structures have several zinc atoms modeled at crystal contacts [164, 167, 169, 170], the additional density at the

ME1146 binding site was suspected to be a Zn^{2+} ion.

To confirm this, two additional datasets at the high remote end (1.2821 Å) and low remote end (1.2848 Å) of the zinc absorption edge were collected and an anomalous double difference electron density map was calculated, displaying anomalous difference density for zinc atoms only. Obvious peaks at a level of 8 σ were observed at three crystal contacts as well as at the proposed position in the ligand binding site (see Figure 19 B). The zinc ion is coordinated trigonal bipyramidal by three nitrogen atoms of the triazole *spacers* in the equatorial plane, and the *core* nitrogen from the top and a water molecule from the bottom in axial positions. The distance between Zn and N or O varies between 1.86–2.32 Å. In the HAdV26-ME1145 crystal structure the possible coordination of zinc or any similar metal ion leads to a flip of the triazole ring, which prevents hydrogen bonding to Y314. However, the Zn^{2+} binding does not influence the overall position and orientation of the sialic acid in the FK binding sites.

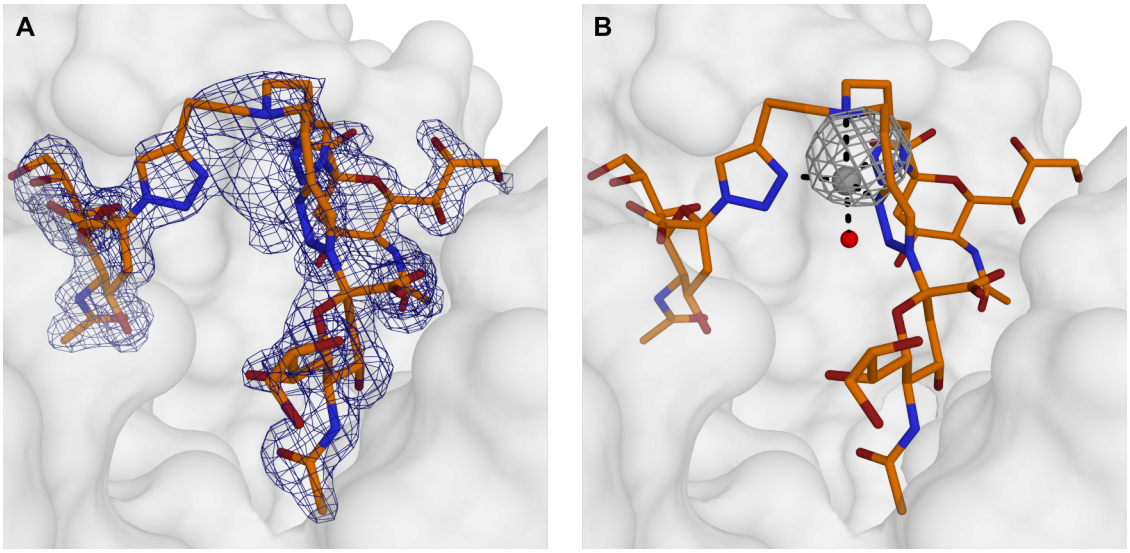

Figure 19) **Zinc binding of ME1146. A:** Simulated Annealing omit difference electron density map depicted as blue mesh at a level of 3 σ reveals additional electron density in between *spacer* and *core* of the inhibitor molecule. **B:** Anomalous double difference electron density map displayed as grey mesh at a level of 8 σ around the Zinc ion (grey), which is complexed trigonal bipyramidal by three nitrogen atoms of the triazole *linkers* in the equatorial plane, and by the central nitrogen of the inhibitor from the top and a water molecule from the bottom in the axial positions.

5.2 Discussion

5.2.1 Structural Comparison of the Inhibitor Binding Modes

In the HAdV37 complex crystal structures, the C2-linked compounds ME1123 and ME1146 are fully resolved in the electron density map. No additional contacts were observed compared to ME0462, that could stabilize the binding and explain the additional electron density. However, the altered and shortened linkage of ME1123 and ME1146 allows for less possible conformations and makes the compounds slightly more rigid. This could explain the improved electron density at this area of the complex structure. Furthermore, it could potentially also lead to a higher binding affinity, if the conformation given by the *spacer* fits ideally into the binding pocket. After initial binding of the first sialic acid moiety, either subsequent or simultaneous binding of the remaining groups is facilitated. However, too much rigidity is also disadvantageous, since a certain flexibility is required for docking of the molecule.

The ”bell-like” conformation of the C2-linked compounds pulls the sialic acid groups inwards to some extent. Therefore, some open space is required at the center of the FK. While this is feasible for HAdV37 and HAdV26, the HAdV36 binding pocket does not allow this. The gatekeeper tyrosine identified by Liaci et al [unpublished manuscript] plays a crucial role here. The gate formed by Y315 and N313 is much more closed for HAdV36 compared to HAdV37 and HAdV26. This puts more steric pressure on the pyranose ring and blocks a movement towards the inside. Therefore, binding of a single inhibitor molecule with all three sialic acid groups is not possible.

To circumvent the steric obstacle, the linkage of the *spacer* to the sialic acid was switched from C2 to C4 at the pyranose ring. This results in a ”goblet-like” conformation of the whole inhibitor molecule, where the *spacer* is pointing downwards into the center of the FK, which may seem counter-intuitive at first glance. But due to this conformation, the sialic acid group is slightly shifted up- and outwards. This movement facilitates the arrangement of the inhibitor around the gatekeeper Y315, which lies in a pocket created by the triazole – C4 – C5 – N-acetyl branch (see Figure 18 C middle panel). Y315 forms a hydrogen bond with the triazole nitrogen and a van-der-Waals contact to the N-acetyl. This allows a stable docking of the complete inhibitor molecule at all three sialic acid binding sites simultaneously.

5.2.2 Biological Inhibition Efficacy Depends on HAdV Type

To evaluate the biological inhibition efficacy, infection inhibition assays using A549 cells were performed (by Dr. David Persson and Katarina Danskog). An improved inhibition potency was determined for the C2-linked 3rd generation inhibitors for HAdV37. Compared to the 2nd generation ME0462, ME1123 shows a 100-fold decreased IC50, hence a much smaller concentration is required to achieve significant inhibition of infection (see Figure 20). The second C2-linked 3rd generation inhibitor ME1146 achieved still better inhibition than ME0462, but not as good as ME1123. Probably the length of the *spacer* influences the affinity, although there was not a big difference observable in the crystal structure. The inhibitor concentrations were high enough to reach full occupancy in the

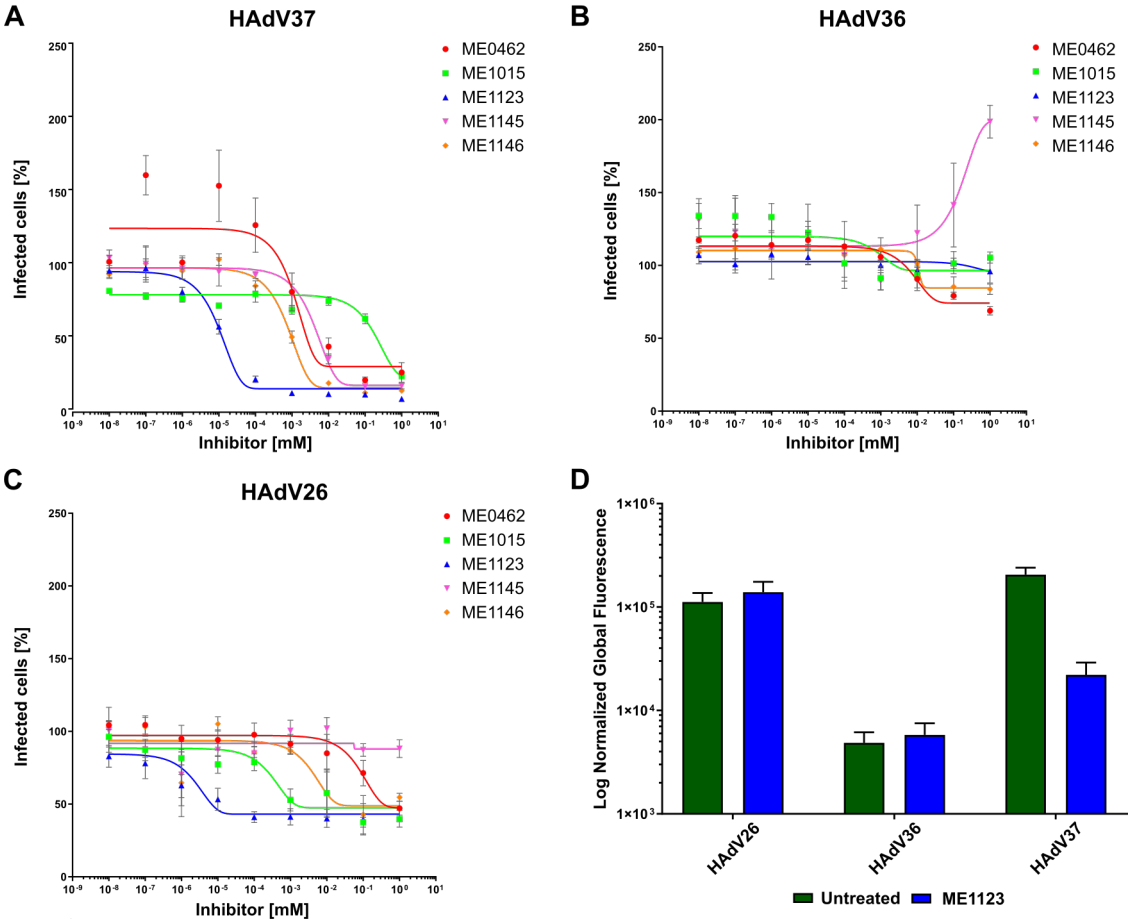

Figure 20) Biological evaluation of inhibitors using A549 cells. A: Infection of HAdV37 at different concentrations of inhibitors. **B:** Infection of HAdV36 at different concentrations of inhibitors. **C:** Infection of HAdV26 at different concentrations of inhibitors. **D:** Re-infection experiment of A549 cells using virus pretreated with ME1123. Data provided by Dr. David Persson and Katarina Danskog.

electron density map. In a biological context, ME1146 might be slightly too large due to the elongated linker for ideal docking into the fiber knob pocket, hence the IC50 concentration is slightly worse compared to ME1123. The C4-linked compounds also show a clear inhibitory effect, however with significantly higher IC50 concentrations, and as such they are less effective than ME0462. Apparently, the "goblet-like" conformation is less favorable for HAdV37 binding in general.

The total infectivity is reduced to ca. 20 % upon saturation of the inhibitor. This indicates that sialic acid is probably the primary attachment receptor for HAdV37, but nevertheless a minor amount of virus escapes via an alternative pathway. HAdV37 was for example shown to bind CAR, which might aid as escape mechanism in case sialic acid based cell attachment blocked [144]. A similar phenomenon is also observed for HAdV56 (see subsection 4.2.2) and seems to be not uncommon for adenoviruses.

For HAdV36, there is almost no inhibitory effect observed for all five compounds. Even the C4-linked compounds, which were very well resolved in the complex crystal structures, show no significant effect up to 1 mM. There are two possible explanations for this: (i) the affinity is too low to see an effect with the concentrations used in this assay or (ii) sialic acid is not the main attachment receptor for HAdV36. Liaci et al. [unpublished manuscript] observed an inhibitory effect of Neu5Ac only for concentrations above 10 mM, similar to HAdV37. However, while for HAdV37 the trivalency of the compounds led to a significantly increased affinity well below the millimolar range, this does not seem to be the case for HAdV36. On the other hand, it cannot be excluded that there is an alternative receptor which predominantly mediates host cell attachment. CAR was also reported to interact with the HAdV36 FK by Liaci et al. and could thus be the potential primary attachment receptor. More biological data will be needed to clarify the receptor preference of HAdV36.

At HAdV26 infection inhibition assays, ME1123 reaches the lowest IC50 concentration, ahead of ME1015 and ME1146. For this serotype, the type of linkage appears to be less important compared to the length of the *spacer*, since the two most potent inhibitors both comprise the shorter linker. This is consistent with the observation that monovalent sialic acid is closer to the center of the binding pocket for HAdV26 (8.4 Å average distance of C3 atoms) compared to HAdV36 (9.4 Å) and HAdV37 (9.2 Å) (see Figure 18 A left panel). The only compound showing no effect up to a concentration of 1 mM is ME1145. Possibly due to a combination of the goblet-like shape and the elongated *spacer*, this compound is slightly too large and binds only with low affinty.

The crystal structure was soaked with a concentration of 20 mM, which was apparently sufficient to achieve full occupancy in the calculated electron density map.

However, the overall infectivity does not decrease below ∼50 % upon saturation of the inhibitor. This is rather different to HAdV37, where the infectivity is reduced to ∼20 %. It is quite possible that there are additional attachment receptors that mediate infection to the A549 cells. Several different attachment receptors have been postulated in recent studies. Baker et al. describe sialic acid as primary attachment receptor. However, they used a pseudotyped HAdV5 vector equipped with a HAdV26 FK, therefore all interactions by other HAdV26 capsid proteins are excluded in this experimental setup [163]. In the meantime, it was shown that the HAdV26 hexon contributes to viral infection via CD46 [239]. Another study by Li et al. also confirmed the dependence on CD46 for infecting human blood and dendritic cells by blocking CD46 on the cell surface with antibodies [251]. Recently, Hemsath et al. confirmed that CD46 is the predominant attachment receptor and can substitute sialic acid, but sialic acid is still capable of providing some level of infectivity [252]. The results from a study by Nestic et al. can be interpreted similarly [253]. A CD46 knockout by siRNA reduced infectivity of HAdV26-FK35, which served as negative control, but it did not influence HAdV26 infectivity. This strengthens the above mentioned hypothesis, as HAdV26 could still escape the CD46-dependent pathway by usage of sialic acid, while HAdV26-FK35 is unable to do so. HAdV35 belongs to group B HAdVs and binds CD46 with its FK, but probably not sialic acid [254]. A knockout of $\alpha v\beta 3$ integrin in this study significantly reduced infectivity of both viruses. In summary, these findings of all studies fit very well with the role of integrins rather for cell entry than for cell attachment. CD46 is probably the primary attachment receptor, but also sialic acid can mediate infectivity to some extent.

In a reinfection experiment, cells were first infected by HAdVs and later an inhibitor was added to prevent reinfection of further cells. While no effect was observed for HAdV26 and HAdV36, consistent with the infection inhibition assays, HAdV37 exhibited a diminished infectivity after ME1123 treatment (see Figure 20 D). Therefore, inhibitor treatment could indeed slow down viral proliferation and reduce the total number of infected cells compared to the untreated sample. Hence, targeting the sialic acid binding site is a valid strategy for developing antiviral agents against HAdV37.

5.2.3 Zinc Binding

The additional electron density in the complex crystal structure of ME1146 binding to HAdV37 FK was proven to be a Zn^{2+} ion by a double anomalous difference electron density map around the zinc absorption edge. Since the crystallization condition contains zinc acetate, it is likely to be a crystallization artifact. Nevertheless, it is possible that zinc replaced another metal ion, e.g. Cu^{2+}, which is used as catalyst during the synthesis and could be leftover from there. This could explain additional density in the HAdV26-ME1145 and ME1146 complex structures. Their crystallization condition does not contain any zinc, but the conformation of the inhibitor still resembles coordinating a charged metal ion. However, its location directly on the crystallographic three-fold axis make a conclusive evaluation challenging in these cases.

The zinc does not influence the positioning of the sialic acid groups compared to the other C2-linked compound ME1123. Theoretically, it could favor a certain pre-conformation of the compound due to the trigonal-bipyramidal metal coordination, however the presence of zinc during infection inhibition assays did not reveal any significant influence. Rather, the conformation of the inhibitor seems to be a prerequisite for the binding of the metal ion and not vice versa. Potentially, ME1123 could be used to extract copper out of solutions, using the HAdV37 FK to capture the compound-copper complex.

In summary, the structure-guided approach resulted in a new generation of inhibitor molecules that show increased inhibition potency against HAdV37. These inhibitors also target another serotype, HAdV26, and show a partial inhibitory effect. Switching the linkage to the C4 carbon enables binding to an additional third serotype, HAdV36, which was previously not able to bind a single trivalent inhibitor molecule. The target range of the compounds is extended and a structural foundation is established to explain the different binding behavior. This expands the toolbox for generating other compounds, which need not necessarily be limited to sialic acid, but could also involve other terminal units. This proof of concept is also valuable for the design of other multivalent molecules targeting symmetrical interfaces or other sialic acid-binding proteins. It was shown that structural biology is a powerful approach for the development and validation of tailor-made drug candidates.

6. Novel Binding Mode of the Neural Receptor NgR1 to the Reovirus Capsid

Contribution of others

The NgR1 and $\mu1_3\sigma3_3$ expression plasmids as well as purified T3SA- reovirus were provided by Dr. Danica Sutherland and Prof. Dr. Terence Dermody, Department of Pediatrics, University of Pittsburgh School of Medicine, Pittsburgh, Pennsylvania, USA. Initial cryoEM data were collected during my two week visit at the group of Prof. Dr. B. V. V. Prasad, Verna and Marrs McLean Department of Biochemistry and Molecular Biology, Baylor College of Medicine, Houston, Texas, USA. Final cryoEM data collection was carried out by Dr. Xinzhe Yu, Dr. Liya Hu, Prof. Dr. Zhao Wang and Prof. Dr. B. V. V. Prasad. Patrick Woerz assisted during his bachelor's thesis with protein purification, analytics and complex formation assays under my supervision [255].

6.1 Results

The aim of this part of the thesis is to structurally characterize NgR1-binding to ReoVs. NgR1 is likely to bind σ3, which was shown in infection assays by Konopa-Anstadt et al. [187]. Since σ3 is part of the heterohexameric capsomer $\mu1_3\sigma3_3$, the latter was used for binding studies and complexation assays with either His- or Fc-tagged recombinant NgR1.

6.1.1 Purification of NgR1

6.1.1.1 Purification of His-tagged NgR1

The NgR1-His expression plasmid encodes for the extracellular domain of NgR1 (amino acids 1–310) and a C'-terminal His6-tag. The recombinant protein was expressed and secreted by Freestyle™ 293F cells in suspension culture for 7 d. The supernatant was

sterile-filtered and initially purified by IMAC, resulting in already quite pure NgR1-His (see Figure 21 A). SDS-PAGE analysis of NgR1-His showed two bands at 35 kDa and 40 kDa, corresponding to different glycosylation states according to Barton et al. [192]. Subsequently, a SEC was performed for polishing, which revealed a sharp NgR1-His peak in the chromatogram and removed a small soluble aggregate peak (see Figure 21 B).

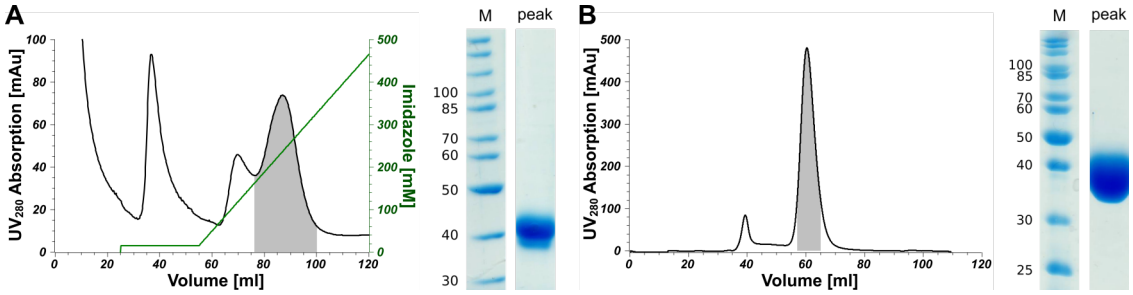

Figure 21) **Purification of His-tagged NgR1. A:** IMAC chromatogram of NgR1-His showing three peaks overall, where the third revealed a double band for NgR1-His at 35–40 kDa at SDS-PAGE analysis. **B:** SEC chromatogram of NgR1-His showing a small aggregate peak and a single, sharp peak of monomeric NgR1-His with two overlapping bands at 35–40 kDa at SDS-PAGE analysis.

6.1.1.2 Purification of Fc-tagged NgR1

Recombinant NgR1-Fc contains a C'-terminal Fc-tag instead of a His-tag and is expressed using similar conditions in Freestyle™ 293F cells. Initial Protein A affinity chromatography results in already quite pure NgR1-Fc, showing a smeary band at 60–70 kDa (see Figure 22 A) at SDS-PAGE analysis, which is presumably due to glycosylation, similar as for NgR1-His. The additional high-molecular weight band at the SDS-PAGE gel is assigned to an aggregation artifact of SDS-PAGE sample preparation. A final SEC

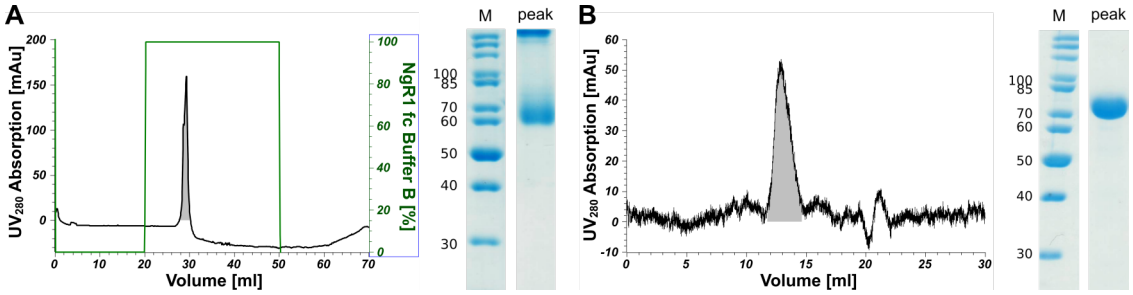

Figure 22) **Purification of Fc-tagged NgR1. A:** Protein A chromatography chromatogram of NgR1-Fc showing a single peak as well as a single band at 60–70 kDa at SDS-PAGE analysis. **B:** SEC chromatogram of NgR1-Fc showing a single peak of dimeric NgR1-Fc and a band at 60–70 kDa at SDS-PAGE analysis.

reveals a single peak in the chromatogram for the NgR1-Fc dimer and pure NgR1-Fc at SDS-PAGE analysis (see Figure 22 B).

6.1.1.3 Glycoslation of NgR1

To further characterize the predicted glycosylation sites of NgR1, the amidase PNGase F was used to cleave off the glycans of NgR1. The samples were subsequently analyzed by SDS-PAGE (see Figure 23 A). Both NgR1-Fc and NgR1-His displayed a loss of 5–10 kDa in weight after PNGase F treatment. Interestingly, the double band of NgR1-His was still present at SDS-PAGE analysis after glycan cleavage. Therefore it is unlikely, that varying glycosylation is responsible for the double band. Subsequent analysis of the NgR1 sequence (UniProt ID *Q9BZR6*) using the SignalP v. 5.0 server [210] revealed a 26 amino acid long N-terminal signal peptide and a 40 % probability of a *AAP/CP* cleavage site afterwards. This corresponds to a difference in molecular weight of 2.9 kDa, which matches the difference of the two bands at SDS-PAGE analysis. Therefore, the two bands probably represent cleaved and uncleaved fractions of NgR1-His.

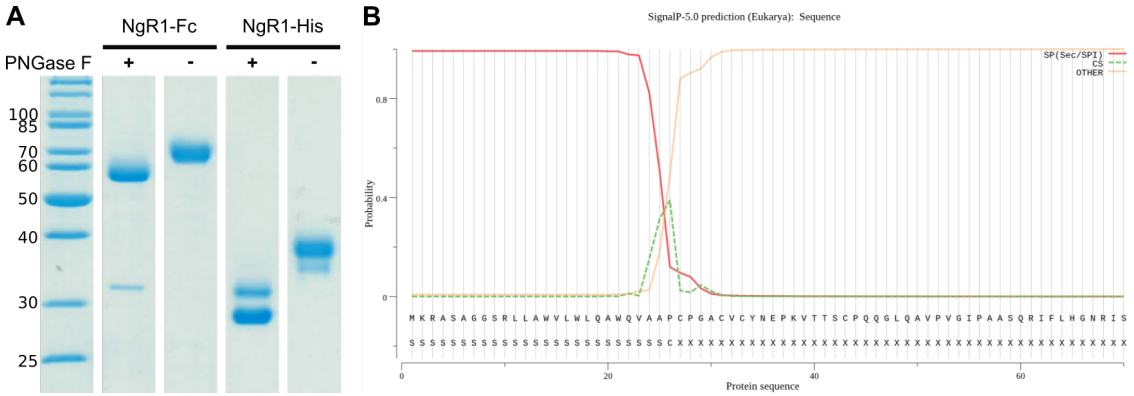

Figure 23) **Glycosylation analysis of NgR1. A:** SDS-PAGE analysis of the deglycosylation assay revealed a shift of NgR1-Fc before (60–70 kDa) and after (60–65 kDa) PNGase F digestion and also for NgR1-His before (35–40 kDa) and after (28–32 kDa). The double band for NgR1-His was still clearly evident after digestion. PNGase F has a molecular weight of 35 kDa and was visible in the NgR1-Fc (+) lane. **B:** Sequence analysis of NgR1 revealed a N-terminal 26 amino acid signal peptide and a 40 % probability of a cleavage site. Sequence analysis was performed with SignalP v. 5.0 [210].

6.1.2 Purification of $\mu 1_3\sigma 3_3$

The viral capsomer $\mu 1_3\sigma 3_3$ was expressed recombinantly in High Five™ insect cells using the baculovirus expression system. The pFastBac™ Dual vector contains two separate MCS under control of polyhedrin and p10 promoters for independent expression

of μ1 and σ3, respectively. DH10Bac cells were used for recombination of the protein encoding genes with the baculovirus encoding bacmid, which was confirmed by PCR analysis, showing a band for a ∼5,500 bp insertion into the bacmid (see Figure 24 A). To generate an initial P1 baculovirus stock, Sf9 insect cells were transfected with bacmid DNA. After 72 h, the cells showed clear signs of viral infection, such as enlarged nuclei and granular, oversized cells, which were partly lyzed (see Figure 24 B). The P1 baculovirus stock was harvested and amplified via a P2 stock to a high-titer P3 baculovirus stock, which was subsequently used for infection of High Five™ cells for protein expression.

In contrast to previously described protocols [72], the protein was secreted by the HighFive™ cells and therefore purified from the supernatant after 96 h expression time. As none of the two capsid proteins contains an affinity tag, an ion exchange chromatography was performed as first step of the purification. During gradient elution with 100–550 mM sodium chloride, continuous protein elution was observed with a peak at approximately 400 mM sodium chloride, which contained μ1 (double band for μ1 and

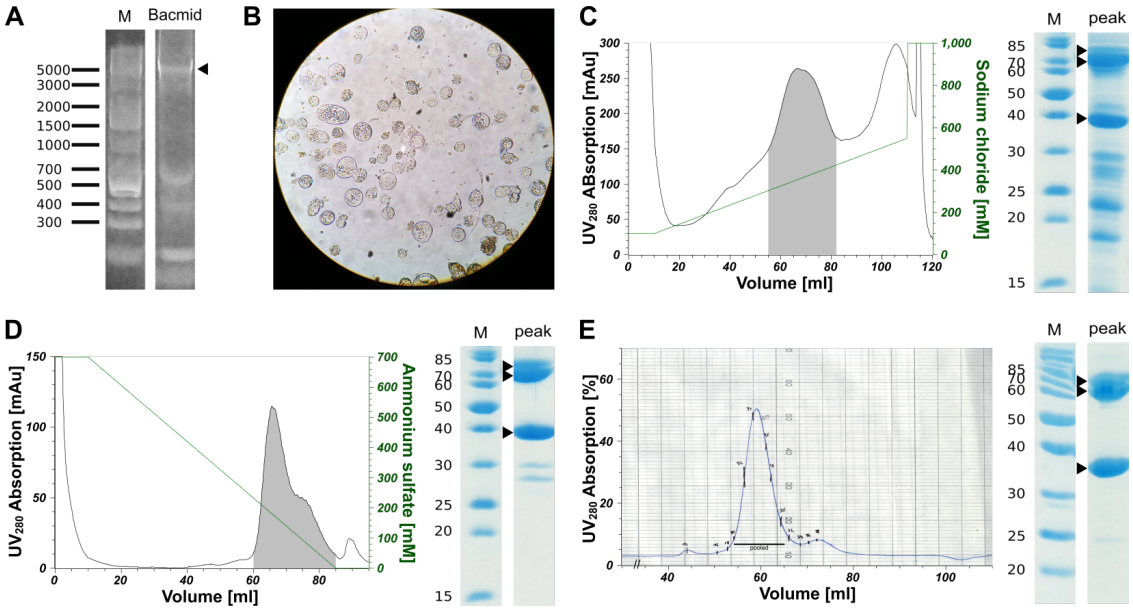

Figure 24) **Expression and purification of $\mu1_3\sigma3_3$. A:** PCR analysis confirms insertion of recombinant DNA (∼5,500 bp) into the bacmid. **B:** Sf9 insect cells show signs of viral infection: swollen cells, lysis, and granular appearance. **C:** IEX chromatogram of $\mu1_3\sigma3_3$ showing continuous protein elution with one distinct peak at 65 mL during gradient elution. SDS-PAGE analysis of the pooled peak revealed, among various impurities, a double band at 76 kDa for μ1 and a single band at 40 kDa for σ3. **D:** HIC chromatogram of $\mu1_3\sigma3_3$ showing a distinct, tailing peak containing μ1, σ3, and minor impurities at SDS-PAGE analysis. **E:** SEC chromatogram of $\mu1_3\sigma3_3$ showing a large peak containing pure $\mu1_3\sigma3_3$, as confirmed by SDS-PAGE analysis, and a separate minor peak containing impurities.

μ1c at 76 kDa) and σ3 (40 kDa) among major impurities (see Figure 24 C). The peak fractions were further purified by a hydrophobic interaction chromatography, resulting in a single, but tailing peak, containing mostly pure $\mu1_3\sigma3_3$ and minor impurities at a lower molecular weight (see Figure 24 D). These were removed by a SEC and strict pooling of peak fractions containing only pure $\mu1_3\sigma3_3$ (see Figure 24 E).

6.1.3 Attempts to Obtain a NgR1 and $\mu1_3\sigma3_3$ Complex

6.1.3.1 Gel Filtration

Having pure NgR1 and $\mu1_3\sigma3_3$ in sufficient quantity and quality in hand, complex formation trials were conducted for subsequent structural analysis. Initially, $\mu1_3\sigma3_3$ and glycosylated NgR1-His were mixed at molar ratios of 1:3 and 1:10, incubated at

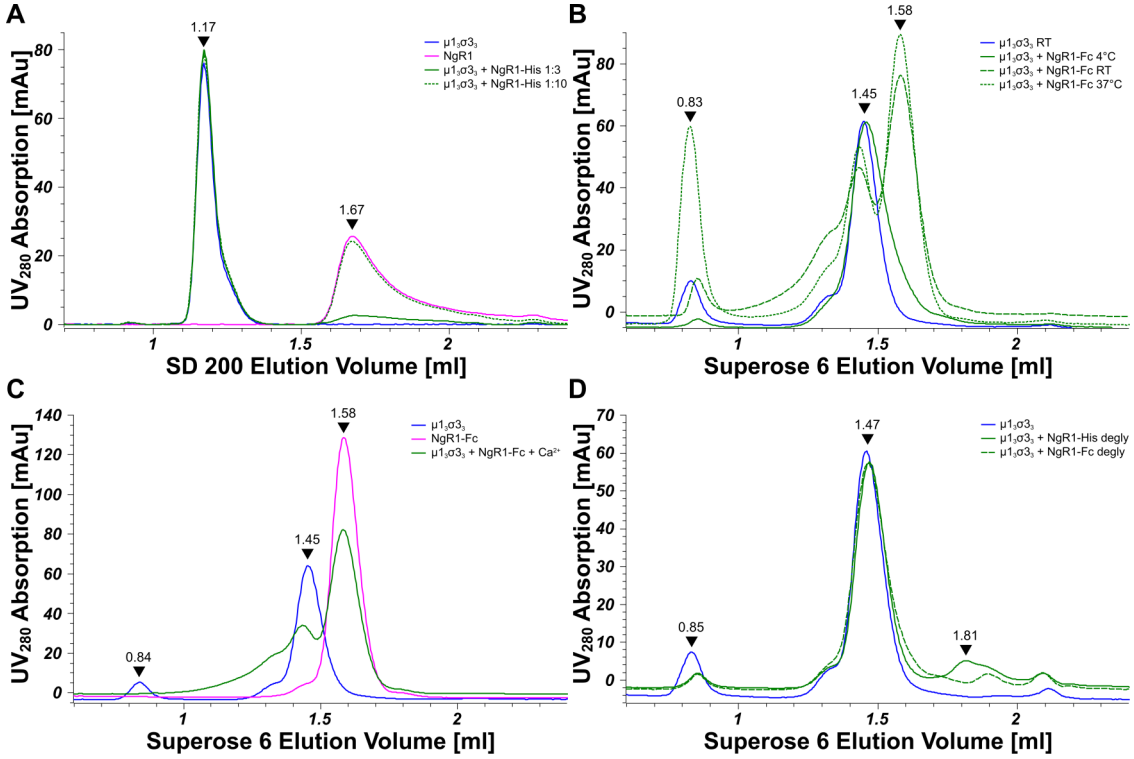

Figure 25) **Analytical SEC chromatograms of $\mu1_3\sigma3_3$ and NgR1 complex assays. A:** Analytical SEC chromatogram of $\mu1_3\sigma3_3$ (blue) and NgR1-His (magenta) incubated at molar ratios of 1:3 (olive line) and 1:10 (olive dashes). **B:** Analytical SEC chromatogram of $\mu1_3\sigma3_3$ (blue) and NgR1-Fc incubated at a molar ratio of 1:1 at 4 °C (olive line), at a molar ratio of 1:6 at RT (large olive dashes) and at a molar ratio of 1:6 at 37 °C (small olive dashes). **C:** Analytical SEC chromatogram of $\mu1_3\sigma3_3$ (blue), NgR1-Fc (magenta), and both incubated together at a ratio of 1:9 with additional 2 mM calcium chloride (olive). **D:** Analytical SEC chromatogram of $\mu1_3\sigma3_3$ (blue) incubated with deglycosylated NgR1-His (olive line) and deglycosylated NgR1-Fc (olive dashes). Peak elution volumes are indicated by black arrowheads.

4 °C for 2 h, and analyzed by analytical SEC using a SD 200 column (see Figure 25 A). A peak at an elution volume of 1.17 mL corresponds to a molecular weight of 430 kDa, which fits approximately to $\mu1_3\sigma3_3$. A second peak eluted at 1.67 mL, which matches the NgR1-His molecular weight of 35 kDa. No additional absorbance signal indicating complex formation was observed.

However, as $\mu1_3\sigma3_3$ is rather at the edge of the Superdex 200 resolution range (10–700 kDa), the Superose 6 (5–5,000 kDa) was used for the following experiments. Fc-tagged NgR1 was used to increase the molecular weight for a better separation of complexed $\mu1_3\sigma3_3$ and uncomplexed $\mu1_3\sigma3_3$, and to evaluate the influence of the affinity tag.

Additionally, different incubation temperatures were examined to test their influence on complex formation. Fc-tagged NgR1 was incubated with $\mu1_3\sigma3_3$ at 4 °C and at RT, both overnight, and at 37 °C for 2 h to avoid excessive aggregation (see Figure 24 B). NgR1-Fc eluted at a peak volume of 1.58 mL, corresponding to a molecular weight of 179 kDa, which is approximately a NgR1-Fc dimer. $\mu1_3\sigma3_3$ eluted at 1.45 mL, which corresponds to 450 kDa. The complex sample at 4 °C did not show any additional signal apart from a small aggregate peak at the void volume of 0.83 mL (>5,000 kDa). At RT, the aggregate peak was enlarged and a front shoulder appeared at the $\mu1_3\sigma3_3$ peak in both samples, with and without NgR1-Fc. Although the shoulder appeared slightly larger in the NgR1-Fc containing sample, SDS-PAGE analysis did not reveal any NgR1-Fc in the respective fraction. Incubation at 37 °C led to significantly more aggregate and an even larger shoulder, however no NgR1-Fc was detected at SDS-PAGE analysis of the corresponding shoulder fraction.

The addition of 2 mM calcium chloride to $\mu1_3\sigma3_3$ and NgR1-Fc, incubated at a 1:9 ratio overnight at RT, resulted in a similar, enlarged front shoulder without detectable NgR1-Fc by SDS-PAGE analysis (see Figure 24 C). Also deglycosylation of NgR1-His as well as NgR1-Fc by PNGase F did not facilitate complex formation with $\mu1_3\sigma3_3$ (see Figure 24 D). In conclusion, no putative $\mu1_3\sigma3_3$-NgR1 complex could be detected by gel filtration, therefore a more sensitive experiment was required to investigate the interaction.

6.1.3.2 Pulldown Assays

As an alternative technique, pulldown assays were performed to test, whether affinity beads can capture a complex in solution via affinity-tagged NgR1. Protein A/G Ultra-Link™ Resin and Ni-NTA Agarose were used for NgR1-Fc and NgR1-His, respectively. NgR1 and $\mu1_3\sigma3_3$ were incubated together overnight at 4°, subsequently incubated with the respective beads, and washed several times. Afterwards, protein was eluted with the respective elution buffer, and finally all samples including the beads were analyzed by SDS-PAGE.

The Protein A pulldown reveals NgR1-Fc bands during all washing steps, with slightly enhanced intensity at the elution sample and more significantly at the beads sample (see Figure 26 A). Bands for μ1 and σ3 were observed at the beads sample, additionally σ3 is present in the first elution sample. However, the signal intensity for all $\mu1_3\sigma3_3$ bands is very low compared to NgR1-Fc signal intensity. To exclude binding of $\mu1_3\sigma3_3$ to the Protein A resin, a control assay using only $\mu1_3\sigma3_3$ was performed, and it did not show any $\mu1_3\sigma3_3$ binding (see Figure S7).

The NTA pulldown shows a strong NgR1-His band at the first elution and medium intense bands at the second elution and the beads sample. A faint band at 76 kDa corresponding to μ1 is observed at the first elution and at the beads sample. σ3 is overlapping with NgR1-His at SDS-PAGE analysis, therefore an evaluation was not possible. In summary, there are indications for a potential complex formation in solution, however it is not stable enough for an unambiguous detection by pulldown assays.

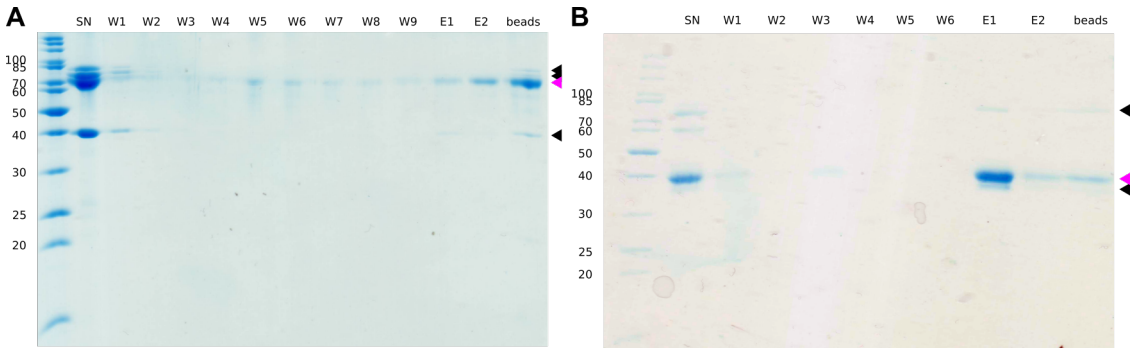

Figure 26) **Pulldown assays. A:** Pulldown assay using Protein A/G UltraLink™ Resin, NgR1-Fc and $\mu1_3\sigma3_3$. **B:** Pulldown assay using Ni-NTA Agarose, NgR1-His and $\mu1_3\sigma3_3$. $\mu1_3\sigma3_3$ is indicated by black arrowheads, NgR1 with magenta arrowheads. SN = supernatant after incubation with resin; WX = washing step X; EX = elution step X; beads = Protein A/G UltraLink™ Resin or Ni-NTA Agarose after elution.

6.1.3.3 Crosslinking Assays

To increase the stability of a potential $\mu1_3\sigma3_3$-NgR1 complex, crosslinking experiments were performed. DMP, DMS, and glutaraldehyde were used to couple primary amines, e.g. from lysines or the N'-terminus, and EDC + NHS to couple primary carboxyls, e.g. from aspartates, glutamates, or the C'-terminus, to primary amines. All crosslinkers were evaluated for both His-tagged and Fc-tagged NgR1 in complex with $\mu1_3\sigma3_3$ (see Figure 27).

DMP and DMS did not show any crosslinking effect, neither for the complex samples nor for the individual proteins. Only bands for non-crosslinked μ1 at 70 kDa and 76 kDa, σ3 at 38 kDa, NgR1-Fc at 70 kDa, and NgR1-His at 38 kDa were observed by SDS-PAGE analysis.

Glutaraldehyde crosslinks $\mu1_3\sigma3_3$ capsomers intermolecularly and creates several additional bands at approximately 140 kDa, and at higher molecular weight around 260 kDa. There is a faint band for NgR1-His at 70 kDa, but there are no clear additional

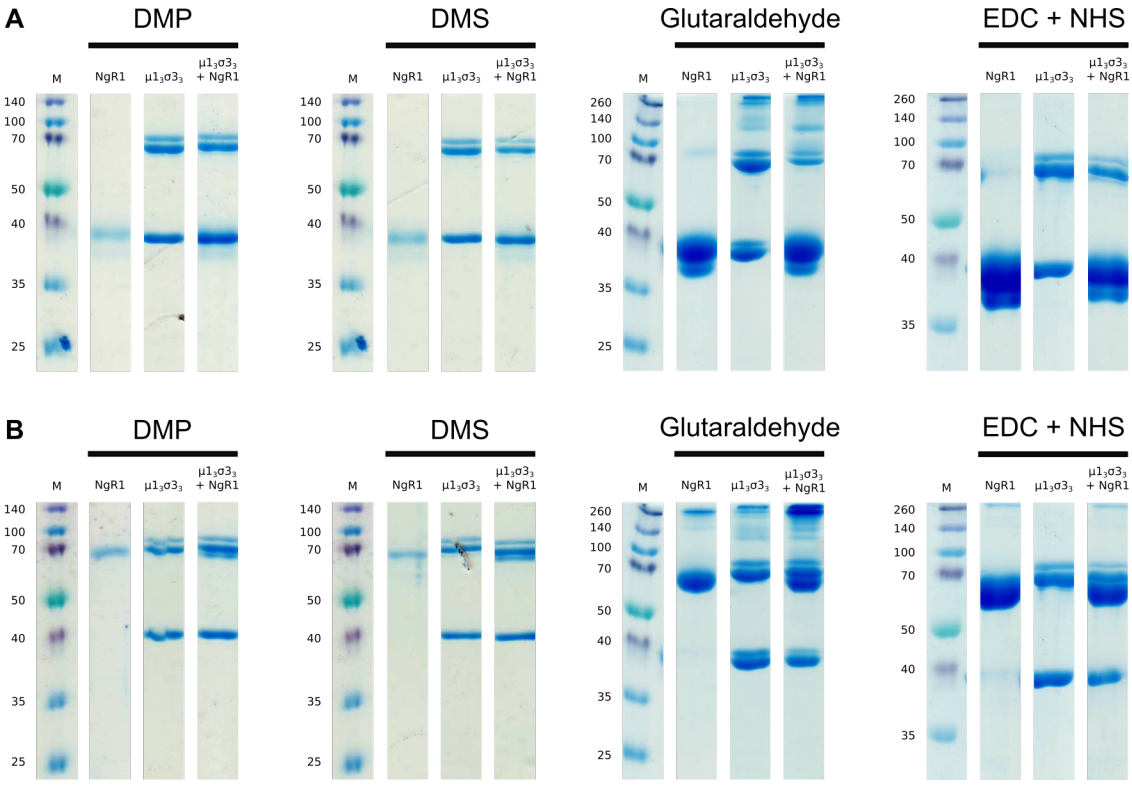

Figure 27) **Crosslinking assays. A:** Crosslinking assays with His-tagged NgR1, $\mu1_3\sigma3_3$ and the crosslinking agents DMP, DMS, glutaraldehyde, and EDC + NHS. **B:** Crosslinking assays with Fc-tagged NgR1, $\mu1_3\sigma3_3$ and the crosslinking agents DMP, DMS, glutaraldehyde, and EDC + NHS.

bands at the $\mu1_3\sigma3_3$-NgR1-His complex sample, although the $\mu1_3\sigma3_3$ bands appear less intense compared to the individual $\mu1_3\sigma3_3$ sample. Individual NgR1-Fc was also crosslinked intermolecularly by glutaraldehyde, resulting in additional bands at 260 kDa, but again no clear additional signal was observed at the $\mu1_3\sigma3_3$-NgR1-Fc complex sample.

Crosslinking using EDC + NHS had no effect on NgR1-His and $\mu1_3\sigma3_3$, but results in a high molecular weight species at NgR1-Fc (>260 kDa). No additional species was detected in the complex samples. None of the crosslinking agents was suitable to generate clear evidence for a $\mu1_3\sigma3_3$-NgR1 complex in solution.

6.1.3.4 Surface Plasmon Resonance Spectroscopy

Since a stable complex could not be evidenced by gel filtration, pulldown, or crosslinking assays, SPR analysis was performed to investigate potential binding in the low micromolar range of $\mu1_3\sigma3_3$ to NgR1. Initially, a NTA Sensor Chip was used to couple His-tagged NgR1 and analyze the affinity to $\mu1_3\sigma3_3$, but the NTA Sensor chip showed unspecific binding of $\mu1_3\sigma3_3$ in a concentration dependent manner, without previous NgR1 coupling (see Figure S8). Therefore, the NTA Sensor Chip was not suitable for affinity measurements.

Alternatively, a Protein A Sensor Chip was tested and did not show any unspecific binding, which could potentially disturb the experiment. Hence, 15 nM NgR1-Fc were immobilized on the chip surface and a range of 1–5,200 nM $\mu1_3\sigma3_3$ was evaluated for

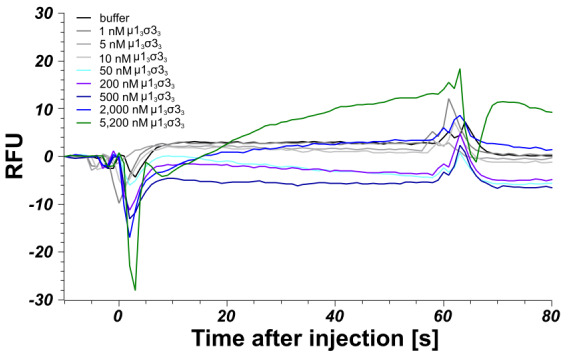

Figure 28) **SPR analysis. A:** SPR analysis using a Protein A Sensor Chip testing a concentration range of 1–5,200 nM with NgR1-Fc immobilized on the surface. Only at 2,000 nM and 5,200 nM a small binding signal was detectable.

binding (see Figure 28). All samples up to 500 nM $\mu1_3\sigma3_3$ did not show any signal increase referring to an interaction with NgR1, only for 2,000 nM and 5,200 nM $\mu1_3\sigma3_3$ a slight increase in relative fluorescence units (RFU) was detected. In summary, high micromolar concentrations of $\mu1_3\sigma3_3$ are required to reveal any binding by SPR analysis. Hence, the binding affinity is not sufficient to form a stable complex of NgR1 and $\mu1_3\sigma3_3$ in solution, not to mention subsequent crystallization for structural studies of the interaction.

6.1.4 CryoEM Analysis of ReoV T3D Virion in Complex with NgR1

Various attempts of $\mu1_3\sigma3_3$-NgR1 complex formation were not successful and as a consequence, crystallographic analysis of the interaction was not feasible. Possibly, one $\mu1_3\sigma3_3$ capsomer is not sufficient for NgR1 binding, as the virion assembly might alter the individual capsomer conformation on the viral surface due to intermolecular interactions. To provide the best possible and biological environment, complete T3SA- virions were examined for NgR1 binding by cryoEM analysis.

T3SA- virions were mixed with either PBS or 8 mg mL^{-1} NgR1-His in a ratio of 1:4 (V/V), and incubated at 4 °C for 4 h prior to vitrification. Data were collected on a JOEL 3200 FSC cryo-electron microscope equipped with a direct detector K2 summit camera, using low-electron dose conditions. Movie stacks containing 50 subframes each were collected using SerialEM at 20,000x magnification, corresponding to a pixel size of 1.71 Å (sample preparation, vitrification, and data collection described until here was performed by Dr. Liya Hu and Dr. Xinzhe Yu).

6.1.4.1 CryoEM Data Processing

Beam-induced motion correction of the movie stacks was performed with the *align-frames* script of the IMOD software package [232]. The micrographs of unliganded virions appear sharper and the borders are clearer distinguishable from the background, while the micrographs with an excess of NgR1 exhibit more background noise (see Figure 29 A+B). The complexed virus particles tend to be more cohesive and clumpy, while the unliganded reovirions are mostly singular. Particles were initially picked by a convolutional neural network using *e2boxer.py* [235]. In order to train this network, clearly identifiable particles were selected as good references, as well as empty areas for background recognition and contaminated particles for eliminating bad particles. After

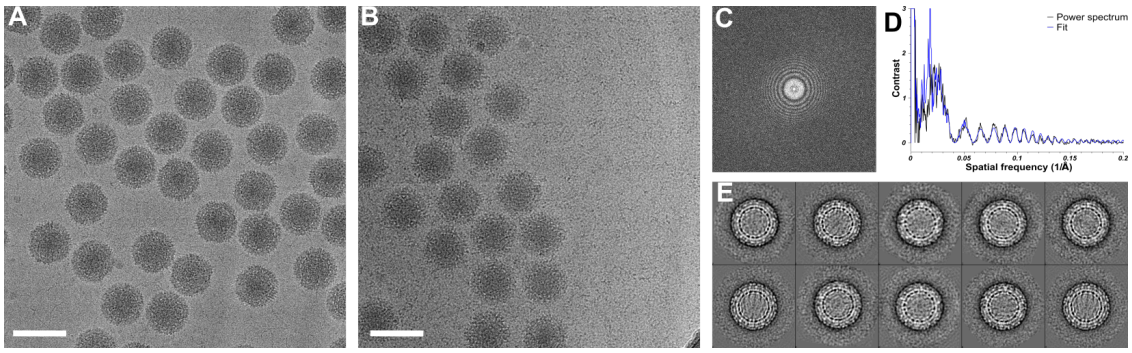

Figure 29) **CryoEM data processing. A+B:** Micrographs of reovirus virions (A) or reovirus virions complexed with NgR1 (B). The scalebar represents 100 nm. **C:** Representative 2D power spectrum averaged for particles of one micrograph. **D:** Background subtracted, rotationally averaged power spectrum (black line) and contrast transfer function (CTF) fit with adjusted defocus and B-factor (blue line). **E:** 2D class averages selected for generating an initial 3D model for subsequent 3D reconstruction.

neural network particle picking, all micrographs were additionally inspected manually to remove non-eliminated contaminations or particles that appeared clumpy and non-singular.

CTF correction was performed using *e2ctf.py*. In this process, an average power spectrum of all particles in one micrograph is calculated (see Figure 29 C). A background-subtracted, rotationally-averaged power spectrum is plotted against the spatial frequency, and the defocus and B-factor parameter of the theoretical contrast transfer function are adjusted to maximize the fit to the real power spectrum (see Figure 29 D).

Reference-free 2D class averages were calculated using *e2refine2d.py*. Classes showing clear reoviral features such as two shells, for the core and the outer capsid (see Figure 29 E), were selected to generate an initial 3D model using *e2refine2d.py*. For this, and throughout all further refinement steps, icosahedral symmetry was applied. Particles were low-pass filtered to 12 Å to reduce the processing time for the first refinement runs. The reconstruction was iteratively refined using low-pass 5 Å and eventually full-resolution images. After having a sufficiently good reconstruction that allowed unambiguous identification of σ3 or NgR1 features, the particle quality was evaluated according to the information content per resolution, and low-quality particles were discarded to further improve the refinement. Final reconstructions of the unliganded reovirus virion to 7.2 Å and of the NgR1-liganded virion to 8.9 Å were obtained (see Figure 30 and 31 A+B).

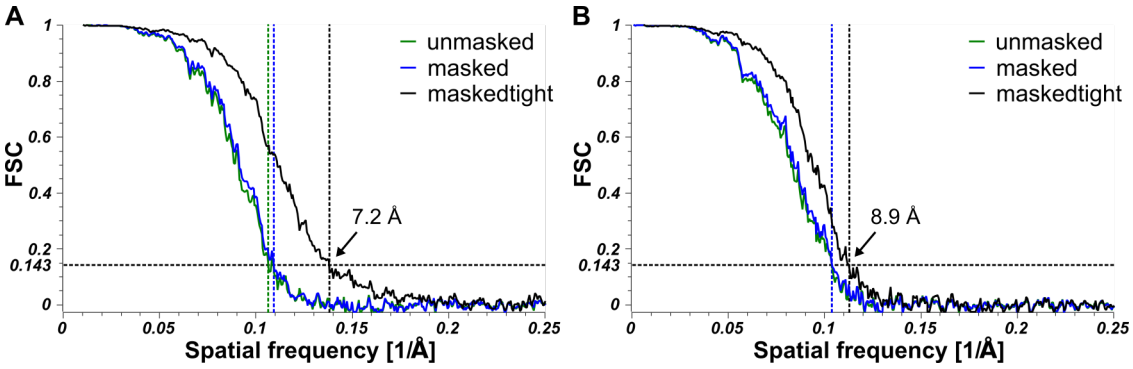

Figure 30) **FSC of unliganded and NgR1-liganded reovirus reconstructions. A+B:** The FSC estimates the average resolution of the final reconstruction without masking (green), masked (blue) and tight-masked (black) for the unliganded (A) and NgR1-liganded (B) ReoV reconstruction.

6.1.4.2 Molecular Docking in Asymmetric Unit

The 3D reconstruction of the reovirus virion clearly displays icosahedral five-, three-, and two-fold rotational symmetry axes (see Figure 31 A left). Therefore, the asymmetric unit (ASU) covers $\frac{1}{60}$ of the whole capsid. The capsid surface displays unambiguous features for μ1 (green) and σ3 (blue), spanning most of the virion, as well as for the outer capsid protein λ2 (yellow) at the vertices. At the center of the λ2 pentamer, the N'-terminus of the σ1 shaft is recognizable.

The reconstruction of the NgR1-liganded virion (Figure 31 A right) displays additional banana-like features on the surface of the virion, matching the shape of NgR1. This features are symmetrically arranged according to the icosahedral symmetry operators and located on top of the viral surface, thus slightly more distant from the core (> 430 Å, colored magenta) than σ3 (< 430 Å, colored blue).

The atomic coordinates of the core proteins λ1, σ2, and of the outer capsid proteins λ2, μ1 and σ3 were unambiguously fitted into the asymmetric unit of the virion reconstruction (see Figure 31 B+C). The asymmetric unit consists of one copy of each λ1, σ2, and λ2, three complete copies of $\mu1_3\sigma3_3$ hexamers, and one third of a copy of another $\mu1_3\sigma3_3$ hexamer, which is directly located on the icosahedral three-fold axis (see Figure 31 C). The asymmetric unit of the NgR1-liganded reconstruction allowed additional fitting of five NgR1 protomers (see Figure 31 D). Four of those five NgR1s are sitting in between two σ3 protomers, solely the NgR1 close to the five-fold axis contacts only a single σ3. Interestingly, the C'-termini of the sandwiched NgR1s, where the His-tag is attached, are clustering at the small pore formed by six σ3 protomers of six different $\mu1_3\sigma3_3$s.

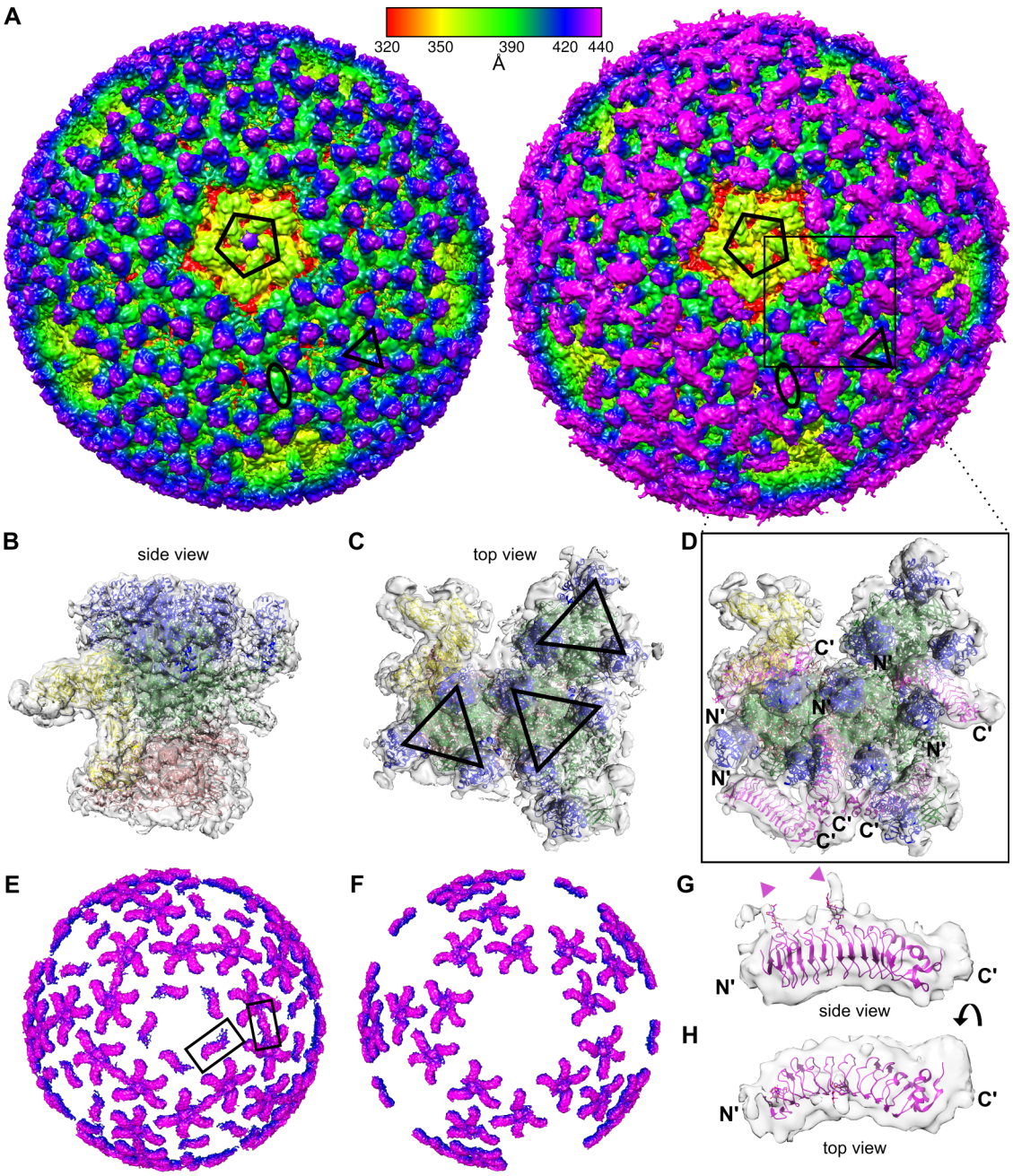

Figure 31) **CryoEM reconstruction of unliganded and NgR1-liganded reovirus virions. A:** Reconstructions of unliganded (left) and NgR1-liganded (right) virion are colored according to distance from the core. Icosahedral five-, three-, and two-fold symmetry axes are indicated by black symbols. **B–D:** Map excerpts covering the asymmetric unit of the reovirus virion from side (B) and top view (C) and NgR1-liganded virion from top view (D) with the atomic coordinates of λ1, σ2 (both red), λ2 (yellow), μ1 (green), σ3 (blue), and NgR1 (magenta) fitted into the map. Three complete $\mu1_3\sigma3_3$ heterohexamers are indicted by black triangles. N'- and C'-termini of NgR1 are labeled. **E+F:** Difference density map of both reconstructions at a counter level level of 1.55 (E) or 2.0 (F). Additional features are highlighted by black boxes. **G+H:** Fit of NgR1 coordinates into the difference density map at a counter level of 1.15 from side (G) and top view (H). N'- and C'-termini are labeled and glycosylation sites are indicated by magenta arrowheads.

6.1.4.3 NgR1 Features in Difference Density Map

To validate the presence of additional features such as NgR1 in the 3D reconstruction, a difference density map of the unliganded ReoV reconstruction subtracted from the NgR1-liganded ReoV reconstruction was calculated. Apart from minor unspecific blobs in the core region, the difference map shows clear density for all proposed NgR1 binding sites (see Figure 31 E). Furthermore, an additional feature directly at the two-fold axis is observed, however the shape does not fit to a single NgR1 molecule, but rather an averaged density of two NgR1 molecules of opposite orientations. Interestingly, upon increasing the counter level for displaying the map, the NgR1 features at the two-fold axis and close to the five-fold axis disappear, suggesting a weaker signal intensity (see Figure 31 F).

Fitting of NgR1 into the difference density map confirmed its proposed orientation (see Figure 31 G+H). Upon slightly decreasing the counter level (1.15), additional density features appeare that perfectly fit to sugar trees at the two glycosylation sites N82 and N179. However, the fit percentage of UCSF Chimera is only slightly better (92–95%) for the above mentioned conformation compared to N'- and C'-termini reversed (88–91%).

6.1.4.4 NgR1 Arrangement on ReoV Capsid

Noticeably, all NgR1 protomers are not located centrally on top of a single $\mu1_3\sigma3_3$ heterohexamer, but either in between two neighboring ones (NgR1 protomers 1–4, see Figure 32 A) or at the side of one (NgR1 protomer 5). The overall binding mode between NgR1 and σ3 is very similar within the NgR1 protomers of the asymmetric unit (see Figure 32 D). In case of NgR1 protomer 1, the neighboring asymmetric unit provides the second σ3 for sandwiching NgR1. Although NgR1 protomer 5 is only contacted by one σ3, there is no difference in the mode of binding compared to the remaining NgR1s. Superimposition of all five σ3-NgR1-σ3 assemblies and subsequent RMSD calculation using *rms_cur* in PyMol revealed an average RMSD of 1.1 Å of all NgR1s, and 2.5 Å or 2.7 Å for σ3 at the concave or convex interfaces, respectively. These values far below the resolution of the reconstruction.

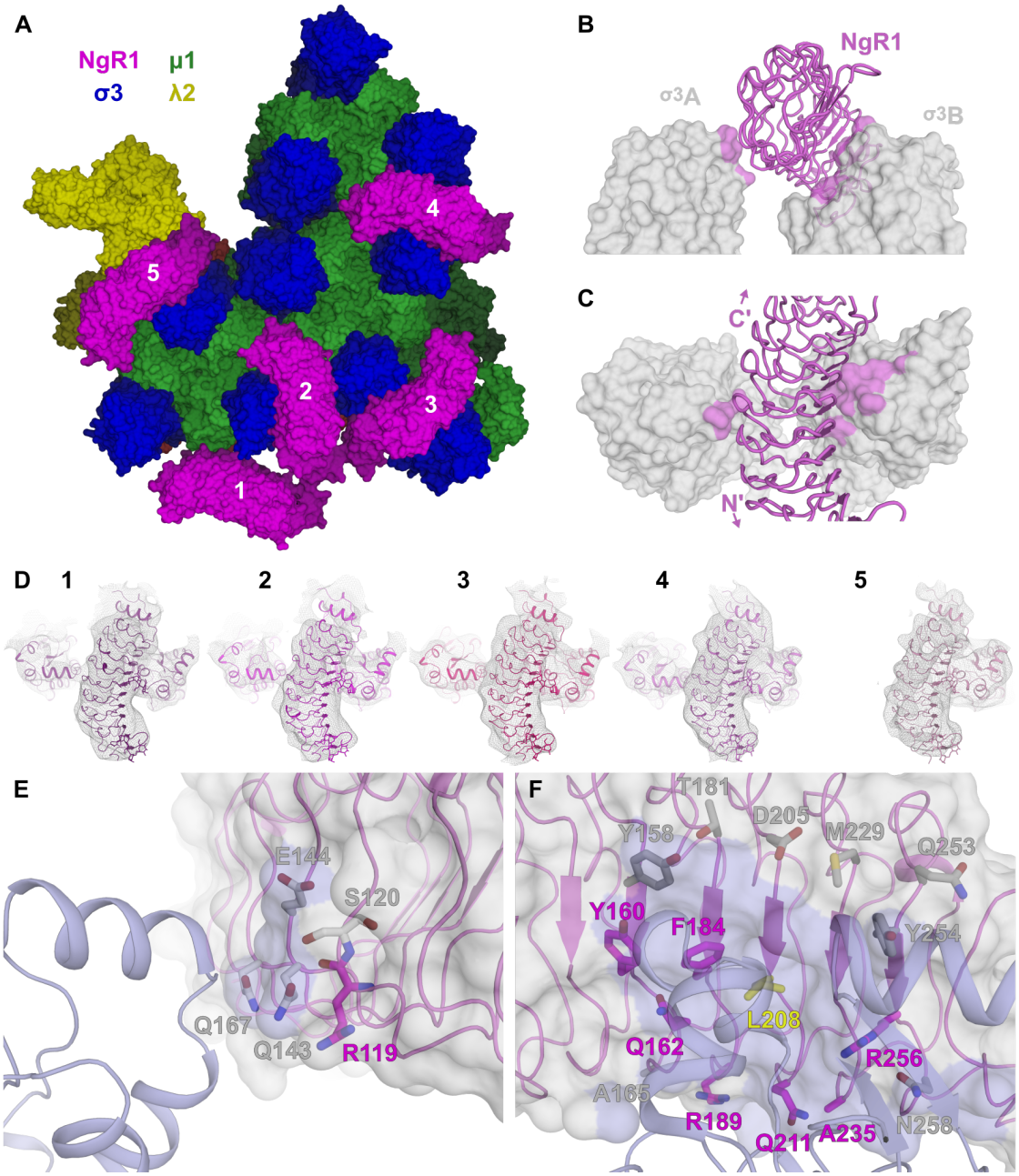

Figure 32) **NgR1 binding mode and interaction with σ3. A:** Surface representation of λ2 (yellow), μ1 (green), σ3 (blue), and NgR1 (magenta, labeled from 1–5) proteins covering the asymmetric unit. **B+C:** NgR1 (magenta) bridges two σ3 protomers from different $\mu1_3\sigma3_3$ heterohexamers (white, A and B) from side view (B) and top view (C). The surface of σ3 within 5 Å of NgR1 is colored in magenta. N'- and C'-termini are labeled. **D:** Binding mode comparison of all five NgR1s and respective σ3s. The corresponding 3D reconstruction is displayed at a counter level of 1.0 as white meshes. NgR1 protomer 1 is flanked by one σ3 from the neighboring asymmetric unit. NgR1 protomer 5 is located at the five-fold axis and is lacking the second σ3. **E+F:** Small, convex interface (E) and large, concave interface (F) of NgR1 and σ3. NgR1 residues are colored magenta (crucial for infection) or grey (not crucial for infection), the central L208 in yellow.

6.1.4.5 Binding Interfaces of NgR1 and σ3

A closer view on the binding interface reveals, that NgR1 is lying flat on the capsid surface in a trench between the two σ3 molecules, but without any contact to μ1 (see Figure 32 B). The convex interface (left side from top view, see Figure 32 C) is much smaller and mainly close to LRR domains 4 and 5. At a distance within 5 Å of σ3, there are either charged (E144) or polar (Q143, Q167) amino acids (see Figure 32 E) for potential interactions with NgR1. The concave interface (right side from top view, see Figure 32 C) is much larger and extends over LRR domains 5–8. The center of this interface is a cavity, formed by the small L208, that is surrounded by many large, either positively charged or aromatic amino acids (magenta residues, see Figure 32 F). Surface charge analysis revealed a highly positive electrostatic potential at this binding interface, while NgR1 has a highly negative electrostatic potential at the opposite area. Overall, this interface provides numerous possibilities for interacting with σ3.

6.2 Discussion

6.2.1 Protein Purification and Analysis

The original aim of this project was to crystallize a complex of NgR1 and $\mu1_3\sigma3_3$ for structural studies. The purification of recombinant NgR1-His was straightforward and yielded high amounts of protein. A deglycosylation assay excluded that the double band at SDS-PAGE analysis is due to glycosylation as proposed by Barton et al. [192]. Instead, a signal peptide cleavage site was detected, and since it is an autocleavage site, it explains why a certain fraction is cleaved while another is not. Furthermore, the cleaved fraction seems to increase over time, as the lower band became more intense compared to the higher-molecular weight band after 1 d at RT. For further analysis, a prolyl-endopeptidase experiment could be performed, which should enable complete cleavage of the signal peptide. Similar to His-tagged NgR1, Fc-tagged NgR1 is probably also partially cleaved, but due to the increased molecular weight of 60 kDa without glycosylation, a difference of 3 kDa is barely visible at SDS-PAGE analysis.

The yield in purifying $\mu1_3\sigma3_3$ could be significantly improved compared to previously published protocols by switching to HighFive insect cells [72]. One major difference is that the protein complex was secreted into the suspension medium, which might be

related either to the switch of cell line or to the prolonged expression time, where a large amount of cells was already lyzed to release new baculovirus particles. The addition of a small amount of FBS during expression has stabilized the recombinant protein by preventing degradation from insect cell proteases. Due to the lack of an affinity tag, $\mu1_3\sigma3_3$ was still largely contaminated after initial IEX, but throughout HIC and SEC the protein purity could be significantly improved to a sufficient quality for complexation assays.

6.2.2 Challenges at Protein-based Complex Formation

Various approaches have been used to study complex formation of $\mu1_3\sigma3_3$ and NgR1. To detect a shift in retention volume, gel filtration requires a quite stable complex in solution, therefore it is less sensitive. Varying conditions regarding protein ratio, affinity tag, temperature, incubation time, and the addition of calcium did not reveal any sign of complex formation that could have been confirmed by SDS-PAGE analysis, apart from aggregation. Also crosslinking has special requirements on proximity and accessibility of chemical groups that are suitable for the respective crosslinking agents. Apparently, these were not met, therefore there was no evidence for complex formation obtained.

Both pulldown assays and SPR analysis revealed very weak interaction of $\mu1_3\sigma3_3$ with NgR1, however SPR is much more sensitive and easier to interpret. In each case, the far smaller NgR1 was stationary immobilized to either affinity beads or a Sensor Chip, and thus less mobile, which might facilitate a slightly more stable interaction with the heterohexamer. However, binding of Fc-tagged NgR1 itself to the Protein A/G Ultralink™ Resin was not entirely stable, as it was continuously released during the washing steps. Nevertheless, there were clear $\mu1_3\sigma3_3$ bands visible during elution, although unspecific binding could not absolutely be excluded, despite the control assay, due to the low sensitivity of SDS-PAGE analysis. Silver staining is much more sensitive and could be applied for future assays to detect weaker bands at SDS-PAGE analysis.

SPR analysis is, in contrast to the previously discussed methods, not relying on a long-term stable complex, but can also detect a temporary interaction of two proteins. This makes negative controls absolutely necessary, as shown for His-tagged NgR1. During this SPR assay, unspecific binding of $\mu1_3\sigma3_3$ to the NTA Sensor Chip was observed. There is a large patch of several histidines on the surface of σ3, which could have caused this interaction. Therefore, the NTA Sensor Chip was not suitable for interaction studies.

The Protein A Sensor Chip instead did not exhibit any unspecific binding of $\mu1_3\sigma3_3$, but showed a weak signal for $\mu1_3\sigma3_3$ binding to NgR1. The binding event occurred however only at the micromolar concentration range of $\mu1_3\sigma3_3$, which indicates a low affinity. This is consistent with the previous results of the complexation assays and explains why less sensitive methods could not detect any interaction.

Overall, a stable complex could not be obtained with purified NgR1 and $\mu1_3\sigma3_3$ only. Presumably, the affinity between a single heterohexamer and NgR1 is only in the millimolar range, making a complex in solution not stable enough to be detected. Therefore, crystallization of this complex was not feasible. However, complete virions are capable of infecting cells using solely NgR1 as attachment receptor protein. Possibly the environment at the capsid surface is required for NgR1 binding. To provide this environment, reovirus virions with and without NgR1 were analyzed by cryoEM, which is advantageous for such large protein complexes compared to crystallography.

6.2.3 CryoEM Data Processing and Refinement

For single particle cryoEM analysis of a reovirus virion liganded with NgR1, the latter was added in excess to achieve complete binding, despite the low affinity observed for the soluble recombinant proteins. However, this also resulted in a increased background noise level of the micrographs due to unbound NgR1. This can hardly be removed on a micrograph level as NgR1 is too small to be identified individually. Via dialysis or gel filtration prior to sample vitrification, excessive NgR1 could be removed. But it is questionable whether NgR1 is bound tightly enough to stay at the virus surface in absence of soluble NgR1 in solution. In addition, the virus particles appeared to be more cohesive and clumpy compared to the unliganded reovirus particles, for which several reasons are conceivable. On the one hand, the high background level made a clear separation of individual particles by visual inspection more difficult, which could have contributed to the clumpy appearance. On the other hand, NgR1 could have tended to interact with each other at high concentrations, for example via their histidine tag. This could have induced a non-covalent crosslinking or mild aggregation of virus particles that have bound NgR1. Finally, ligand binding could also have triggered internal processing of the reovirus particle leading to conformational changes of $\sigma1$, as in the transition from virion to ISVP [71, 73], and subsequent particle association.

For this reason, far less NgR1-liganded virions were picked at the beginning of

the single particle analysis compared to the unliganded data, although many more micrographs were recorded. Also the particle quality, i.e. the theoretical maximum resolution of the individual micrographs, was on average significantly lower, probably also due to the higher background noise level. As a consequence, more particles were discarded in the course of the refinement, and the final resolution is lower (8.9 Å) compared to the ReoV virion solely (7.2 Å).

Although the number of particles is low for cryoEM standards, a reasonable resolution was obtained due to the icosahedral symmetry of the viral capsid, which could be applied for the 3D reconstruction. The asymmetric unit of the icosahedral capsid is only $\frac{1}{60}$ of the whole virion, therefore the information content of a single virus particle is much higher than for a regular protein. The final reconstructions allowed for unambiguous docking of the ReoV capsid proteins λ1, σ2, λ2, μ1, and σ3 into the asymmetric unit. The N'-terminus of the σ1 tail is visible at lower density thresholds, however the remaining larger part of σ1 could not be resolved. One reason therefore is the tight mask that was applied on the virus capsid during the reconstruction, which excludes the major part of σ1 in favor of significantly reduced background noise. Additionally, the application of icosahedral symmetry for the reconstruction is disadvantageous for the reconstruction of σ1 due to the five-fold-to-three-fold mismatch with the λ2 pentamer. In that case, local asymmetric reconstruction would be necessary to better resolve σ1 as shown by Pan et al. [76]. However, this is not explicitly relevant for the aim of this project and was therefore not performed.

6.2.4 Structural Analysis of the 3D Reconstructions

Overall, the 3D reconstruction agrees well with existing low [256], intermediate [257], and high resolution [258, 76] ReoV reconstructions. Due to the close contact of the $\mu1_3\sigma3_3$ heterohexamers at the capsid surface, a large σ3 surface pattern is formed, enabling several possibilities for NgR1 to interact with one or more σ3s. Interestingly, the surface is not completely closed, but three cavities are formed on every icosahedral face by six $\mu1_3\sigma3_3$ heterohexamers each, generating another different environment for potential NgR1 binding.

In each asymmetric unit, five NgR1 protomers were unambiguously docked into the 3D reconstruction. Additionally, there is a map feature directly at the two-fold symmetry axis that looks like an average of two NgR1 protomers in contrary orientation. At this

position, the capsid environment enables two possible, symmetry-related binding sites, each slightly shifted against the other. Due to steric hindrance, only one can be occupied at a time. Assuming a statistical 50 % occupancy for each, the application of icosahedral symmetry results in an average density feature of both binding possibilities, which does however not allow for modeling any of them. In summary, this results in 330 possible NgR1 binding sites on the virus surface.

RMSD analysis of the five modeled binding sites reveals a highly similar binding mode with respect to the resolution of the reconstruction. No obvious differences in positioning of either NgR1 or both neighboring σ3 molecules is observed, indicating a specific binding mechanism. The only difference is that NgR1 protomer 5, which is located close to the five-fold axis, is only interacting with one σ3 protomer. It is therefore less tightly attached to the virus capsid and shows a lower feature intensity compared to the embedded NgR1s. Maybe a slight steric influence of σ1 helps stabilizing the NgR1-binding at this position, although only one interaction partner is present. Also the unmodeled NgR1 feature at the two-fold axis shows a lower signal compared to the others, as explained above. But since this NgR1 is also complexed by two σ3 protomers, a similar affinity compared to the other four modeled NgR1s is expected. In general, the interaction with two different σ3 protomers might be stabilized additionally by a loose contact to a third σ3 the N-terminus of NgR1, which is not directly interacting with NgR1, but at least in close proximity. However, the resolution of the reconstruction was not sufficient to make a precise assessment on this third potential contact.

Overall, the binding mode indicates a low affinity of σ3 to NgR1. This explains, why all interaction assays with single proteins instead of a complete virus did show no (gel filtration, crosslinking assay) or only a very weak interaction (pulldown assay, SPR). In both, pulldown and SPR assays, one interaction partner is coupled to either beads or a Sensor Chip and thus less mobile, which could facilitate binding at low affinities and give at least some signal at these assays. In solution, both proteins were too mobile to stay in complex at such a low affinity.

6.2.5 Concave and Convex NgR1 Binding Interfaces

A look at the two binding interfaces shows that the convex interface is much smaller in comparison to the concave interface (156 $Å^2$ versus 821 $Å^2$ contact area with a distance of less than 3.9 Å between NgR1 and σ3, calculated with PyMol). There are a few

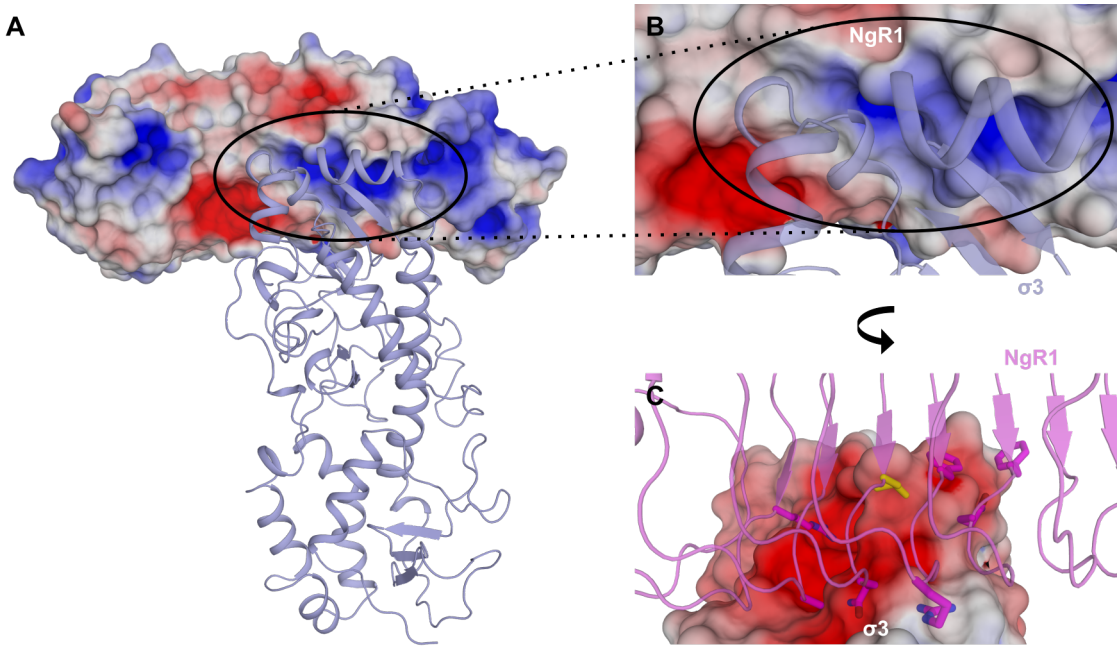

Figure 33) Surface charge analysis of concave interface. A: Concave binding interface of σ3 (blue cartoon) and NgR1 (surface colored according to electrostatic potential) **B:** Close-up View of (A). **C:** Close-up view on σ3 (surface colored according to electrostatic potential) and NgR1 (magenta cartoon). Electrostatic surface potential colored from −6 kT (red) to 6 kT (blue).

charged or polar residues at the convex interface, which could serve as an interaction partner. However, due to its small size it may well be that this interface only helps to facilitate and direct the docking of NgR1 or stabilize NgR1 in the binding groove. On the other hand, the concave interface is quite large with an overall positive surface charge of NgR1 and a significant negative charge of σ3 (see Figure 33). Both, the resolution and the size of the interaction area do not allow for identifying individual amino acids that contribute to binding. However, the small and hydrophobic L208 is remarkably sticking out (by not sticking out) in between a broad patch of large, either aromatic or charged amino acids. It rather forms a small cavity in between the bulky residues, which could serve as anchoring point for NgR1 docking onto σ3. Mutating L208 to an arginine resulted in an almost complete loss of infectivity, while NgR1 was still detectable by antibodies on the cell surface, hence the folding is not significantly affected by the mutation [Dr. Danica Sutherland, personal communication].

To further characterize the interaction interface and identify potentially essential amino acids, a mutagenesis study was performed (by Dr. Danica Sutherland and Olivia Welsh). Two panels of amino acids, either in close proximity (< 5 Å) or slightly further distant (5–7.5 Å) from the proximate σ3 protomer were assigned, with L208 being the

center of the concave interface. Reversed-charge mutants showed a complete loss of infectivity, despite cell surface expression, for seven additional amino acids that are either directly adjacent or in close proximity to L208: Y160, Q162, F184, R189, Q211, A235, and R256 (see Figure 34). All other mutants at this interface, which showed little to no effect on infectivity, are more distant from L208 and at the border of the concave

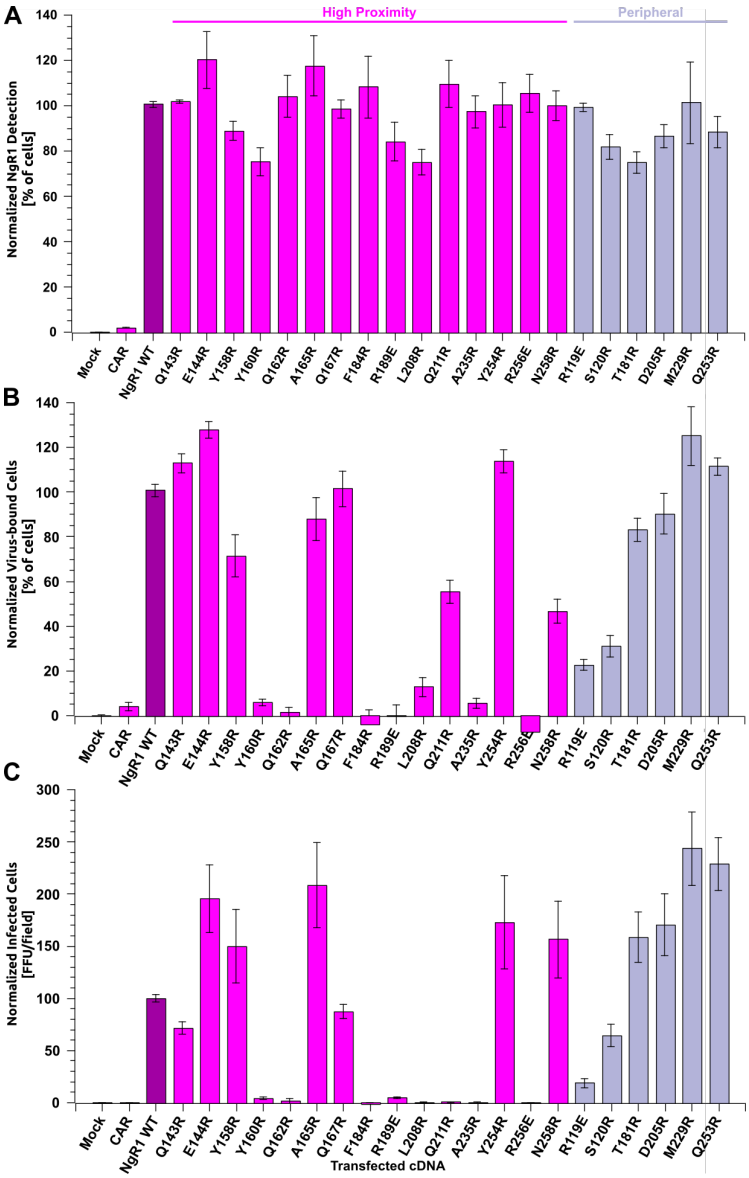

Figure 34) **NgR1 mutagenesis studies. A:** Surface expression, **B:** ReoV binding, or **C:** ReoV infectivity of mock- or NgR1-transfected CHO cells. The NgR1 mutants are grouped by close proximity (< 5 Å from σ3, magenta) or peripheral (5–7.5 Å from σ3, light blue). CAR was used as negative control. Error bars indicate SEM. Data provided by Dr. Danica Sutherland.

interface proposed by the cryoEM reconstruction. Diverse amino acid types are present in this panel of crucial residues: Positively charged arginines, polar glutamines and also an aromatic and a hydrophobic amino acid each. The interaction seems not solely dependent on a specifically charged or polarized site. The large number and diversity of amino acids indicates that the overall conformation and arrangement is more important than single interactions.

Interestingly, from all mutants at the convex interface, only R119, which is located in the periphery of this interface, resulted in a loss of infectivity, while all other amino acid mutations did not influence the infectivity. This effect could be caused by the reversed charge of the glutamic acid compared to arginine, that affects the neighboring residues of the convex interface. Alternatively, it is plausible that the actual interface is slightly shifted compared to the proposed interface due to the intermediate resolution of the reconstruction.

The C'-to-N'-terminal orientation of NgR1 is unambiguously visible in the final 3D reconstruction and it is also reasonable in a biological context. The glycosylation sites, which were also displayed in the existing crystal structures, are pointing away from the virus capsid and are hence not contributing to viral binding. At the opposing orientation, the carbohydrates would point into the viral capsid, clashing with σ3. Hence, binding of NgR1 would not be feasible in first place. This is also in line with mutagenesis studies of the NgR1 glycosylation sites N82 and N179, which showed that the post-translational modification is dispensable for viral binding and infection [Danica Sutherland, personal communication]. Therefore, any induced fit mechanism or interaction of the glycans with the viral capsid are unlikely.

Interestingly, this orientation leads to an accumulation of the C-terminal histidine tags of the recombinant protein at cavities formed by six $\mu1_3\sigma3_3$ heterohexamers. As there is an unmodeled density feature at this position, this could be explained by several interacting histidine tags. In a biological context, full-length NgR1 has a long, unfolded region of more than 100 amino acids at the C'-terminus, which acts as a linker to the GPI-anchor. The length of the linker is probably very important to enable NgR1 binding. Since σ1 is protruding from the viral surface, σ3 is not able to directly reach the host cell surface. The linker bridges this distance and allows for the unusual binding mode of NgR1, which is lying flat on the viral surface. This increase of interaction surface counteracts the low overall affinity. Furthermore, NgR1 molecules tend to accumulate to two or more in lipid raft regions at the cell surface [259, 260, 261]. The proposed

binding mode would allow a whole patch of NgR1s to simultaneously bind to the viral surface. Despite the low affinity of a single NgR1, the multivalent binding interactions of a patch of NgR1s would increase the binding strength significantly. It is however unlikely that NgR1 protomer 5 is contributing considerably to the attachment, as it would, in addition to the lower affinity, also block binding of the integrin to λ2, which is required for subsequent cell entry. Overall, the structural data suggest that NgR1 mediated cell attachment is rather facilitated by high-avidity binding of numerous NgR1s instead of high-affinity binding.

In summary, the first structural data on reovirus attachment via the outer capsid protein σ3 are presented here. NgR1 is binding in a cleft of two σ3 protomers on the viral surface. This binding site is highly redundant on the capsid and enables multivalent binding of several NgR1s at the same time. This overcomes the presumably low affinity of this interaction, which is indicated by unsuccessful complexation trials using recombinant, soluble proteins. CryoEM analysis at intermediate resolution allowed narrowing down the potential interaction area, and mutagenesis studies confirmed several important NgR1 residues involved in binding. These data shed more light on reoviral host cell attachment on a structural basis. This study expands the knowledge on the reovirus receptor portfolio, it helps to better elucidate the viral path through the human body during an infection and can contribute to the development of reoviral vectors for medical applications.

7. Conclusion

All three projects have made significant findings, either at a very early stage of virological research by identifying basic attachment mechanisms, or at a rather advanced stage by optimizing viral inhibition strategies.

Starting from established antiviral inhibitors against HAdV37, binding of a new generation of compounds to serotype HAdV26 was shown by X-ray crystallographic analysis. A structure-guided approach further enabled adaption to a third serotype, HAdV36. This highlights the importance of characterizing pathogen-host interactions by structural biology approaches and shows the potential benefits. Exploiting structural data of one type of attachment site is a valid starting point for designing antiviral drugs. Visualization at atomic level allows for specific adjustments to the respective target, which may not be limited to HAdVs, but any other virus or pathogen with a symmetric receptor binding site. This strategy enables the design, development, and validation of high-affinity inhibitory compounds.

Furthermore, the old concept of a singular type of receptor or attachment site per virus is invalidated. HAdV56 was shown to bind CD46 not via established interaction sites for other HAdV serotypes, but through a novel binding site at an even different capsid protein that has not been shown to be involved in viral attachment so far. This raises the question, whether the attachment mechanism via the hexon has developed recently in new HAdV strains or whether it is the primordial, but so far undiscovered mechanism, from which binding sites at the much more exposed FK have evolved? Also the conserved sialic acid binding site does not seem to be required for HAdV56 infectivity. Is this site a recombination artifact from the ancestor virus or can it still be used as a backup escape mechanism, similar to HAdV26, in case CD46-binding is not possible?

Similarly, a JAM-A and sialic acid-independent cell attachment pathway for ReoVs has been structurally characterized in this thesis. It also involves a different capsid protein, namely σ3, and a unique binding mode of NgR1 embedded in between two σ3 interaction sites. It is of particular interest to find out how this attachment mechanism has evolved, whether the different ReoV types also exhibit different binding affinities

for NgR1 and how this ability to attach to neuronal cells affects the preferred infection routes.

It seems unusual that a numerously presented, but hardly accessible capsomer is involved in such a initial step of viral proliferation. A reasonable conclusion would be, that attachment via the major capsid protein relies on multivalent, simultaneous binding of several host cell receptor molecules, probably with low affinity. In that case, the attachment receptor would naturally occur in clusters on the host cell surface or in a highly oligomerized fashion, comparable to integrin clustering for HAdVs prior cell entry. This way the virus could be directed either to a certain type of cells, that is presenting a sufficient amount of receptor molecules, or to a certain area of the cell surface. Future research will have to address this to gain a better understanding of the complex field of virology.

Both novel attachment strategies raise questions that could address many other viruses, too: why have viruses evolved to exploiting different entry routes? Was the primary attachment site not available anymore and viruses needed an alternative pathway to escape? It could also be caused by two precursor virus strains with differing attachment modes that have recombined to a superior type retaining both. Furthermore, it is interesting to find out when, and in which order, the recombination or mutation has happened. For HAdVs, recombination of the major capsid proteins is an established source of novel serotypes. Therefore, it is not unlikely that a novel type combines potential attachment pathways of the two precursor HAdVs. But for ReoV only a small number of serotypes is known that do not recombine frequently. Either a cross-species recombination has occurred or the precursor is not existing anymore. Further research will be necessary to tackle these questions.

Overall, the results of this thesis have generated further evidence for the similarity of *adenoviruses* and *reoviruses*. Both are the first viruses reported to make use of a second capsid protein for an independent cell attachment and entry mechanism. In combination with the novel findings on structure-guided inhibitor design, this thesis provides a valuable addition to the still emerging field of viral and, even more important, antiviral research.

Bibliography

[1] D. Iwanowski (1903). *Über die Mosaikkrankheit der Tabakspflanze*, volume 13. E. Ulmer

[2] M. W. Beijerinck (1898). *Ueber ein contagium vivum fluidum als Ursache der Fleckenkrankheit der Tabaksblatter*. Verhandelingen der Koninklijke akademie van Wetenschappen te Amsterdam, pp. 3–21

[3] W. Reed, J. Carroll, and A. Agramonte (1901). *The etiology of yellow fever: An additional note*. Journal of the American Medical Association, XXXVI(7):431–440. ISSN 23768118. doi: 10.1001/jama.1901.52470070017001f

[4] T. P. Monath and P. F. Vasconcelos (2015). *Yellow fever*. Journal of Clinical Virology, 64:160–173. ISSN 18735967. doi:10.1016/j.jcv.2014.08.030

[5] F. D´Herelle (2007). *On an invisible microbe antagonistic toward dysenteric bacilli: brief note by Mr. F. D'Herelle(translated from the original of 1917)*. Research in Microbiology, 158(7):553–554. ISSN 0923-2508. doi:10.1016/J.RESMIC.2007.07.005

[6] W. M. Stanley (1935). *Isolation of a crystalline protein possessing the properties of tobacco-mosaic virus*. Science, 81(2113):644–645. ISSN 00368075. doi:10.1126/science.81.2113.644

[7] M. Knoll and E. Ruska (1932). *Das Elektronenmikroskop*. Zeitschrift für Physik, 78:318–339

[8] G. A. Kausche, E. Pfankuch, and H. Ruska (1939). *Die Sichtbarmachung von pflanzlichem Virus im Übermikroskop*. Die Naturwissenschaften, 27(18):292–299. ISSN 0028-1042. doi:10.1007/BF01493353

[9] N. P. Johnson and J. Mueller (2002). *Updating the accounts: global mortality of the 1918-1920 "Spanish" influenza pandemic.* Bulletin of the history of medicine, 76(1):105–115. ISSN 00075140. doi:10.1353/bhm.2002.0022

[10] W. Smith, C. Andrewes, and P. Laidlaw (1933). *A Virus Obtained From Influenza Patients*. The Lancet, 222(5732):66–68. ISSN 01406736. doi:10.1016/S0140-6736(00)78541-2

[11] J. K. Taubenberger and D. M. Morens (2006). *1918 Influenza: the Mother of All Pandemics*. Emerging Infectious Diseases, 12(1):15–22. ISSN 1080-6040. doi:10.3201/eid1201.050979

[12] E. D. Kilbourne (2006). *Influenza Pandemics of the 20th Century*. Emerging Infectious Diseases, 12(1):9–14. ISSN 1080-6040. doi:10.3201/eid1201.051254

[13] M. Rozo and G. K. Gronvall (2015). *The reemergent 1977 H1N1 strain and the gain-of-function debate*. mBio, 6(4). ISSN 21507511. doi:10.1128/mBio.01013-15

[14] M. P. Girard, J. S. Tam, O. M. Assossou, and M. P. Kieny (2010). *The 2009 A (H1N1) influenza virus pandemic: A review*. Vaccine, 28(31):4895–4902. ISSN 0264410X. doi:10.1016/j.vaccine.2010.05.031

[15] World Health Organization (WHO) (2012). *Vaccines against influenza WHO position paper – November 2012.* Releve epidemiologique hebdomadaire, 87(47):461–76. ISSN 0049-8114

[16] S. G. Deeks, J. Overbaugh, A. Phillips, and S. Buchbinder (2015). *HIV infection*. Nature Reviews Disease Primers, 1(1):1–22. ISSN 2056676X. doi:10.1038/nrdp.2015.35

[17] M. Worobey, M. Gemmel, D. E. Teuwen, T. Haselkorn, K. Kunstman, M. Bunce, J. J. Muyembe, J. M. M. Kabongo, R. M. Kalengayi, E. Van Marck, et al. (2008). *Direct evidence of extensive diversity of HIV-1 in Kinshasa by 1960*. Nature, 455(7213):661–664. ISSN 14764687. doi: 10.1038/nature07390

[18] Centers for Disease Control (CDC) (1981). *Pneumocystis pneumonia–Los Angeles.* MMWR. Morbidity and mortality weekly report, 30(21):250–2. ISSN 0149-2195

[19] M. S. Gottlieb, R. Schroff, H. M. Schanker, J. D. Weisman, P. T. Fan, R. A. Wolf, and

A. Saxon (1981). *Pneumocystis carinii Pneumonia and Mucosal Candidiasis in Previously Healthy Homosexual Men*. New England Journal of Medicine, 305(24):1425–1431. ISSN 0028-4793. doi:10.1056/NEJM198112103052401

[20] J. D. Reeves and R. W. Doms (2002). *Human immunodeficiency virus type 2*. Journal of General Virology, 83(6):1253–1265. ISSN 0022-1317. doi:10.1099/0022-1317-83-6-1253

[21] F. Barré-Sinoussi, J. C. Chermann, F. Rey, M. T. Nugeyre, S. Chamaret, J. Gruest, C. Dauguet, C. Axler-Blin, F. Vézinet-Brun, C. Rouzioux, et al. (1983). *Isolation of a T-lymphotropic retrovirus from a patient at risk for acquired immune deficiency syndrome (AIDS)*. Science, 220(4599):868–871. ISSN 00368075. doi:10.1126/science.6189183

[22] M. Popovic, M. Sarngadharan, E. Read, and R. Gallo (1984). *Detection, isolation, and continuous production of cytopathic retroviruses (HTLV-III) from patients with AIDS and pre-AIDS*. Science, 224(4648):497–500. ISSN 0036-8075. doi:10.1126/science.6200935

[23] S. Broder (2010). *The development of antiretroviral therapy and its impact on the HIV-1/AIDS pandemic*. Antiviral Research, 85(1):1–18. ISSN 01663542. doi:10.1016/j.antiviral.2009.10.002

[24] E. De Wit, N. Van Doremalen, D. Falzarano, and V. J. Munster (2016). *SARS and MERS: Recent insights into emerging coronaviruses*. Nature Reviews Microbiology, 14(8):523–534. ISSN 17401534. doi:10.1038/nrmicro.2016.81

[25] S. T. Jacob, I. Crozier, W. A. Fischer, A. Hewlett, C. S. Kraft, M. A. d. L. Vega, M. J. Soka, V. Wahl, A. Griffiths, L. Bollinger, et al. (2020). *Ebola virus disease*. Nature Reviews Disease Primers, 6(1):1–31. ISSN 2056676X. doi:10.1038/s41572-020-0147-3

[26] *WHO — Ebola virus disease – Democratic Republic of the Congo*. `https://web.archive.org/web/20210311194443/https://www.who.int/csr/don/26-June-2020-ebola-drc/en/` (Accessed: 2021-09-02)

[27] V. Sikka, V. Chattu, R. Popli, S. Galwankar, D. Kelkar, S. Sawicki, S. Stawicki, and T. Papadimos (2016). *The emergence of zika virus as a global health security threat: A review and a consensus statement of the INDUSEM Joint working Group (JWG)*. Journal of Global Infectious Diseases, 8(1):3. ISSN 0974-777X. doi:10.4103/0974-777X.176140

[28] T. C. Pierson and M. S. Diamond (2018). *The emergence of Zika virus and its new clinical syndromes*. Nature, 560(7720):573–581. ISSN 14764687. doi:10.1038/s41586-018-0446-y

[29] B. Afrough, S. Dowall, and R. Hewson (2019). *Emerging viruses and current strategies for vaccine intervention*. doi:10.1111/cei.13295. `/pmc/articles/PMC6468171//pmc/articles/PMC6468171/?report=abstracthttps://www.ncbi.nlm.nih.gov/pmc/articles/PMC6468171/`

[30] D. Baxby (1999). *Edward Jenner's inquiry; a bicentenary analysis*. Vaccine, 17(4):301–307. ISSN 0264410X. doi:10.1016/S0264-410X(98)00207-2

[31] A. Tarantola (2017). *Four thousand years of concepts relating to rabies in animals and humans, its prevention and its cure*. Tropical Medicine and Infectious Disease, 2(2). ISSN 24146366. doi:10.3390/tropicalmed2020005

[32] T. H. Weller, F. C. Robbins, and J. F. Enders (1949). *Cultivation of Poliomyelitis Virus in Cultures of Human Foreskin and Embryonic Tissues*. Proceedings of the Society for Experimental Biology and Medicine, 72(1):153–155. ISSN 15353699. doi:10.3181/00379727-72-17359

[33] H. Koprowski (1960). *Historical Aspects of the Development of Live Virus Vaccines in Poliomyelitis*. American Journal of Diseases of Children, 100(3):428–439. ISSN 15383628. doi:10.1001/archpedi.1960.04020040430018

[34] J. E. Salk, P. L. Bazeley, B. L. Bennett, U. Krech, L. J. Lewis, E. N. Ward, and J. S. Youngner (1954). *II. A Practical Means for Inducing and Maintaining Antibody Formation*. American Journal of Public Health and the Nations Health, 44(8):994–1009. ISSN 0002-9572. doi:10.2105/ajph.44.8.994

[35] D. R. Smith and P. A. Leggat (2005). *Pioneering figures in medicine: Albert Bruce Sabin- inventor of the oral polio vaccine*. Kurume Medical Journal, 52(3):111–116. ISSN 00235679. doi:10.2739/

kurumemedj.52.111

[36] A. B. Sabin, M. Ramos Alvarez, J. Alvarez Amezquita, W. Pelon, R. H. Michaels, I. Spigland, M. A. Koch, J. M. Barnes, and J. S. Rhim (1960). *Live, orally given poliovirus vaccine: Effects of rapid mass immunization on population under conditions of massive enteric infection with other viruses*. Journal of the American Medical Association, 173(14):1521–1526. ISSN 23768118. doi: 10.1001/jama.1960.03020320001001

[37] O. Kew and M. Pallansch (2018). *Breaking the last chains of poliovirus transmission: Progress and challenges in global polio eradication*. Annual Review of Virology, 5:427–451. ISSN 23270578. doi:10.1146/annurev-virology-101416-041749

[38] WHO (2019). *Polio Now – GPEI*. `https://polioeradication.org/polio-today/polio-now/` (Accessed: 2022-02-02)

[39] F. Fenner, D. A. Henderson, I. Arita, Z. Jezek, and I. D. Ladnyi (1988). *Smallpox and its Eradication*. World Health Organisation, Geneva. ISBN 9241561106

[40] F. P. Polack, S. J. Thomas, N. Kitchin, J. Absalon, A. Gurtman, S. Lockhart, J. L. Perez, G. Pérez Marc, E. D. Moreira, C. Zerbini, et al. (2020). *Safety and Efficacy of the BNT162b2 mRNA Covid-19 Vaccine*. New England Journal of Medicine, 383(27):2603–2615. ISSN 0028-4793. doi:10.1056/nejmoa2034577

[41] L. R. Baden, H. M. El Sahly, B. Essink, K. Kotloff, S. Frey, R. Novak, D. Diemert, S. A. Spector, N. Rouphael, C. B. Creech, et al. (2021). *Efficacy and Safety of the mRNA-1273 SARS-CoV-2 Vaccine*. New England Journal of Medicine, 384(5):403–416. ISSN 0028-4793. doi:10.1056/nejmoa2035389

[42] J. Sadoff, G. Gray, A. Vandebosch, V. Cárdenas, G. Shukarev, B. Grinsztejn, P. A. Goepfert, C. Truyers, H. Fennema, B. Spiessens, et al. (2021). *Safety and Efficacy of Single-Dose Ad26.COV2.S Vaccine against Covid-19*. New England Journal of Medicine, 384(23):2187–2201. ISSN 0028-4793. doi:10.1056/nejmoa2101544

[43] M. Voysey, S. A. C. Clemens, S. A. Madhi, L. Y. Weckx, P. M. Folegatti, P. K. Aley, B. Angus, V. L. Baillie, S. L. Barnabas, Q. E. Bhorat, et al. (2021). *Safety and efficacy of the ChAdOx1 nCoV-19 vaccine (AZD1222) against SARS-CoV-2: an interim analysis of four randomised controlled trials in Brazil, South Africa, and the UK*. Lancet (London, England), 397(10269):99–111. ISSN 1474-547X. doi:10.1016/S0140-6736(20)32661-1

[44] S. J. Flint, L. W. Enquist, V. R. Racaniello, and A. M. Skalka (2004). *Principles of Virology: Molecular Biology, Pathogenesis, and Control of Animal Viruses*. American Society for Microbiology, second edition. ISBN 9781555812591

[45] M. J. Adams, E. J. Lefkowitz, A. M. King, B. Harrach, R. L. Harrison, N. J. Knowles, A. M. Kropinski, M. Krupovic, J. H. Kuhn, A. R. Mushegian, et al. (2017). *50 years of the International Committee on Taxonomy of Viruses: progress and prospects*. Archives of Virology, 162(5):1441–1446. ISSN 03048608. doi:10.1007/s00705-016-3215-y

[46] A. Lwoff, R. Horne, and P. Tournier (1962). *A System of Viruses*. Cold Spring Harbor Symposia on Quantitative Biology, 27:51–55. ISSN 0091-7451. doi:10.1101/SQB.1962.027.001.008

[47] *ICTV Report on Virus Classification and Taxon Nomenclature*. `https://talk.ictvonline.org/ictv-reports/ictv_online_report/` (Accessed: 2021-09-03)

[48] P. J. Walker, S. G. Siddell, E. J. Lefkowitz, A. R. Mushegian, E. M. Adriaenssens, P. Alfenas-Zerbini, A. J. Davison, D. M. Dempsey, B. E. Dutilh, M. L. García, et al. (2021). *Changes to virus taxonomy and to the International Code of Virus Classification and Nomenclature ratified by the International Committee on Taxonomy of Viruses (2021)*. Archives of Virology, 166(9):2633–2648. ISSN 14328798. doi:10.1007/s00705-021-05156-1

[49] E. V. Koonin, M. Krupovic, and V. I. Agol (2021). *The Baltimore Classification of Viruses 50 Years Later: How Does It Stand in the Light of Virus Evolution?* Microbiology and Molecular Biology Reviews, 85(3). ISSN 1092-2172. doi:10.1128/mmbr.00053-21

[50] D. Baltimore (1971). *Expression of animal virus genomes*. Bacteriological Reviews, 35(3):235–

241. ISSN 0005-3678. doi:10.1128/br.35.3.235-241.1971

[51] W. P. Rowe, R. J. Huebner, L. K. Gilmore, R. H. Parrott, and T. G. Ward (1953). *Isolation of a Cytopathogenic Agent from Human Adenoids Undergoing Spontaneous Degeneration in Tissue Culture*. Proceedings of the Society for Experimental Biology and Medicine, 84(3):570–573. ISSN 15353699. doi:10.3181/00379727-84-20714

[52] *HAdV Working Group*. `http://hadvwg.gmu.edu/` (Accessed: 2022-04-04)

[53] (2012). *Reoviridae*. In A. M. Q. King; M. J. Adams; E. B. Carstens; and E. J. Lefkowitz, editors, *Virus Taxonomy*, pp. 541–637. Elsevier, San Diego. ISBN 978-0-12-384684-6. doi:10.1016/B978-0-12-384684-6.00051-3

[54] R. Duncan, D. Horne, L. William Cashdollar, W. K. Joklik, and P. W. Lee (1990). *Identification of conserved domains in the cell attachment proteins of the three serotypes of reovirus*. Virology, 174(2):399–409. ISSN 10960341. doi:10.1016/0042-6822(90)90093-7

[55] M. L. Nibert, T. S. Dermody, and B. N. Fields (1990). *Structure of the reovirus cell-attachment protein: a model for the domain organization of sigma 1*. Journal of Virology, 64(6):2976–2989. ISSN 0022-538X. doi:10.1128/jvi.64.6.2976-2989.1990

[56] (2012). *Family - Adenoviridae*. In A. M. Q. King; M. J. Adams; E. B. Carstens; and E. J. Lefkowitz, editors, *Virus Taxonomy*, pp. 125–141. Elsevier, San Diego. ISBN 978-0-12-384684-6. doi:https://doi.org/10.1016/B978-0-12-384684-6.00009-4

[57] C. M. Robinson, G. Singh, J. Y. Lee, S. Dehghan, J. Rajaiya, E. B. Liu, M. A. Yousuf, R. A. Betensky, M. S. Jones, D. W. Dyer, et al. (2013). *Molecular evolution of human adenoviruses*. Scientific Reports, 3(1):1812. ISSN 20452322. doi:10.1038/srep01812

[58] D. L. D. Caspar and A. Klug (1962). *Physical Principles in the Construction of Regular Viruses*. Cold Spring Harbor Symposia on Quantitative Biology, 27:1–24. ISSN 0091-7451. doi:10.1101/SQB.1962.027.001.005

[59] P. L. Stewart, R. M. Burnett, M. Cyrklaff, and S. D. Fuller (1991). *Image reconstruction reveals the complex molecular organization of adenovirus*. Cell, 67(1):145–154. ISSN 00928674. doi:10.1016/0092-8674(91)90578-M

[60] B. V. Prasad and M. F. Schmid (2012). *Principles of virus structural organization*. Advances in Experimental Medicine and Biology, 726:17–47. ISSN 00652598. doi:10.1007/978-1-4614-0980-9_3

[61] C. M. Fabry, M. Rosa-Calatrava, J. F. Conway, C. Zubieta, S. Cusack, R. W. Ruigrok, and G. Schoehn (2005). *A quasi-atomic model of human adenovirus type 5 capsid*. EMBO Journal, 24(9):1645–1654. ISSN 02614189. doi:10.1038/sj.emboj.7600653

[62] S. A. Nicklin, E. Wu, G. R. Nemerow, and A. H. Baker (2005). *The influence of adenovirus fiber structure and function on vector development for gene therapy*. Molecular Therapy, 12(3):384–393. ISSN 15250016. doi:10.1016/j.ymthe.2005.05.008

[63] C. Zubieta, G. Schoehn, J. Chroboczek, and S. Cusack (2005). *The structure of the human adenovirus 2 penton*. Molecular Cell, 17(1):121–135. ISSN 10972765. doi:10.1016/j.molcel.2004.11.041

[64] H. Liu, L. Wu, and Z. H. Zhou (2011). *Model of the trimeric fiber and its interactions with the pentameric penton base of human adenovirus by cryo-electron microscopy.* Journal of molecular biology, 406(5):764–774. ISSN 1089-8638. doi:10.1016/j.jmb.2010.11.043

[65] V. Abrishami, S. L. Ilca, J. Gomez-Blanco, I. Rissanen, J. M. de la Rosa-Trevín, V. S. Reddy, J. M. Carazo, and J. T. Huiskonen (2021). *Localized reconstruction in Scipion expedites the analysis of symmetry mismatches in cryo-EM data*. Progress in Biophysics and Molecular Biology, 160:43–52. ISSN 00796107. doi:10.1016/j.pbiomolbio.2020.05.004

[66] K. Rafie, A. Lenman, J. Fuchs, A. Rajan, N. Arnberg, and L. A. Carlson (2021). *The structure of enteric human adenovirus 41 — A leading cause of diarrhea in children*. Science Advances, 7(2):eabe0974. ISSN 23752548. doi:10.1126/sciadv.abe0974

[67] *ViralZone - Mastadenovirus*. `https://viralzone.expasy.org/183?outline=all_by_`

species (Accessed: 2021-09-10)

[68] *ViralZone - Orthoreovirus*. https://viralzone.expasy.org/105 (Accessed: 2021-09-10)

[69] V. S. Reddy, S. K. Natchiar, P. L. Stewart, and G. R. Nemerow (2010). *Crystal structure of human adenovirus at 3.5 Å resolution*. Science, 329(5995):1071–1075. ISSN 00368075. doi: 10.1126/science.1187292

[70] J. Perez-Vargas, R. C. Vaughan, C. Houser, K. M. Hastie, C. C. Kao, and G. R. Nemerow (2014). *Isolation and Characterization of the DNA and Protein Binding Activities of Adenovirus Core Protein V*. Journal of Virology, 88(16):9287–9296. ISSN 0022-538X. doi:10.1128/jvi.00935-14

[71] K. A. Dryden, G. Wang, M. Yeager, M. L. Nibert, K. M. Coombs, D. B. Furlong, B. N. Fields, and T. S. Baker (1993). *Early steps in reovirus infection are associated with dramatic changes in supramolecular structure and protein conformation: Analysis of virions and subviral particles by cryoelectron microscopy and image reconstruction*. Journal of Cell Biology, 122(5):1023–1041. ISSN 00219525. doi:10.1083/jcb.122.5.1023

[72] S. Liemann, K. Chandran, T. S. Baker, M. L. Nibert, and S. C. Harrison (2002). *Structure of the reovirus membrane-penetration protein, $\mu 1$, in a complex with its protector protein, $\sigma 3$*. Cell, 108(2):283–295. ISSN 00928674. doi:10.1016/S0092-8674(02)00612-8

[73] R. D. Fraser, D. B. Furlong, B. L. Trus, M. L. Nibert, B. N. Fields, and A. C. Steven (1990). *Molecular structure of the cell-attachment protein of reovirus: correlation of computer-processed electron micrographs with sequence-based predictions*. Journal of Virology, 64(6):2990–3000. ISSN 0022-538X. doi:10.1128/jvi.64.6.2990-3000.1990

[74] D. B. Furlong, M. L. Nibert, and B. N. Fields (1988). *Sigma 1 protein of mammalian reoviruses extends from the surfaces of viral particles*. Journal of Virology, 62(1):246–256. ISSN 0022-538X. doi:10.1128/jvi.62.1.246-256.1988

[75] K. M. Guglielmi, E. M. Johnson, T. Stehle, and T. S. Dermody (2006). *Attachment and cell entry of mammalian orthoreovirus*. doi:10.1007/3-540-30773-7_1. http://link.springer.com/10.1007/3-540-30773-7_1

[76] M. Pan, A. L. Alvarez-cabrera, J. S. Kang, L. Wang, and C. Fan (2021). *Asymmetric reconstruction of mammalian reovirus reveals interactions among RNA , transcriptional factor $\mu 2$, and other proteins*. NATURE COMMUNICATIONS, 12(1):4176. doi:10.1038/S41467-021-24455-4

[77] T. Stehle and T. S. Dermody (2003). *Structural evidence for common functions and ancestry of the reovirus and adenovirus attachment proteins*. Reviews in Medical Virology, 13(2):123–132. ISSN 10529276. doi:10.1002/rmv.379

[78] M. H. Dietrich, K. M. Ogden, J. M. Long, R. Ebenhoch, A. Thor, T. S. Dermody, and T. Stehle (2018). *Structural and Functional Features of the Reovirus $\sigma 1$ Tail*. Journal of Virology, 92(14). ISSN 0022-538X. doi:10.1128/jvi.00336-18

[79] M. J. Van Raaij, A. Mitrakl, G. Lavigne, and S. Cusack (1999). *A triple β-spiral in the adenovirus fibre shaft reveals a new structural motif for a fibrous protein*. Nature, 401(6756):935–938. ISSN 00280836. doi:10.1038/44880

[80] S. Lindert, M. Silvestry, T.-M. Mullen, G. R. Nemerow, and P. L. Stewart (2009). *Cryo-Electron Microscopy Structure of an Adenovirus-Integrin Complex Indicates Conformational Changes in both Penton Base and Integrin*. Journal of Virology, 83(22):11491–11501. ISSN 0022-538X. doi: 10.1128/jvi.01214-09

[81] D. Veesler, K. Cupelli, M. Burger, P. Graeber, T. Stehle, and J. E. Johnson (2014). *Single-particle EM reveals plasticity of interactions between the adenovirus penton base and integrin $\alpha V\beta 3$*. Proceedings of the National Academy of Sciences of the United States of America, 111(24):8815–8819. ISSN 10916490. doi:10.1073/pnas.1404575111

[82] J. Snijder, V. S. Reddy, E. R. May, W. H. Roos, G. R. Nemerow, and G. J. L. Wuite (2013). *Integrin and Defensin Modulate the Mechanical Properties of Adenovirus*. Journal of Virology, 87(5):2756–2766. ISSN 0022-538X. doi:10.1128/jvi.02516-12

[83] C. J. Burckhardt, M. Suomalainen, P. Schoenenberger, K. Boucke, S. Hemmi, and U. F. Greber

(2011). *Drifting motions of the adenovirus receptor CAR and immobile integrins initiate virus uncoating and membrane lytic protein exposure*. Cell Host and Microbe, 10(2):105–117. ISSN 19313128. doi:10.1016/j.chom.2011.07.006

[84] J. G. Smith, M. Silvestry, S. Lindert, W. Lu, G. R. Nemerow, and P. L. Stewart (2010). *Insight into the mechanisms of adenovirus capsid disassembly from studies of defensin neutralization*. PLoS Pathogens, 6(6):1000959. ISSN 15537366. doi:10.1371/journal.ppat.1000959

[85] C. M. Wiethoff, H. Wodrich, L. Gerace, and G. R. Nemerow (2005). *Adenovirus Protein VI Mediates Membrane Disruption following Capsid Disassembly*. Journal of Virology, 79(4):1992–2000. ISSN 0022-538X. doi:10.1128/jvi.79.4.1992-2000.2005

[86] E. J. Kremer and G. R. Nemerow (2015). *Adenovirus Tales: From the Cell Surface to the Nuclear Pore Complex*. doi:10.1371/journal.ppat.1004821. `https://journals.plos.org/plospathogens/article?id=10.1371/journal.ppat.1004821`

[87] U. F. Greber and J. W. Flatt (2019). *Adenovirus Entry: From Infection to Immunity*. Annual Review of Virology, 6:177–197. ISSN 23270578. doi:10.1146/annurev-virology-092818-015550

[88] S. Luisoni, M. Suomalainen, K. Boucke, L. B. Tanner, M. R. Wenk, X. L. Guan, M. Grzybek, U. Coskun, and U. F. Greber (2015). *Co-option of membrane wounding enables virus penetration into cells*. Cell Host and Microbe, 18(1):75–85. ISSN 19346069. doi:10.1016/j.chom.2015.06.006

[89] K. H. Bremner, J. Scherer, J. Yi, M. Vershinin, S. P. Gross, and R. B. Vallee (2009). *Adenovirus Transport via Direct Interaction of Cytoplasmic Dynein with the Viral Capsid Hexon Subunit*. Cell Host and Microbe, 6(6):523–535. ISSN 19313128. doi:10.1016/j.chom.2009.11.006

[90] L. C. Trotman, N. Mosberger, M. Fornerod, R. P. Stidwill, and U. F. Greber (2001). *Import of adenovirus DNA involves the nuclear pore complex receptor CAN/Nup214 and histone H1*. Nature Cell Biology, 3(12):1092–1100. ISSN 14657392. doi:10.1038/ncb1201-1092

[91] S. Strunze, M. F. Engelke, I. H. Wang, D. Puntener, K. Boucke, S. Schleich, M. Way, P. Schoenenberger, C. J. Burckhardt, and U. F. Greber (2011). *Kinesin-1-mediated capsid disassembly and disruption of the nuclear pore complex promote virus infection*. Cell Host and Microbe, 10(3):210–223. ISSN 19313128. doi:10.1016/j.chom.2011.08.010

[92] J. W. Flatt and U. F. Greber (2017). *Viral mechanisms for docking and delivering at nuclear pore complexes*. doi:10.1016/j.semcdb.2017.05.008

[93] H. Wodrich, A. Cassany, M. A. D'Angelo, T. Guan, G. Nemerow, and L. Gerace (2006). *Adenovirus Core Protein pVII Is Translocated into the Nucleus by Multiple Import Receptor Pathways*. Journal of Virology, 80(19):9608–9618. ISSN 0022-538X. doi:10.1128/jvi.00850-06

[94] C. E. Hindley, F. J. Lawrence, and D. A. Matthews (2007). *A role for transportin in the nuclear import of adenovirus core proteins and DNA*. Traffic, 8(10):1313–1322. ISSN 13989219. doi:10.1111/j.1600-0854.2007.00618.x

[95] K. A. Karen and P. Hearing (2011). *Adenovirus Core Protein VII Protects the Viral Genome from a DNA Damage Response at Early Times after Infection*. Journal of Virology, 85(9):4135–4142. ISSN 0022-538X. doi:10.1128/jvi.02540-10

[96] F. Georgi and U. F. Greber (2020). *The Adenovirus Death Protein – a small membrane protein controls cell lysis and disease*. FEBS Letters, 594(12):1861–1878. ISSN 18733468. doi:10.1002/1873-3468.13848

[97] K. Doronin, K. Toth, M. Kuppuswamy, P. Krajcsi, A. E. Tollefson, and W. S. Wold (2003). *Overexpression of the ADP (E3-11.6K) protein increases cell lysis and spread of Adenovirus*. Virology, 305(2):378–387. ISSN 00426822. doi:10.1006/viro.2002.1772

[98] A. E. Tollefson, A. Scaria, T. W. Hermiston, J. S. Ryerse, L. J. Wold, and W. S. Wold (1996). *The adenovirus death protein (E3-11.6K) is required at very late stages of infection for efficient cell lysis and release of adenovirus from infected cells*. Journal of Virology, 70(4):2296–2306. ISSN 0022-538X. doi:10.1128/jvi.70.4.2296-2306.1996

[99] M. Ehrlich, W. Boll, A. Van Oijen, R. Hariharan, K. Chandran, M. L. Nibert, and T. Kirchhausen (2004). *Endocytosis by random initiation and stabilization of clathrin-coated pits*. Cell,

118(5):591–605. ISSN 00928674. doi:10.1016/j.cell.2004.08.017

[100] M. S. Maginnis, B. A. Mainou, A. Derdowski, E. M. Johnson, R. Zent, and T. S. Dermody (2008). *NPXY Motifs in the β1 Integrin Cytoplasmic Tail Are Required for Functional Reovirus Entry*. Journal of Virology, 82(7):3181–3191. ISSN 0022-538X. doi:10.1128/jvi.01612-07

[101] E. S. Barton, B. E. Youree, D. H. Ebert, J. C. Forrest, J. L. Connolly, T. Valyi-Nagy, K. Washington, J. D. Wetzel, and T. S. Dermody (2003). *Utilization of sialic acid as a coreceptor is required for reovirus-induced biliary disease*. Journal of Clinical Investigation, 111(12):1823–1833. ISSN 00219738. doi:10.1172/JCI16303

[102] P. Danthi, G. H. Holm, T. Stehle, and T. S. Dermody (2013). *Reovirus receptors, cell entry, and proapoptotic signaling*. Advances in Experimental Medicine and Biology, 790:42–71. ISSN 00652598. doi:10.1007/978-1-4614-7651-1_3

[103] M. S. Maginnis, J. C. Forrest, S. A. Kopecky-Bromberg, S. K. Dickeson, S. A. Santoro, M. M. Zutter, G. R. Nemerow, J. M. Bergelson, and T. S. Dermody (2006). *β1 Integrin Mediates Internalization of Mammalian Reovirus*. Journal of Virology, 80(6):2760–2770. ISSN 0022-538X. doi:10.1128/jvi.80.6.2760-2770.2006

[104] L. J. Sturzenbecker, M. Nibert, D. Furlong, and B. N. Fields (1987). *Intracellular digestion of reovirus particles requires a low pH and is an essential step in the viral infectious cycle*. Journal of Virology, 61(8):2351–2361. ISSN 0022-538X. doi:10.1128/jvi.61.8.2351-2361.1987

[105] M. Koehler, S. J. Petitjean, J. Yang, P. Aravamudhan, X. Somoulay, C. Lo Giudice, M. A. Poncin, A. C. Dumitru, T. S. Dermody, and D. Alsteens (2021). *Reovirus directly engages integrin to recruit clathrin for entry into host cells*. Nature Communications, 12(1). ISSN 20411723. doi:10.1038/s41467-021-22380-0

[106] M. L. Nibert and B. N. Fields (1992). *A carboxy-terminal fragment of protein mu 1/mu 1C is present in infectious subvirion particles of mammalian reoviruses and is proposed to have a role in penetration*. Journal of Virology, 66(11):6408–6418. ISSN 0022-538X. doi:10.1128/jvi.66.11.6408-6418.1992

[107] I. F. de Castro, P. F. Zamora, L. Ooms, J. J. Fernández, C. M. Lai, B. A. Mainou, T. S. Dermody, and C. Risco (2014). *Reovirus forms neo-organelles for progeny particle assembly within reorganized cell membranes*. mBio, 5(1). ISSN 21612129. doi:10.1128/mBio.00931-13

[108] P. Danthi, C. M. Coffey, J. S. Parker, T. W. Abel, and T. S. Dermody (2008). *Independent regulation of reovirus membrane penetration and apoptosis by the μ1 ϕ domain*. PLoS Pathogens, 4(12):e1000248. ISSN 15537366. doi:10.1371/journal.ppat.1000248

[109] C. M. Lai, B. A. Mainou, K. S. Kim, and T. S. Dermody (2013). *Directional release of reovirus from the apical surface of polarized endothelial cells*. mBio, 4(2). ISSN 21612129. doi:10.1128/mBio.00049-13

[110] K. Kosulin (2019). *Intestinal HAdV Infection: Tissue Specificity, Persistence, and Implications for Antiviral Therapy*. doi:10.3390/v11090804. `https://pubmed.ncbi.nlm.nih.gov/31480296/`

[111] C. T. Garnett, D. Erdman, W. Xu, and L. R. Gooding (2002). *Prevalence and Quantitation of Species C Adenovirus DNA in Human Mucosal Lymphocytes*. Journal of Virology, 76(21):10608–10616. ISSN 0022-538X. doi:10.1128/jvi.76.21.10608-10616.2002

[112] E. Ford, K. E. Nelson, and D. Warren (1987). *Epidemiology of epidemic keratoconjunctivitis*. Epidemiologic Reviews, 9(1):244–261. ISSN 1478-6729. doi:10.1093/oxfordjournals.epirev.a036304

[113] N. Arnberg, A. H. Kidd, K. Edlund, J. Nilsson, P. Pring-Åkerblom, and G. Wadell (2002). *Adenovirus type 37 binds to cell surface sialic acid through a charge-dependent interaction*. Virology, 302(1):33–43. ISSN 00426822. doi:10.1006/viro.2002.1503

[114] I. Engelmann, I. Madisch, H. Pommer, and A. Heim (2006). *An outbreak of epidemic keratoconjunctivitis caused by a new intermediate adenovirus 22/H8 identified by molecular typing.* Clinical infectious diseases : an official publication of the Infectious Diseases Society of America, 43(7):e64–e66. ISSN 15376591. doi:10.1086/507533

[115] H. Kaneko, T. Iida, H. Ishiko, T. Ohguchi, T. Ariga, Y. Tagawa, K. Aoki, S. Ohno, and T. Suzutani (2009). *Analysis of the complete genome sequence of epidemic keratoconjunctivitis-related human adenovirus type 8, 19, 37 and a novel serotype*. Journal of General Virology, 90(6):1471–1476. ISSN 00221317. doi:10.1099/vir.0.009225-0

[116] C. M. Robinson, G. Singh, C. Henquell, M. P. Walsh, H. Peigue-Lafeuille, D. Seto, M. S. Jones, D. W. Dyer, and J. Chodosh (2011). *Computational analysis and identification of an emergent human adenovirus pathogen implicated in a respiratory fatality*. Virology, 409(2):141–147. ISSN 00426822. doi:10.1016/j.virol.2010.10.020

[117] A. Lenman, A. M. Liaci, Y. Liu, C. Årdahl, A. Rajan, E. Nilsson, W. Bradford, L. Kaeshammer, M. S. Jones, L. Frängsmyr, et al. (2015). *Human adenovirus 52 uses sialic acid-containing glycoproteins and the coxsackie and adenovirus receptor for binding to target cells.* PLoS pathogens, 11(2):e1004657. ISSN 1553-7374. doi:10.1371/journal.ppat.1004657

[118] A. H. Kidd, J. Chroboczek, S. Cusack, and R. W. Ruigrok (1993). *Adenovirus type 40 virions contain two distinct fibers*. Virology, 192(1):73–84. ISSN 00426822. doi:10.1006/viro.1993.1009

[119] Y. Hung-Yueh, N. Pieniazek, D. Pieniazek, H. Gelderblom, and R. B. Luftig (1994). *Human adenovirus type 41 contains two fibers*. Virus Research, 33(2):179–198. ISSN 01681702. doi:10.1016/0168-1702(94)90054-X

[120] T. Kojaoghlanian, P. Flomenberg, and M. S. Horwitz (2003). *The impact of adenovirus infection on the immunocompromised host*. Reviews in Medical Virology, 13(3):155–171. ISSN 10529276. doi:10.1002/rmv.386

[121] E. Ponterio and L. Gnessi (2015). *Adenovirus 36 and obesity: An overview*. Viruses, 7(7):3719–3740. ISSN 19994915. doi:10.3390/v7072787

[122] M.-Y. Y. Xu, B. Cao, D.-F. F. Wang, J.-H. H. Guo, K.-L. L. Chen, M. Shi, J. Yin, and Q.-B. B. Lu (2015). *Human Adenovirus 36 Infection Increased the Risk of Obesity: A Meta-Analysis Update.* Medicine, 94(51):e2357. ISSN 1536-5964. doi:10.1097/MD.0000000000002357

[123] J. Kim, H. Na, J. A. Kim, and J. H. Nam (2020). *What we know and what we need to know about adenovirus 36-induced obesity*. International Journal of Obesity, 44(6):1197–1209. ISSN 14765497. doi:10.1038/s41366-020-0536-4

[124] A. B. Sabin (1959). *Reoviruses: A new group of respiratory and enteric viruses formerly classified as ECHO type 10 is described*. Science, 130(3386):1387–1389. ISSN 0036-8075. doi:10.1126/science.130.3386.1387

[125] D. M. Sutherland, P. Aravamudhan, and T. S. Dermody (2018). *An Orchestra of Reovirus Receptors: Still Searching for the Conductor*. Advances in Virus Research, 100:223–246. ISSN 15578399. doi:10.1016/bs.aivir.2017.10.005

[126] M. Keroack and B. N. Fields (1986). *Viral shedding and transmission between hosts determined by reovirus L2 gene*. Science, 232(4758):1635–1638. ISSN 00368075. doi:10.1126/science.3012780

[127] J. L. Wolf, D. H. Rubin, R. Finberg, R. S. Kauffman, A. H. Sharpe, J. S. Trier, and B. N. Fields (1981). *Intestinal M cells: A pathway for entry of reovirus into the host*. Science, 212(4493):471–472. ISSN 00368075. doi:10.1126/science.6259737

[128] D. M. Bass, J. S. Trier, R. Dambrauskas, and J. L. Wolf (1988). *Reovirus type I infection of small intestinal epithelium in suckling mice and its effect on M cells*. Laboratory Investigation, 58(2):226–235. ISSN 00236837

[129] K. L. Tyler, D. A. McPhee, and B. N. Fields (1986). *Distinct pathways of viral spread in the host determined by reovirus S1 gene segment*. Science, 233(4765):770–774. ISSN 00368075. doi:10.1126/science.3016895

[130] H. L. Weiner, M. L. Powers, and B. N. Fields Fields (1980). *Absolute linkage of virulence and central nervous system cell tropism of reoviruses to viral hemagglutinin*. Journal of Infectious Diseases, 141(5):609–616. ISSN 00221899. doi:10.1093/infdis/141.5.609

[131] H. L. Weiner, D. Drayna, D. R. Averill, and B. N. Fields (1977). *Molecular basis of reovirus virulence: role of the S1 gene*. Proceedings of the National Academy of Sciences of the United

States of America, 74(12):5744–5748. ISSN 0027-8424. doi:10.1073/PNAS.74.12.5744

[132] M. Tardieu and H. L. Weiner (1982). *Viral receptors on isolated murine and human ependymal cells*. Science, 215(4531):419–421. ISSN 00368075. doi:10.1126/science.6276976

[133] M. A. Dichter and H. L. Weiner (1984). *Infection of neuronal cell cultures with reovirus mimics in vitro patterns of neurotropism*. Annals of Neurology, 16(5):603–610. ISSN 15318249. doi:10.1002/ana.410160512

[134] J. Stencel-Baerenwald, K. Reiss, B. S. Blaum, D. Colvin, X. N. Li, T. Abel, K. Boyd, T. Stehle, and T. S. Dermody (2015). *Glycan engagement dictates hydrocephalus induction by serotype 1 reovirus*. mBio, 6(2). ISSN 21507511. doi:10.1128/mBio.02356-14

[135] J. M. Frierson, A. J. Pruijssers, J. L. Konopka, D. M. Reiter, T. W. Abel, T. Stehle, and T. S. Dermody (2012). *Utilization of Sialylated Glycans as Coreceptors Enhances the Neurovirulence of Serotype 3 Reovirus*. Journal of Virology, 86(24):13164–13173. ISSN 0022-538X. doi:10.1128/jvi.01822-12

[136] E. S. Barton, J. L. Connolly, J. C. Forrest, J. D. Chappell, and T. S. Dermody (2001). *Utilization of sialic acid as a coreceptor enhances reovirus attachment by multistep adhesion strengthening*. Journal of Biological Chemistry, 276(3):2200–2211. ISSN 00219258. doi:10.1074/jbc.M004680200

[137] J. L. Connolly, E. S. Barton, and T. S. Dermody (2001). *Reovirus Binding to Cell Surface Sialic Acid Potentiates Virus-Induced Apoptosis*. Journal of Virology, 75(9):4029–4039. ISSN 0022-538X. doi:10.1128/jvi.75.9.4029-4039.2001

[138] T. S. Dermody, J. Parker, and B. Sherry (2013). *Orthoreoviruses*. Fields Virology, 2:1304—-1346

[139] R. Bouziat, R. Hinterleitner, J. J. Brown, J. E. Stencel-Baerenwald, M. Ikizler, T. Mayassi, M. Meisel, S. M. Kim, V. Discepolo, A. J. Pruijssers, et al. (2017). *Reovirus infection triggers inflammatory responses to dietary antigens and development of celiac disease*. Science, 356(6333):44–50. ISSN 10959203. doi:10.1126/science.aah5298

[140] D. Xia, L. J. Henry, R. D. Gerard, and J. Deisenhofer (1994). *Crystal structure of the receptor-binding domain of adenovirus type 5 fiberprotein at 1.7 Å resolution*. Structure, 2(12):1259–1270. ISSN 09692126. doi:10.1016/S0969-2126(94)00126-X

[141] A. C. Stasiak and T. Stehle (2020). *Human adenovirus binding to host cell receptors: a structural view*. doi:10.1007/s00430-019-00645-2. `https://pubmed.ncbi.nlm.nih.gov/31784892/`

[142] J. M. Bergelson, J. A. Cunningham, G. Droguett, E. A. Kurt-Jones, A. Krithivas, J. S. Hong, M. S. Horwitz, R. L. Crowell, and R. W. Finberg (1997). *Isolation of a common receptor for coxsackie B viruses and adenoviruses 2 and 5*. Science, 275(5304):1320–1323. ISSN 00368075. doi:10.1126/science.275.5304.1320

[143] M. C. Bewley, K. Springer, Y.-B. B. Zhang, P. Freimuth, and J. M. Flanagan (1999). *Structural analysis of the mechanism of adenovirus binding to its human cellular receptor, CAR*. Science, 286(5444):1579–1583. ISSN 00368075. doi:10.1126/science.286.5444.1579

[144] E. Seiradake, H. Lortat-Jacob, O. Billet, E. J. Kremer, and S. Cusack (2006). *Structural and mutational analysis of human Ad37 and canine adenovirus 2 fiber heads in complex with the D1 domain of coxsackie and adenovirus receptor*. Journal of Biological Chemistry, 281(44):33704–33716. ISSN 00219258. doi:10.1074/jbc.M605316200

[145] M. J. Van Raaij, E. Chouin, H. Van der Zandt, J. M. Bergelson, and S. Cusack (2000). *Dimeric structure of the coxsackievirus and adenovirus receptor D1 domain at 1.7 Å resolution*. Structure, 8(11):1147–1155. ISSN 09692126. doi:10.1016/S0969-2126(00)00528-1

[146] R. C. Riley-Vargas, D. B. Gill, C. Kemper, M. K. Liszewski, and J. P. Atkinson (2004). *CD46: expanding beyond complement regulation*. Trends in Immunology, 25(9):496–503. ISSN 1471-4906. doi:10.1016/J.IT.2004.07.004

[147] M. K. Liszewski, T. W. Post, and J. P. Atkinson (1991). *Membrane cofactor protein (MCP or CD46): Newest member of the regulators of complement activation gene cluster*. doi:10.1146/annurev.iy.09.040191.002243. `https://pubmed.ncbi.nlm.nih.gov/1910685/`

[148] F. Santoro, P. E. Kennedy, G. Locatelli, M. S. Malnati, E. A. Berger, and P. Lusso (1999). *CD46 is a cellular receptor for human herpesvirus 6*. Cell, 99(7):817–827. ISSN 00928674. doi: 10.1016/S0092-8674(00)81678-5

[149] C. Santiago, M. L. Celma, T. Stehle, and J. M. Casasnovas (2010). *Structure of the measles virus hemagglutinin bound to the CD46 receptor*. Nature Structural and Molecular Biology, 17(1):124–130. ISSN 15459985. doi:10.1038/nsmb.1726

[150] A. Segerman, J. P. Atkinson, M. Marttila, V. Dennerquist, G. Wadell, and N. Arnberg (2003). *Adenovirus Type 11 Uses CD46 as a Cellular Receptor*. Journal of Virology, 77(17):9183–9191. ISSN 0022-538X. doi:10.1128/jvi.77.17.9183-9191.2003

[151] M. Marttila, D. Persson, D. Gustafsson, M. K. Liszewski, J. P. Atkinson, G. Wadell, and N. Arnberg (2005). *CD46 Is a Cellular Receptor for All Species B Adenoviruses except Types 3 and 7*. Journal of Virology, 79(22):14429–14436. ISSN 0022-538X. doi:10.1128/jvi.79.22.14429-14436.2005

[152] B. D. Persson, D. M. Reiter, M. Marttila, Y. F. Mei, J. M. Casasnovas, N. Arnberg, and T. Stehle (2007). *Adenovirus type 11 binding alters the conformation of its receptor CD46*. Nature Structural and Molecular Biology, 14(2):164–166. ISSN 15459993. doi:10.1038/nsmb1190

[153] K. Cupelli, S. Müller, B. D. Persson, M. Jost, N. Arnberg, and T. Stehle (2010). *Structure of Adenovirus Type 21 Knob in Complex with CD46 Reveals Key Differences in Receptor Contacts among Species B Adenoviruses*. Journal of Virology, 84(7):3189–3200. ISSN 0022-538X. doi: 10.1128/jvi.01964-09

[154] O. J. Harrison, J. Brasch, G. Lasso, P. S. Katsamba, G. Ahlsen, B. Honig, and L. Shapiro (2016). *Structural basis of adhesive binding by desmocollins and desmogleins*. Proceedings of the National Academy of Sciences of the United States of America, 113(26):7160–7165. ISSN 10916490. doi: 10.1073/pnas.1606272113

[155] H. Wang, Z. Li, Y. Liu, J. Persson, I. Beyer, T. Möller, D. Koyuncu, M. R. Drescher, R. Strauss, X.-B. Zhang, et al. (2011). *Desmoglein 2 is a receptor for adenovirus serotypes 3, 7, 11 and 14*. Nature Medicine, 17(1):96–104. ISSN 1078-8956. doi:10.1038/nm.2270

[156] E. Vassal-Stermann, G. Effantin, C. Zubieta, W. Burmeister, H. Wang, A. Lieber, G. Schoehn, P. Fender, F. Iseni, H. Wang, et al. (2019). *Cryo-EM structure of adenovirus type 3 fibre with desmoglein 2 shows a novel mode of 2 receptor engagement 3 4 5 6*. Nature Communications, 10(1):1181. ISSN 2041-1723. doi:10.1101/471383

[157] E. Vassal-Stermann, M. Mottet, C. Ducournau, F. Iseni, C. Vragniau, H. Wang, C. Zubieta, A. Lieber, and P. Fender (2018). *Mapping of Adenovirus of serotype 3 fibre interaction to desmoglein 2 revealed a novel 'non-classical' mechanism of viral receptor engagement*. Scientific Reports, 8(1). ISSN 20452322. doi:10.1038/s41598-018-26871-x

[158] N. Arnberg, K. Edlund, A. H. Kidd, and G. Wadell (2000). *Adenovirus Type 37 Uses Sialic Acid as a Cellular Receptor*. Journal of Virology, 74(1):42–48. ISSN 0022-538X. doi:10.1128/jvi.74.1.42-48.2000

[159] N. Arnberg, A. H. Kidd, K. Edlund, F. Olfat, and G. Wadell (2000). *Initial Interactions of Subgenus D Adenoviruses with A549 Cellular Receptors: Sialic Acid versus αvIntegrins*. Journal of Virology, 74(16):7691–7693. ISSN 0022-538X. doi:10.1128/jvi.74.16.7691-7693.2000

[160] S. M. Cashman, D. J. Morris, and R. Kumar-Singh (2004). *Adenovirus type 5 pseudotyped with adenovirus type 37 fiber uses sialic acid as a cellular receptor*. Virology, 324(1):129–139. ISSN 00426822. doi:10.1016/j.virol.2004.04.001

[161] T. Angata and A. Varki (2002). *Chemical Diversity in the Sialic Acids and Related α-Keto Acids: An Evolutionary Perspective*. Chemical Reviews, 102(2):439–470. ISSN 0009-2665. doi:10.1021/cr000407m

[162] A. Varki (2007). *Glycan-based interactions involving vertebrate sialic-acid-recognizing proteins*. doi:10.1038/nature05816

[163] A. T. Baker, R. M. Mundy, J. A. Davies, P. J. Rizkallah, and A. L. Parker (2019). *Human adenovirus type 26 uses sialic acid-bearing glycans as a primary cell entry receptor*. Science Advances,

5(9):eaax3567. ISSN 23752548. doi:10.1126/sciadv.aax3567

[164] W. P. Burmeister, D. Guilligay, S. Cusack, G. Wadell, and N. Arnberg (2004). *Crystal structure of species D adenovirus fiber knobs and their sialic acid binding sites.* Journal of virology, 78(14):7727–36. ISSN 0022-538X. doi:10.1128/JVI.78.14.7727-7736.2004

[165] N. H. Rustmeier, M. Strebl, and T. Stehle (2019). *The Symmetry of Viral Sialic Acid Binding Sites-Implications for Antiviral Strategies.* Viruses, 11(10):947. ISSN 1999-4915. doi:10.3390/v11100947

[166] A. Lenman, A. M. Liaci, Y. Liu, L. Frängsmyr, M. Frank, B. S. Blaum, W. Chai, I. I. Podgorski, B. Harrach, M. Benkő, et al. (2018). *Polysialic acid is a cellular receptor for human adenovirus 52.* Proceedings of the National Academy of Sciences of the United States of America, 115(18):E4264–E4273. ISSN 1091-6490. doi:10.1073/pnas.1716900115

[167] E. C. Nilsson, R. J. Storm, J. Bauer, S. M. C. Johansson, A. Lookene, J. Ångström, M. Hedenström, T. L. Eriksson, L. Frängsmyr, S. Rinaldi, et al. (2011). *The GD1a glycan is a cellular receptor for adenoviruses causing epidemic keratoconjunctivitis.* Nature medicine, 17(1):105–9. ISSN 1546-170X. doi:10.1038/nm.2267

[168] P. I. Kitov, J. M. Sadowska, G. Mulvey, G. D. Armstrong, H. Ling, N. S. Pannu, R. J. Read, and D. R. Bundle (2000). *Shiga-like toxins are neutralized by tailored multivalent carbohydrate ligands.* Nature, 403(6770):669–72. ISSN 0028-0836. doi:10.1038/35001095

[169] S. Spjut, W. Qian, J. Bauer, R. Storm, L. Frängsmyr, T. Stehle, N. Arnberg, and M. Elofsson (2011). *A potent trivalent sialic acid inhibitor of adenovirus type 37 infection of human corneal cells.* Angewandte Chemie (International ed. in English), 50(29):6519–21. ISSN 1521-3773. doi:10.1002/anie.201101559

[170] R. Caraballo, M. Saleeb, J. Bauer, A. M. Liaci, N. Chandra, R. J. Storm, L. Frängsmyr, W. Qian, T. Stehle, N. Arnberg, et al. (2015). *Triazole linker-based trivalent sialic acid inhibitors of adenovirus type 37 infection of human corneal epithelial cells.* Organic and Biomolecular Chemistry, 13(35):9194–205. ISSN 1477-0539. doi:10.1039/c5ob01025j

[171] M. Baier, N. H. Rustmeier, J. Harr, N. Cyrus, G. J. Reiss, A. Grafmüller, B. S. Blaum, T. Stehle, and L. Hartmann (2019). *Divalent Sialylated Precision Glycooligomers Binding to Polyomaviruses and the Effect of Different Linkers*. Macromolecular Bioscience, 19(5):e1800426. ISSN 16165195. doi:10.1002/mabi.201800426

[172] E. Johansson, R. Caraballo, N. Mistry, G. Zocher, W. Qian, C. D. Andersson, D. L. Hurdiss, N. Chandra, R. Thompson, L. Frängsmyr, et al. (2020). *Pentavalent Sialic Acid Conjugates Block Coxsackievirus A24 Variant and Human Adenovirus Type 37-Viruses That Cause Highly Contagious Eye Infections*. ACS Chemical Biology, 15(10):2683–2691. ISSN 15548937. doi:10.1021/acschembio.0c00446

[173] A. E. Prota, J. A. Campbell, P. Schelling, J. C. Forrest, M. J. Watson, T. R. Peters, M. Aurrand-Lions, B. A. Imhof, T. S. Dermody, and T. Stehle (2003). *Crystal structure of human junctional adhesion molecule 1: Implications for reovirus binding*. Proceedings of the National Academy of Sciences of the United States of America, 100(9):5366–5371. ISSN 00278424. doi:10.1073/pnas.0937718100

[174] S. Stelzer, K. Ebnet, and J. C. Schwamborn (2010). *JAM-A is a novel surface marker for NG2-Glia in the adult mouse brain*. BMC Neuroscience, 11. ISSN 14712202. doi:10.1186/1471-2202-11-27

[175] I. Hwang, B. S. An, H. Yang, H. S. Kang, E. M. Jung, and E. B. Jeung (2013). *Tissue-specific expression of occludin, Zona occludens-1, and junction adhesion molecule a in the duodenum, ielum, colon, kidney, liver, lung, brain, and skeletal muscle of C57BL mice*. Journal of Physiology and Pharmacology, 64(1):11–18. ISSN 08675910

[176] C. Weber, L. Fraemohs, and E. Dejana (2007). *The role of junctional adhesion molecules in vascular inflammation*. doi:10.1038/nri2096. `https://pubmed.ncbi.nlm.nih.gov/17525755/https://pubmed.ncbi.nlm.nih.gov/17525755/?dopt=Abstract`

[177] T. Stehle and T. S. Dermody (2004). *Structural similarities in the cellular receptors used by*

adenovirus and reovirus. Viral Immunology, 17(2):129–143. ISSN 08828245. doi:10.1089/0882824041310621

[178] J. A. Campbell, P. Schelling, J. D. Wetzel, E. M. Johnson, J. C. Forrest, G. A. R. Wilson, M. Aurrand-Lions, B. A. Imhof, T. Stehle, and T. S. Dermody (2005). *Junctional Adhesion Molecule A Serves as a Receptor for Prototype and Field-Isolate Strains of Mammalian Reovirus*. Journal of Virology, 79(13):7967–7978. ISSN 0022-538X. doi:10.1128/jvi.79.13.7967-7978.2005

[179] E. Kirchner, K. M. Guglielmi, H. M. Strauss, T. S. Dermody, and T. Stehle (2008). *Structure of reovirus $\sigma 1$ in complex with its receptor junctional adhesion molecule-A*. PLoS Pathogens, 4(12):e1000235. ISSN 15537366. doi:10.1371/journal.ppat.1000235

[180] E. Stettner, M. H. Dietrich, K. Reiss, T. S. Dermody, and T. Stehle (2015). *Structure of Serotype 1 Reovirus Attachment Protein $\sigma 1$ in Complex with Junctional Adhesion Molecule A Reveals a Conserved Serotype-Independent Binding Epitope*. Journal of Virology, 89(11):6136–6140. ISSN 0022-538X. doi:10.1128/jvi.00433-15

[181] A. A. Antar, J. L. Konopka, J. A. Campbell, R. A. Henry, A. L. Perdigoto, B. D. Carter, A. Pozzi, T. W. Abel, and T. S. Dermody (2009). *Junctional Adhesion Molecule-A Is Required for Hematogenous Dissemination of Reovirus*. Cell Host and Microbe, 5(1):59–71. ISSN 19313128. doi:10.1016/j.chom.2008.12.001

[182] R. W. Paul, A. H. Choi, and P. W. Lee (1989). *The α-anomeric form of sialic acid is the minimal receptor determinant recognized by reovirus*. Virology, 172(1):382–385. ISSN 10960341. doi:10.1016/0042-6822(89)90146-3

[183] T. S. Dermody, M. L. Nibert, R. Bassel-Duby, and B. N. Fields (1990). *A sigma 1 region important for hemagglutination by serotype 3 reovirus strains*. Journal of Virology, 64(10):5173–5176. ISSN 0022-538X. doi:10.1128/jvi.64.10.5173-5176.1990

[184] J. D. Chappell, V. L. Gunn, J. D. Wetzel, G. S. Baer, and T. S. Dermody (1997). *Mutations in type 3 reovirus that determine binding to sialic acid are contained in the fibrous tail domain of viral attachment protein sigma1*. Journal of Virology, 71(3):1834–1841. ISSN 0022-538X. doi:10.1128/jvi.71.3.1834-1841.1997

[185] D. M. Reiter, J. M. Frierson, E. E. Halvorson, T. Kobayashi, T. S. Dermody, and T. Stehle (2011). *Crystal structure of reovirus attachment protein $\sigma 1$ in complex with sialylated oligosaccharides.* PLoS pathogens, 7(8):e1002166. ISSN 1553-7374. doi:10.1371/journal.ppat.1002166

[186] K. Reiss, J. E. Stencel, Y. Liu, B. S. Blaum, D. M. Reiter, T. Feizi, T. S. Dermody, and T. Stehle (2012). *The GM2 Glycan Serves as a Functional Coreceptor for Serotype 1 Reovirus*. PLoS Pathogens, 8(12):e1003078. ISSN 15537366. doi:10.1371/journal.ppat.1003078

[187] J. L. Konopka-Anstadt, B. A. Mainou, D. M. Sutherland, Y. Sekine, S. M. Strittmatter, and T. S. Dermody (2014). *The Nogo receptor NgR1 mediates infection by mammalian reovirus*. Cell Host and Microbe, 15(6):681–691. ISSN 19346069. doi:10.1016/j.chom.2014.05.010

[188] B. Barrette, N. Vallières, M. Dubé, and S. Lacroix (2007). *Expression profile of receptors for myelin-associated inhibitors of axonal regeneration in the intact and injured mouse central nervous system*. Molecular and Cellular Neuroscience, 34(4):519–538. ISSN 10447431. doi:10.1016/j.mcn.2006.12.004

[189] D. Hunt, R. S. Coffin, and P. N. Anderson (2002). *The Nogo receptor, its ligands and axonal regeneration in the spinal cord; a review.* Journal of neurocytology, 31(2):93–120. ISSN 0300-4864. doi:10.1023/a:1023941421781

[190] T. GrandPré, F. Nakamura, T. Vartanlan, and S. M. Strittmatter (2000). *Identification of the Nogo inhibitor of axon regeneration as a Reticulon protein*. Nature, 403(6768):439–444. ISSN 00280836. doi:10.1038/35000226

[191] T. GrandPré, L. I. Shuxin, and S. M. Strittmatter (2002). *Nogo-66 receptor antagonist peptide promotes axonal regeneration*. Nature, 417(6888):547–551. ISSN 00280836. doi:10.1038/417547a

[192] W. A. Barton, B. P. Liu, D. Tzvetkova, P. D. Jeffrey, A. E. Fournier, D. Sah, R. Cate, S. M. Strittmatter, and D. B. Nikolov (2003). *Structure and axon outgrowth inhibitor binding of the*

Nogo-66 receptor and related proteins. EMBO Journal, 22(13):3291–3302. ISSN 02614189. doi: 10.1093/emboj/cdg325

[193] X. L. He, J. F. Bazan, G. McDermott, J. B. Park, K. Wang, M. Tessier-Lavigne, Z. He, and K. C. Garcia (2003). *Structure of the Nogo receptor ectodomain: A recognition module implicated in myelin inhibition*. Neuron, 38(2):177–185. ISSN 08966273. doi:10.1016/S0896-6273(03)00232-0

[194] J. Laurén, F. Hu, J. Chin, J. Liao, M. S. Airaksinen, and S. M. Strittmatter (2007). *Characterization of myelin ligand complexes with neuronal Nogo-66 receptor family members*. Journal of Biological Chemistry, 282(8):5715–5725. ISSN 00219258. doi:10.1074/jbc.M609797200

[195] B. Rupp (2010). *Biomolecular crystallography : principles, practice, and application to structural biology*. Garland Science. ISBN 978-0815340812

[196] A. Doerr (2016). *Single-particle cryo-electron microscopy*. Nature methods, 13(1):23. ISSN 15487105. doi:10.1038/nmeth.3700

[197] Y. Cheng, N. Grigorieff, P. A. Penczek, and T. Walz (2015). *A primer to single-particle cryo-electron microscopy*. Cell, 161(3):438–449. ISSN 10974172. doi:10.1016/j.cell.2015.03.050

[198] *Getting Started in Cryo-EM with Professor Grant Jensen - YouTube*. `https://www.youtube.com/watch?v=gDgFbAqdM_c&list=PL8_xPU5epJdctoHdQjpfHmd_z9WvGxK8-` (Accessed: 2021-12-07)

[199] X. Fan, J. Wang, X. Zhang, Z. Yang, J. C. Zhang, L. Zhao, H. L. Peng, J. Lei, and H. W. Wang (2019). *Single particle cryo-EM reconstruction of 52 kDa streptavidin at 3.2 Angstrom resolution*. Nature Communications, 10(1):1–11. ISSN 20411723. doi:10.1038/s41467-019-10368-w

[200] X. Wu and T. A. Rapoport (2021). *Cryo-EM structure determination of small proteins by nanobody-binding scaffolds (Legobodies)*. Proceedings of the National Academy of Sciences of the United States of America, 118(41). ISSN 10916490. doi:10.1073/pnas.2115001118

[201] Y. Liu, D. T. Huynh, and T. O. Yeates (2019). *A 3.8 Å resolution cryo-EM structure of a small protein bound to an imaging scaffold*. Nature Communications, 10(1):1–7. ISSN 20411723. doi: 10.1038/s41467-019-09836-0

[202] (2021). *RCSB PDB: Search*. `https://www.rcsb.org/search?request=%7B%22query%22%3A%7B%22type%22%3A%22group%22%2C%22nodes%22%3A%5B%7B%22type%22%3A%22group%22%2C%22nodes%22%3A%5B%7B%22type%22%3A%22terminal%22%2C%22service%22%3A%22text%22%2C%22parameters%22%3A%7B%22attribute%22%3A%22rcs` (Accessed: 2022-03-24)

[203] (2021). *RCSB PDB: Search*. `https://www.rcsb.org/search?request=%7B%22query%22%3A%7B%22type%22%3A%22group%22%2C%22nodes%22%3A%5B%7B%22type%22%3A%22group%22%2C%22nodes%22%3A%5B%7B%22type%22%3A%22terminal%22%2C%22service%22%3A%22text%22%2C%22parameters%22%3A%7B%22attribute%22%3A%22rcs` (Accessed: 2022-03-24)

[204] A. Schmidt, M. Teeter, E. Weckert, and V. S. Lamzin (2011). *Crystal structure of small protein crambin at 0.48 Å resolution*. Acta Crystallographica Section F: Structural Biology and Crystallization Communications, 67(4):424–428. ISSN 17443091. doi:10.1107/S1744309110052607

[205] T. Nakane, A. Kotecha, A. Sente, G. McMullan, S. Masiulis, P. M. Brown, I. T. Grigoras, L. Malinauskaite, T. Malinauskas, J. Miehling, et al. (2020). *Single-particle cryo-EM at atomic resolution*. Nature, 587(7832):152–156. ISSN 14764687. doi:10.1038/s41586-020-2829-0

[206] J. E. Strong, M. C. Coffey, D. Tang, P. Sabinin, and P. W. Lee (1998). *The molecular basis of viral oncolysis: Usurpation of the Ras signaling pathway by reovirus*. EMBO Journal, 17(12):3351–3362. ISSN 02614189. doi:10.1093/emboj/17.12.3351

[207] R. Chakrabarty, H. Tran, G. Selvaggi, A. Hagerman, B. Thompson, and M. Coffey (2015). *The oncolytic virus, pelareorep, as a novel anticancer agent: A review*. Investigational New Drugs, 33(3):761–774. ISSN 15730646. doi:10.1007/s10637-015-0216-8

[208] M. P. Lolkema, H. T. Arkenau, K. Harrington, P. Roxburgh, R. Morrison, V. Roulstone, K. Twigger, M. Coffey, K. Mettinger, G. Gill, et al. (2011). *A phase I study of the combination of intravenous*

reovirus type 3 dearing and gemcitabine in patients with advanced cancer. Clinical Cancer Research, 17(3):581–588. ISSN 10780432. doi:10.1158/1078-0432.CCR-10-2159

[209] E. Gasteiger, C. Hoogland, A. Gattiker, S. Duvaud, M. R. Wilkins, R. D. Appel, and A. Bairoch (2005). *Protein Identification and Analysis Tools on the ExPASy Server*. In *The Proteomics Protocols Handbook*, pp. 571–607. Humana Press, Totowa, NJ. doi:10.1385/1-59259-890-0:571

[210] J. J. Almagro Armenteros, K. D. Tsirigos, C. K. Sønderby, T. N. Petersen, O. Winther, S. Brunak, G. von Heijne, and H. Nielsen (2019). *SignalP 5.0 improves signal peptide predictions using deep neural networks*. Nature Biotechnology, 37(4):420–423. ISSN 15461696. doi:10.1038/s41587-019-0036-z

[211] F. Sievers, A. Wilm, D. Dineen, T. J. Gibson, K. Karplus, W. Li, R. Lopez, H. McWilliam, M. Remmert, J. Söding, et al. (2011). *Fast, scalable generation of high-quality protein multiple sequence alignments using Clustal Omega*. Molecular Systems Biology, 7(1):539. ISSN 17444292. doi:10.1038/msb.2011.75

[212] F. Madeira, Y. M. Park, J. Lee, N. Buso, T. Gur, N. Madhusoodanan, P. Basutkar, A. R. Tivey, S. C. Potter, R. D. Finn, et al. (2019). *The EMBL-EBI search and sequence analysis tools APIs in 2019*. Nucleic Acids Research, 47(W1):W636–W641. ISSN 13624962. doi:10.1093/nar/gkz268

[213] A. M. Waterhouse, J. B. Procter, D. M. A. Martin, M. Clamp, and G. J. Barton (2009). *Jalview Version 2-A multiple sequence alignment editor and analysis workbench*. Bioinformatics, 25(9):1189–1191. ISSN 13674803. doi:10.1093/bioinformatics/btp033

[214] A. M. Liaci (2017). *Structural and Functional Studies on the Early Steps of Polyomavirus and Adenovirus Life Cycles*. Dissertation, Eberhard Karls Universität Tübingen

[215] T. Hassemer (2013). *Structural Analysis of Human Adenovirus 26 and 48 Fiber Knob and their Interactions with Sialic Acid Ligands*. Diploma thesis, Eberhard Karls Universität Tübingen

[216] W. Kabsch (2010). *XDS*. Acta Crystallographica Section D Biological Crystallography, 66(2):125–132. ISSN 0907-4449. doi:10.1107/S0907444909047337

[217] A. J. McCoy, R. W. Grosse-Kunstleve, P. D. Adams, M. D. Winn, L. C. Storoni, and R. J. Read (2007). *Phaser crystallographic software*. Journal of Applied Crystallography, 40(4):658–674. ISSN 00218898. doi:10.1107/S0021889807021206

[218] M. D. Winn, C. C. Ballard, K. D. Cowtan, E. J. Dodson, P. Emsley, P. R. Evans, R. M. Keegan, E. B. Krissinel, A. G. Leslie, A. McCoy, et al. (2011). *Overview of the CCP4 suite and current developments*. Acta Crystallographica Section D: Biological Crystallography, 67(4):235–242. ISSN 09074449. doi:10.1107/S0907444910045749

[219] P. D. Adams, R. W. Grosse-Kunstleve, L.-W. Hung, T. R. Ioerger, A. J. McCoy, N. W. Moriarty, R. J. Read, J. C. Sacchettini, N. K. Sauter, and T. C. Terwilliger (2002). *PHENIX : building new software for automated crystallographic structure determination*. Acta Crystallographica Section D Biological Crystallography, 58(11):1948–1954. ISSN 0907-4449. doi:10.1107/S0907444902016657

[220] N. Stein (2008). *CHAINSAW : a program for mutating pdb files used as templates in molecular replacement*. Journal of Applied Crystallography, 41(3):641–643. ISSN 0021-8898. doi:10.1107/S0021889808006985

[221] P. Emsley, B. Lohkamp, W. G. Scott, and K. Cowtan (2010). *Features and development of Coot*. Acta Crystallographica Section D: Biological Crystallography, 66(4):486–501. ISSN 09074449. doi:10.1107/S0907444910007493

[222] P. V. Afonine, R. W. Grosse-Kunstleve, N. Echols, J. J. Headd, N. W. Moriarty, M. Mustyakimov, T. C. Terwilliger, A. Urzhumtsev, P. H. Zwart, and P. D. Adams (2012). *Towards automated crystallographic structure refinement with phenix.refine*. Acta Crystallographica Section D: Biological Crystallography, 68(4):352–367. ISSN 09074449. doi:10.1107/S0907444912001308

[223] A. Urzhumtsev, P. V. Afonine, and P. D. Adams (2011). *TLS for dummies*. Computational Crystallography Newsletter, 2(1):42–84

[224] *BKChem*. `https://bkchem.zirael.org/index.html` (Accessed: 2021-09-16)

[225] N. W. Moriarty, R. W. Grosse-Kunstleve, and P. D. Adams (2009). *Electronic ligand builder and optimization workbench (eLBOW): A tool for ligand coordinate and restraint generation*. Acta Crystallographica Section D: Biological Crystallography, 65(10):1074–1080. ISSN 09074449. doi: 10.1107/S0907444909029436

[226] *X-ray Absorption Edges*. `http://skuld.bmsc.washington.edu/scatter/AS_periodic.html` (Accessed: 2021-09-16)

[227] *CAD (CCP4: Supported Program)*. `https://www.ccp4.ac.uk/html/cad.html` (Accessed: 2021-09-16)

[228] R. J. Read and A. J. Schierbeek (1988). *A phased translation function*. Journal of Applied Crystallography, 21(5):490–495. ISSN 0021-8898. doi:10.1107/S002188988800562X

[229] L. Schrödinger (2015). *The PyMOL Molecular Graphics System, Version 1.8*. doi: citeulike-article-id:9562772

[230] N. A. Baker, D. Sept, S. Joseph, M. J. Holst, J. Andrew McCammon, and J. A. McCammon (2001). *Electrostatics of nanosystems: Application to microtubules and the ribosome*. Proceedings of the National Academy of Sciences of the United States of America, 98(18):10037–10041. ISSN 00278424. doi:10.1073/pnas.181342398

[231] D. N. Mastronarde (2005). *Automated electron microscope tomography using robust prediction of specimen movements.* Journal of structural biology, 152(1):36–51. ISSN 1047-8477. doi: 10.1016/j.jsb.2005.07.007

[232] J. R. Kremer, D. N. Mastronarde, and J. McIntosh (1996). *Computer Visualization of Three-Dimensional Image Data Using IMOD*. Journal of Structural Biology, 116(1):71–76. ISSN 10478477. doi:10.1006/jsbi.1996.0013

[233] G. Tang, L. Peng, P. R. Baldwin, D. S. Mann, W. Jiang, I. Rees, and S. J. Ludtke (2007). *EMAN2: An extensible image processing suite for electron microscopy*. Journal of Structural Biology, 157(1):38–46. ISSN 10478477. doi:10.1016/j.jsb.2006.05.009

[234] J. M. Bell, M. Chen, P. R. Baldwin, and S. J. Ludtke (2016). *High resolution single particle refinement in EMAN2.1*. Methods, 100:25–34. ISSN 10959130. doi:10.1016/j.ymeth.2016.02.018

[235] J. M. Bell, M. Chen, T. Durmaz, A. C. Fluty, and S. J. Ludtke (2018). *New software tools in EMAN2 inspired by EMDatabank map challenge*. Journal of Structural Biology, 204(2):283–290. ISSN 10958657. doi:10.1016/j.jsb.2018.09.002

[236] E. F. Pettersen, T. D. Goddard, C. C. Huang, G. S. Couch, D. M. Greenblatt, E. C. Meng, and T. E. Ferrin (2004). *UCSF Chimera - A visualization system for exploratory research and analysis*. Journal of Computational Chemistry, 25(13):1605–1612. ISSN 01928651. doi:10.1002/jcc.20084

[237] K. M. Reinisch, M. L. Nibert, and S. C. Harrison (2000). *Structure of the reovirus core at 3.6 Å resolution*. Nature, 404(6781):960–967. ISSN 00280836. doi:10.1038/35010041

[238] P. V. Afonine, J. J. Headd, T. C. Terwilliger, and P. D. Adams (2013). *PHENIX News - Real space refine*. Computational Crystallography Newsletter, 4:43–44

[239] B. D. Persson, L. John, K. Rafie, M. Strebl, L. Frängsmyr, M. Z. Ballmann, K. Mindler, M. Havenga, A. Lemckert, T. Stehle, et al. (2021). *Human species D adenovirus hexon capsid protein mediates cell entry through a direct interaction with CD46*. Proceedings of the National Academy of Sciences, 118(3):e2020732118. ISSN 0027-8424. doi:10.1073/pnas.2020732118

[240] B. D. Persson, S. Müller, D. M. Reiter, B. B. T. Schmitt, M. Marttila, C. V. Sumowski, S. Schweizer, U. Scheu, C. Ochsenfeld, N. Arnberg, et al. (2009). *An arginine switch in the species B adenovirus knob determines high-affinity engagement of cellular receptor CD46.* Journal of virology, 83(2):673–86. ISSN 1098-5514. doi:10.1128/JVI.01967-08

[241] *Uniprot- Human adenovirus 56 - L5 gene*. `https://www.uniprot.org/uniprot/E1AI37` (Accessed: 2022-03-28)

[242] *Uniprot - Human adenovirus D serotype 9 (HAdV-9) - L5 gene*. `https://www.uniprot.org/uniprot/P68982` (Accessed: 2022-03-28)

[243] R. Yan, Y. Zhang, Y. Li, L. Xia, Y. Guo, and Q. Zhou (2020). *Structural basis for the recognition*

of SARS-CoV-2 by full-length human ACE2. Science, 367(6485):1444–1448. ISSN 10959203. doi:10.1126/science.abb2762

[244] L. J. Ströh, N. H. Rustmeier, B. S. Blaum, J. Botsch, P. Rößler, F. Wedekink, W. Ian Lipkin, N. Mishra, and T. Stehle (2020). *Structural basis and evolution of glycan receptor specificities within the polyomavirus family*. mBio, 11(4):1–21. ISSN 21507511. doi:10.1128/mBio.00745-20

[245] M. De Graaf and R. A. Fouchier (2014). *Role of receptor binding specificity in influenza A virus transmission and pathogenesis*. EMBO Journal, 33(8):823–841. ISSN 14602075. doi:10.1002/embj.201387442

[246] S. Lopez and C. F. Arias (2006). *Early steps in rotavirus cell entry*. doi:10.1007/3-540-30773-7_2

[247] P. R. Dormitzer, Z.-Y. J. Sun, O. Blixt, J. C. Paulson, G. Wagner, and S. C. Harrison (2002). *Specificity and Affinity of Sialic Acid Binding by the Rhesus Rotavirus VP8* Core*. Journal of Virology, 76(20):10512–10517. ISSN 0022-538X. doi:10.1128/jvi.76.20.10512-10517.2002

[248] C. A. Guerrero, D. Bouyssounade, S. Zárate, P. Iša, T. López, R. Espinosa, P. Romero, E. Méndez, S. López, and C. F. Arias (2002). *Heat Shock Cognate Protein 70 Is Involved in Rotavirus Cell Entry*. Journal of Virology, 76(8):4096–4102. ISSN 0022-538X. doi:10.1128/jvi.76.8.4096-4102.2002

[249] S. Zárate, M. A. Cuadras, R. Espinosa, P. Romero, K. O. Juárez, M. Camacho-Nuez, C. F. Arias, and S. López (2003). *Interaction of Rotaviruses with Hsc70 during Cell Entry Is Mediated by VP5*. Journal of Virology, 77(13):7254–7260. ISSN 0022-538X. doi:10.1128/jvi.77.13.7254-7260.2003

[250] X. Jiang, Y. Liu, and M. Tan (2017). *Histo-blood group antigens as receptors for rotavirus, new understanding on rotavirus epidemiology and vaccine strategy*. doi:10.1038/emi.2017.30. `https://www.tandfonline.com/doi/abs/10.1038/emi.2017.30`

[251] H. Li, E. G. Rhee, K. Masek-Hammerman, J. E. Teigler, P. Abbink, and D. H. Barouch (2012). *Adenovirus Serotype 26 Utilizes CD46 as a Primary Cellular Receptor and Only Transiently Activates T Lymphocytes following Vaccination of Rhesus Monkeys*. Journal of Virology, 86(19):10862–10865. ISSN 0022-538X. doi:10.1128/jvi.00928-12

[252] J. R. Hemsath, A. M. Liaci, J. D. Rubin, B. J. Parrett, S.-C. Lu, T. V. Nguyen, M. A. Turner, C. Y. Chen, K. Cupelli, V. S. Reddy, et al. (2021). *Ex Vivo and In Vivo CD46 Receptor Utilization by Species D Human Adenovirus Serotype 26 (HAdV26)*. Journal of Virology. ISSN 0022-538X. doi:10.1128/jvi.00826-21

[253] D. Nestić, T. G. Uil, J. Ma, S. Roy, J. Vellinga, A. H. Baker, J. Custers, and D. Majhen (2019). *$\alpha v\beta 3$ Integrin Is Required for Efficient Infection of Epithelial Cells with Human Adenovirus Type 26*. Journal of Virology, 93(1). ISSN 0022-538X. doi:10.1128/jvi.01474-18

[254] L. Pache, S. Venkataraman, G. R. Nemerow, and V. S. Reddy (2008). *Conservation of fiber structure and CD46 usage by subgroup B2 adenoviruses*. Virology, 375(2):573–579. ISSN 00426822. doi:10.1016/j.virol.2008.02.013

[255] P. Wörz (2019). *Functional Characterization of Reovirus Attachment to the Nogo Receptor NgR1*. Bachelor´s thesis, Eberhard Karls Universität Tübingen

[256] E. L. Nason, J. D. Wetzel, S. K. Mukherjee, E. S. Barton, B. V. V. Prasad, and T. S. Dermody (2001). *A Monoclonal Antibody Specific for Reovirus Outer-Capsid Protein 3 Inhibits 1-Mediated Hemagglutination by Steric Hindrance*. Journal of Virology, 75(14):6625–6634. ISSN 0022-538X. doi:10.1128/jvi.75.14.6625-6634.2001

[257] A. J. Snyder, J. C.-Y. Wang, and P. Danthi (2019). *Components of the Reovirus Capsid Differentially Contribute to Stability*. Journal of Virology, 93(2). ISSN 0022-538X. doi:10.1128/jvi.01894-18

[258] X. Zhang, L. Jin, Q. Fang, W. H. Hui, and Z. H. Zhou (2010). *3.3 Å Cryo-EM structure of a nonenveloped virus reveals a priming mechanism for cell entry*. Cell, 141(3):472–482. ISSN 00928674. doi:10.1016/j.cell.2010.03.041

[259] A. E. Fournier, G. C. Gould, B. P. Liu, and S. M. Strittmatter (2002). *Truncated soluble Nogo receptor binds Nogo-66 and blocks inhibition of axon growth by myelin*. Journal of Neuroscience, 22(20):8876–8883. ISSN 02706474. doi:10.1523/jneurosci.22-20-08876.2002

[260] M. Vinson, O. Rausch, P. R. Maycox, R. K. Prinjha, D. Chapman, R. Morrow, A. J. Harper, C. Dingwall, F. S. Walsh, S. A. Burbidge, et al. (2003). *Lipid rafts mediate the interaction between myelin-associated glycoprotein (MAG) on myelin and MAG-receptors on neurons*. Molecular and Cellular Neuroscience, 22(3):344–352. ISSN 10447431. doi:10.1016/S1044-7431(02)00031-3

[261] W. Yu, W. Guo, and L. Feng (2004). *Segregation of Nogo66 receptors into lipid rafts in rat brain and inhibition of Nogo66 signaling by cholesterol depletion*. FEBS Letters, 577(1-2):87–92. ISSN 00145793. doi:10.1016/j.febslet.2004.09.068

List of Tables

1 **Baltimore classification of viruses** 4
2 **Human adenovirus types** 4
3 **List of plasmids** 28
4 **Pipetting scheme and PCR program for bacmid PCR** 34
5 **Pipetting schemes for SDS-PAGE gels and 4x Protein Sample Buffer.** 34
6 **Preparative size exclusion chromatography overview** 39
7 **Analytical size exclusion chromatography overview** 40
8 **Data processing and refinement statistics of HAdV56 FK structures** 49
S1 **Data processing and refinement statistics of HAdV37-inhibitor structures** 123
S2 **Data processing and refinement statistics of HAdV36-inhibitor structures** 124
S3 **Data processing and refinement statistics of HAdV26-inhibitor structures** 125

List of Figures

1 **Overview of ReoV and HAdV capsid structure** 6
2 **Overview of HAdV FK receptor binding sites** 13
3 **Structure of 2nd generation compound ME0462** 15
4 **Overview of ReoV receptor binding sites** 16
5 **Crystal structure of NgR1** 17
6 **Ewald sphere** 19
7 **CryoEM workflow** 21
8 **Purification of HAdV56 FK** 48
9 **Crystallization of HAdV56 FK** 48
10 **Sequence alignment and structural superposition of the loops involved in CD46 binding at HAdV11, HAdV7 and HAdV56** 50
11 **Sequence alignment and surface charge analysis** 51
12 **Structural superposition of sialic acid binding sites of HAdV56 and HAdV37** 52
13 **SPR Analysis and Transduction Assays Confirming CD46 Interaction With HAdV56 Hexon** 54
14 **3rd generation of trivalent sialic acid inhibitors** 57
15 **Representative crystals of HAdV37-, HAdV36-, and HAdV26-inhibitor complexes** 58
16 **Difference electron density maps and intermolecular interactions of ME1123 in complex with HAdV37, HAdV36, and HAdV26** 60
17 **Difference electron density maps and intermolecular interactions of ME1145 in complex with HAdV37, HAdV36, and HAdV26** 62
18 **Sialic acid ring shifts at the binding site** 63
19 **Zinc binding of ME1146** 65
20 **Biological evaluation of inhibitors using A549 cells** 67
21 **Purification of His-tagged NgR1** 72

22 **Purification of Fc-tagged NgR1** . . . 72
23 **Glycosylation analysis of NgR1** . . . 73
24 **Expression and purification of $\mu 1_3\sigma 3_3$** . . . 74
25 **Analytical SEC chromatograms of $\mu 1_3\sigma 3_3$ and NgR1** complex assays 75
26 **Pulldown assays** . . . 77
27 **Crosslinking Assays** . . . 78
28 **SPR analysis** . . . 79
29 **CryoEM data processing** . . . 81
30 **FSC of unliganded and NgR1-liganded reovirus reconstructions** . . 82
31 **CryoEM reconstruction of unliganded and NgR1-liganded reovirus virions** . . . 83
32 **NgR1 binding mode and interaction with $\sigma 3$** . . . 85
33 **Surface charge analysis of concave interface** . . . 91
34 **NgR1 mutagenesis studies** . . . 92
S1 **Purification of HAdV37** . . . 121
S2 **Purification of HAdV26** . . . 121
S3 **Purification of HAdV36** . . . 121
S4 **Simulated annealing omit difference electron density maps of all inhibitors in complex with HAdV37, HAdV36, and HAdV26** . . . 122
S5 **Difference electron density maps and intermolecular interactions of ME1146 in complex with HAdV37, HAdV36, and HAdV26** . . . 126
S6 **Difference electron density maps and intermolecular interactions of ME1015 in complex with HAdV37, HAdV36, and HAdV26** . . . 127
S7 **Pulldown assay negative control** . . . 127
S8 **SPR analysis using NTA Sensor Chip** . . . 128

Acknowledgments

Viele Menschen haben mich in den letzten Jahren inner- und auch ausserhalb des Labors unterstützt, in großen wie in kleinen Dingen. Es ist nicht leicht, dafür angemesse Worte zu finden, dennoch möchte auf diesem Wege meinen Dank aussprechen an:

- Thilo, für die immer vertrauensvolle und fruchtbare Zusammenarbeit. Ich hatte vollste Unterstützung wenn nötig und großen Freiraum wann immer möglich, was mich zu dem Wissenschaftler hat wachsen lassen, der ich jetzt bin.

- Prof. Dirk Schwarzer für die spontane Bereitschaft als Zweitgutacher.

- Prof. Niklas Arnberg for a great collaboration on several adenovirus projects and for being my supervisor and examiner at my PhD defense.

- Team Reovirus from Pittsburgh, especially Prof. Terry Dermody and Dr. Danica Sutherland for a wonderful collaboration, exciting discussions and very educational as well as entertaining phonecalls.

- meinen beiden Studenten Katja (die mittlerweile meine Kollegin ist, was mich besonders stolz macht) und Patrick. Durch euch habe ich wahrscheinlich ebenso viel gelernt, wie ihr hoffentlich auch von mir.

- dem gesamten AK Stehle für die vergangenen Jahre. Es war mir eine Freude, von euch zu lernen und mit euch zusammenzuarbeiten. Allen voran Niklas, der mich in die Welt von Linux und in die Kristallographie eingeführt hat, mir stets mit Rat und Tat zur Seite stand (auch ausserhalb des Labors), und bei dem ich mich dafür mit kulinarischen Ratschlägen aller Art revanchieren konnte. Daneben vielen weiteren Mitarbeitern des AK Stehle, besonders Georg (vor allem für jeglichen

Server-Support), Christoph (für das am Leben erhalten vieler Geräte), Aleks (for proofreading this thesis), Elena (für Schreibmotivation) und dem Roboter-Team um Elena, Irmi, Katja und Nina. Des weiteren Bärbel, Christina, Glencora, Jasmin, Joana, Marie, Micha, Natascha, Nils, Simon, und Yinglan für die stets fröhliche und konstruktive Zusammenarbeit.

- ein riesengroßer Dank gilt meinen Eltern für die bedingungslose Unterstützung mein Leben lang, ohne die ich heute nicht hier wäre.

- der größte Dank gilt schlussendlich meiner Johanna. Einfach für alles. Und für immer. Ich liebe dich!

Appendix

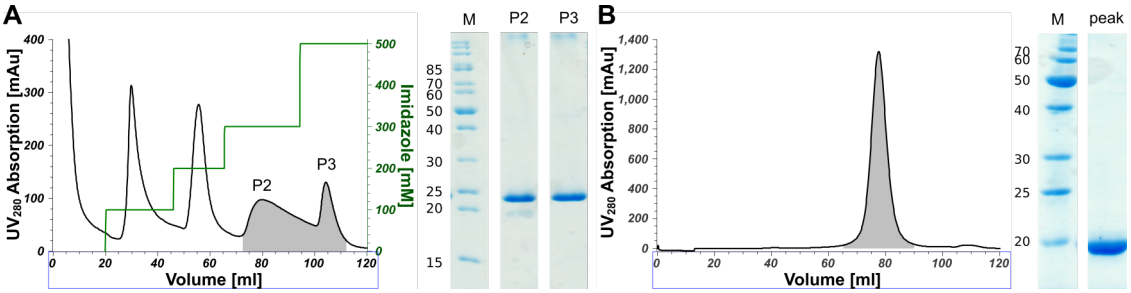

Figure S1) **Purification of HAdV37. A:** IMAC chromatogram of HAdV37 FK purification showing two peaks at 200 mM and 300 mM imidiazole, respectively, that reveal a single band at 24 kDa at SDS-PAGE analysis. **B:** SEC chromatogram of HAdV37 FK purification showing a single peak and SDS-PAGE reveals a single, pure band at 20 kDa after cleavage of the His-tag.

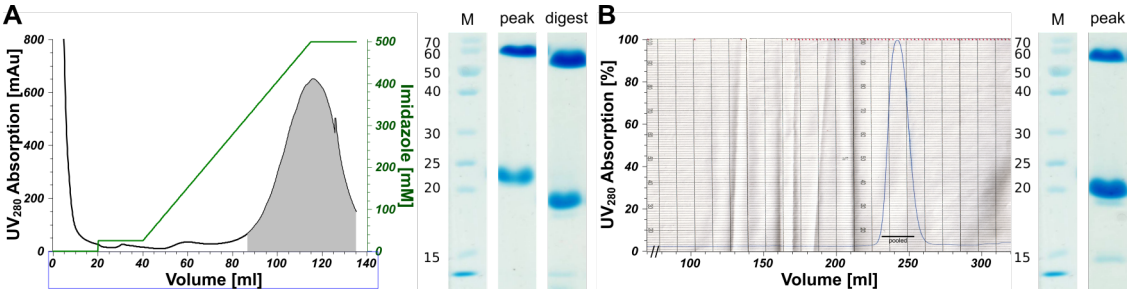

Figure S2) **Purification of HAdV26. A:** IMAC chromatogram of HAdV26 FK purification showing a single peak, which is analyzed by SDS-PAGE before (peak) and after cleavage (digest) of the His-tag, revealing bands for the HAdV26 monomer (24 kDa before cleavage, 21 kDa afterwards) and the trimer (approx. 60 kDa). **B:** SEC chromatogram of HAdV26 FK purification showing a sharp peak and similar bands at the SDS-PAGE analysis for the monomeric and trimeric state of HAdV26.

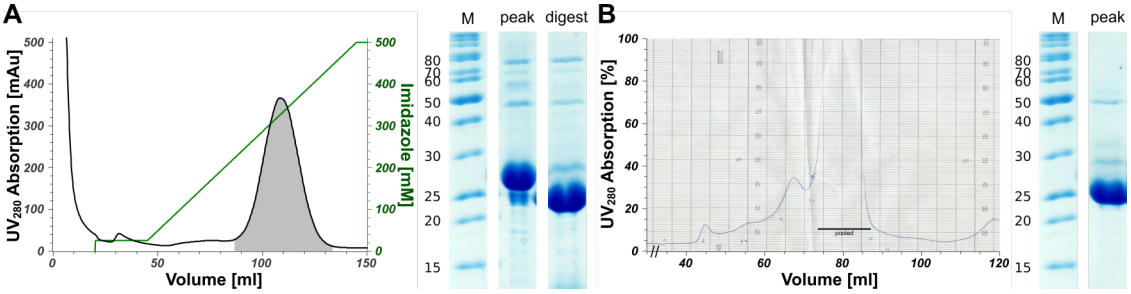

Figure S3) **Purification of HAdV36. A:** IMAC chromatogram of HAdV36 FK purification showing a single peak, which is analyzed by SDS-PAGE before (peak) and after cleavage (digest) of the His-tag, revealing bands for the HAdV36 monomer (26 kDa before cleavage, 23 kDa afterwards) and minor impurities. **B:** SEC chromatogram of HAdV36 FK purification showing a small, high molecular weight peak, corresponding to the 75 kDa impurity of the IMAC and a larger second peak, which corresponds to HAdV36 as confirmed by SDS-PAGE analysis.

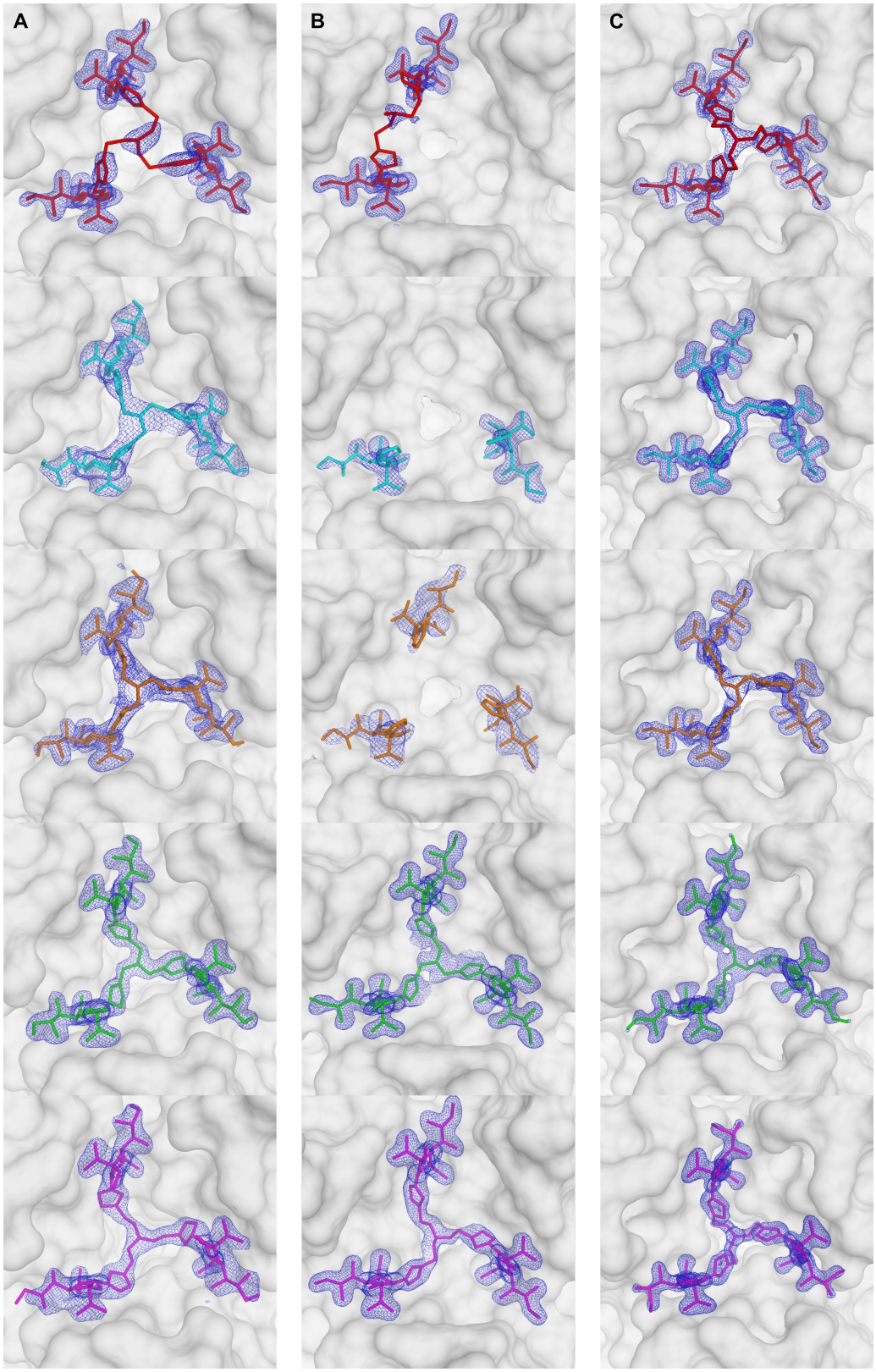

Figure S4) Simulated annealing omit difference electron density maps of ME0462 (red), ME1123 (cyan), ME1146 (orange), ME1015 (green), and ME1145 (magenta) in complex with each HAdV37 (A), HAdV36 (B), and HAdV26 (C). Simulated Annealing omit difference electron density maps depicted as blue meshes at a level of 3 σ and a radius of 1.6 Å around the ligand.

Table S1) Data processing and refinement statistics of HAdV37-inhibitor structures.

	HAdV37 FK +ME1123	HAdV37 FK +ME1146	HAdV37 FK +ME1015	HAdV37 FK +ME1145
Data Processing				
Space Group	P 1 21 1	P 1 21 1	P 1 21 1	P 1 21 1
Cell Dimensions				
a, b, c	60.4, 69.5, 74.5	60.9, 69.5, 74.4	60.0, 69.0, 74.3	61.0, 69.5, 74.4
α, β, γ	90.0, 94.7, 90.0	90.0, 94.3, 90.0	90.0, 94.3, 90.0	90.0, 94.5, 90.0
Resolution bin (last bin) [Å]	45.50–2.05 (2.17–2.05)	48.79–1.56 (1.65–1.56)	48.34–1.54 (1.60–1.54)	45.77–1.60 (1.69–1.60)
Reflections overall	262,443	421,078	603,719	408,778
Reflections unique	38413 (6112)	85149 (14056)	87986 (89030)	81172 (13052)
Redundancy	6.8 (6.8)	4.9 (5.1)	6.9 (7.0)	5.0 (5.0)
Completeness [%]	99.8 (98.9)	97.0 (99.5)	98.8 (97.6)	99.8 (99.4)
I/σ [I]	16.61 (1.31)	15.33 (1.20)	10.70 (1.93)	15.1 (1.18)
R_{meas}	9.1 (156.2)	6.7 (135.9)	10.1 (85.0)	6.3 (130.5)
$CC_{1/2}$	99.9 (61.8)	99.9 (51.5)	99.6 (84.4)	99.9 (52.7)
Wilson B [$Å^2$]	49.7	29.5	29.9	32
Refinement				
No. of atoms total	4,272	4,984	4,888	5,027
protein	4,052	4,383	4,336	4,476
ligand	79	82	82	85
solvent	141	519	470	466
R_{work} / R_{free} [%]	19.0/22.3	19.6/21.5	13.6 / 17.3	14.3/18.9
r.m.s.d bond [Å]	0.01	0.011	0.008	0.01
r.m.s.d angle [°]	1.04	1.19	1.18	1.23
B factor overall [$Å^2$]	58.85	30.28	30.1	32.1
protein	59.23	29.25	28.7	30.6
ligand	50.14	29.97	31.2	42.6
solvent	52.6	39	43.4	43.8
Ramachandran [%]				
favored	94.9	96.7	96.47	96.52
allowed	5.1	3.11	3.53	3.48
outlier	0	0.18	0	0

Table S2) Data processing and refinement statistics of HAdV36-inhibitor structures.

	HAdV36 FK +ME0462	HAdV36 FK +ME1123	HAdV36 FK +ME1146	HAdV36 FK +ME1015	HAdV36 FK +ME1145
Data Processing					
Space Group	P 21 21 2	P 21 21 21	P 21 21 21	P 21 21 21	P 21 21 21
Cell Dimensions					
a, b, c	99.5, 88.6, 58.7	55.4, 100.5, 102.5	55.3, 100.4, 102.5	59.6, 102.0, 111.2	59.2, 100.6, 111.0
α, β, γ	90.0, 90.0, 90.0	90.0, 90.0, 90.0	90.0, 90.0, 90.0	90.0, 90.0, 90.0	90.0, 90.0, 90.0
Resolution bin (last bin) [Å]	48.92–1.25 (1.34–1.25)	37.61–1.80 (1.84–1.80)	48.66–2.30 (2.35–2.30)	48.82–1.32 (1.39–1.32)	48.58–1.50 (1.53–1.50)
Reflections overall	921,509	837,022	419,095	2,043,334	1,598,589
Reflections unique	143686 (22806)	53644 (3942)	26020 (1859)	158917 (25460)	106794 (7674)
Redundancy	6.4 (6.1)	15.6 (8.4)	16.1 (16.1)	12.8 (11.4)	15.0 (12.2)
Completeness [%]	99.8 (98.9)	100.0 (99.8)	99.9 (99.3)	100.0 (99.9)	99.7 (97.8)
I/σ [I]	15.91 (1.42)	14.75 (0.99)	9.78 (1.34)	14.68 (1.69)	21.12 (1.65)
R_{meas}	6.0 (129.6)	14.1 (212.5)	26.7 (239.7)	9.1 (125.9)	8.0 (176.2)
$CC_{1/2}$	99.9 (61.6)	99.9 (47.0)	99.7 (59.0)	99.9 (73.2)	100.0 (60.4)
Wilson B [$Å^2$]	19.6	34.7	49.1	22.7	26.5
Refinement					
No. of atoms total	5,068	4,559	4,353	5,469	5,152
protein	4,486	4,258	4,217	4,469	4,488
ligand	60	50	75	164	85
solvent	522	251	61	836	579
R_{work} / R_{free} [%]	14.3/17.3	17.2/20.4	19.2/23.9	13.2/15.5	13.2/17.1
r.m.s.d bond [Å]	0.01	0.011	0.004	0.011	0.013
r.m.s.d angle [°]	1.24	1.14	0.73	1.5	1.43
B factor overall [$Å^2$]	21.8	36.8	52.8	23.5	26.8
protein	20	36.2	52.6	20.5	24.8
ligand	29.2	53.2	73.3	16.7	25
solvent	36.4	43.6	47.6	40.6	42.7
Ramachandran [%]					
favored	96.89	96.99	91.07	97.77	97.09
allowed	3.11	3.01	2.8	2.23	2.91
outlier	0	0	0.19	0	0

Table S3) Data processing and refinement statistics of HAdV26-inhibitor structures.

	HAdV26 FK +ME0462	HAdV26 FK +ME1123	HAdV26 FK +ME1146	HAdV26 FK +ME1015	HAdV26 FK +ME1145
Data Processing					
Space Group	P 21 3	P 21 3	P 21 3	P 21 3	P 21 3
Cell Dimensions					
a, b, c	86.1, 86.1, 86.1	85.9, 85.9, 85.9	85.9, 85.9, 85.9	85.8, 85.8, 85.8	86.0, 86.0, 86.0
α, β, γ	90.0, 90.0, 90.0	90.0, 90.0, 90.0	90.0, 90.0, 90.0	90.0, 90.0, 90,0	90.0, 90.0, 90,0
Resolution bin (last bin) [Å]	43.07–1.65 (1.74–1.65)	49.60–1.21 (1.27–1.21)	42.95–1.40 (1.48–1.40)	49.53–1.10 (1.16–1.10)	43.01–1.19 (1.25–1.19)
Reflections overall	589,451	1,688,846	999,408	2,169,451	1,487,984
Reflections unique	23026 (4135)	64427 (10131)	41737 (6663)	85116 (13630)	68468 (10979)
Redundancy	25.6 (25.9)	26.1 (25.3)	23.9 (21.5)	25.5 (22.4)	21.7 (21.4)
Completeness [%]	89.2 (100.0)	100.0 (100.0)	99.9 (99.5)	100.0 (99.9)	99.9 (99.9)
I/σ [I]	16.81 (2.25)	20.87 (2.20)	17.93 (2.07)	15.81 (1.37)	21.85 (1.71)
R_{meas}	19.2 (159.3)	9.8 (151.9)	19.5 (202.9)	14.5 (227.8)	7.9 (192.8)
$CC_{1/2}$	99.8 (77.5)	100.0 (73.4)	99.9 (71.9)	99.9 (58.4)	100.0 (64.9)
Wilson B [$Å^2$]	21	18.1	21.6	14.6	19.2
Refinement					
No. of atoms total	1,509	1,668	1,584	1,750	1,594
protein	1,345	1,423	1,356	1,475	1,420
ligand	30	27	28	28	29
solvent	134	218	200	247	145
R_{work} / R_{free} [%]	19.5/23.2	14.4/16.4	13.9/16.7	14.5/15.4	15.3/16.8
r.m.s.d bond [Å]	0.011	0.011	0.01	0.015	0.009
r.m.s.d angle [°]	1.14	1.35	1.27	1.56	1.26
B factor overall [$Å^2$]	22.7	23.2	21	21.2	23.6
protein	21.8	20.6	18.7	17.8	21.9
ligand	24.7	13.19	19.8	20.6	23.8
solvent	30.8	41.4	37	41.4	39.6
Ramachandran [%]					
favored	95.06	93.94	93.87	92.93	95.32
allowed	4.94	6.06	6.13	7.07	4.68
outlier	0	0	0	0	0

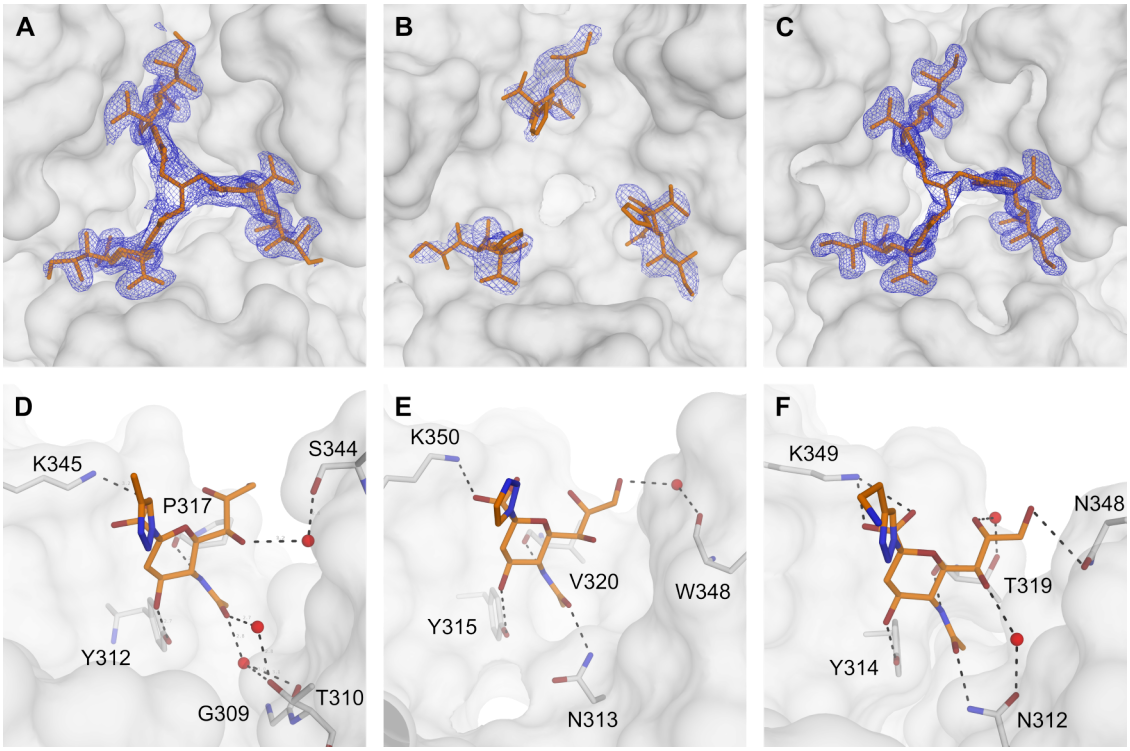

Figure S5) **Difference electron density maps and intermolecular interactions of ME1146 in complex with HAdV37 (A,D), HAdV36 (B,E), and HAdV26 (C,F). A–C:** Simulated annealing omit difference electron density maps depicted as blue meshes at a level of 3 σ and a radius of 1.6 Å around the ligand. **D–F:** Water molecules are displayed as red spheres, hydrogen bonds as black dashed lines.

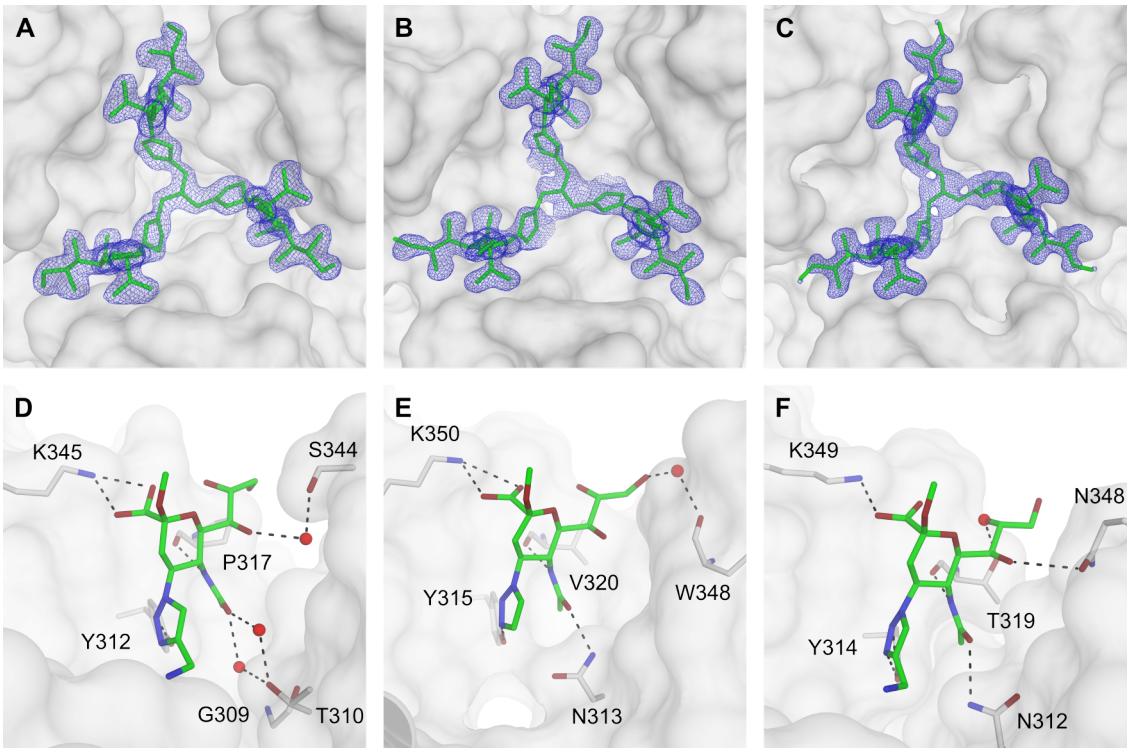

Figure S6) **Difference electron density maps and intermolecular interactions of ME1015 in complex with HAdV37 (A,D), HAdV36 (B,E), and HAdV26 (C,F). A–C:** Simulated annealing omit difference electron density maps depicted as blue meshes at a level of 3 σ and a radius of 1.6 Å around the ligand. **D–F:** Water molecules are displayed as red spheres, hydrogen bonds as black dashed lines.

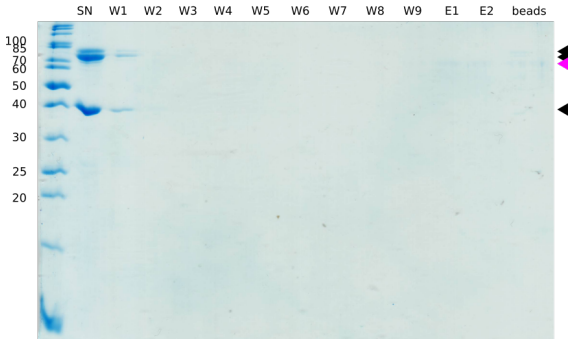

Figure S7) **Pulldown assay negative control.** Pulldown assay using Protein A beads without NgR1-Fc reveals no bands at the expected molecular weight for $\mu 1_3 \sigma 3_3$ (black arrowheads) or NgR1-Fc (magenta arrowheads) at SDS-PAGE analysis. SN = supernatant after incubation; WX = washing step X; EX = elution step X; beads = Protein A/G UltraLink™ Resin after elution.

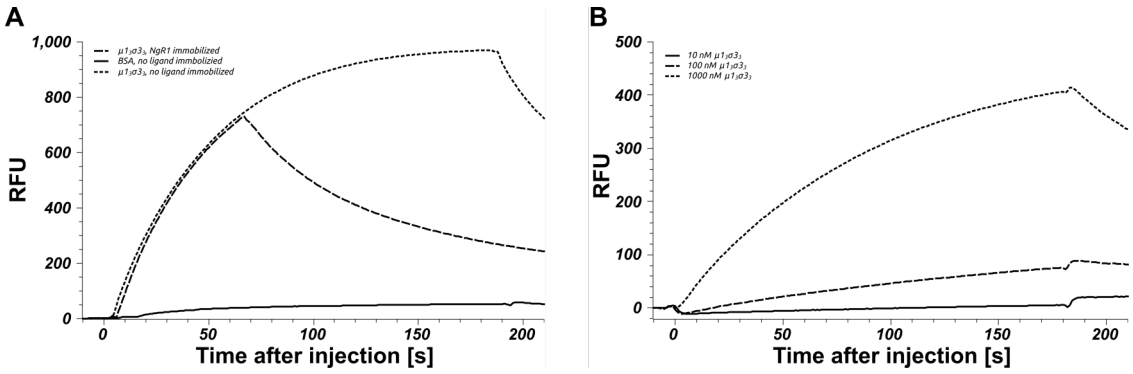

Figure S8) **SPR analysis using NTA Sensor Chip. A:** $\mu 1_3\sigma 3_3$ binds to the NTA Sensor Chip with NgR1-His immobilized (large dashes, 60 s contact time) and without NgR1-His immobilized (small dashes, 180 s contact time), while BSA does not bind to the NTA Sensor chip only (black line, 180 s contact time). **B:** An increasing concentration of $\mu 1_3\sigma 3_3$ results in a signal increase using the NTA Sensor Chip without NgR1-His ligand coupling.

Publications and Unpublished Manuscripts

Publications

Rustmeier, N.H., **Strebl, M.**, and Stehle, T. (2019). *The Symmetry of Viral Sialic Acid Binding Sites - Implications for Antiviral Strategies*. Viruses, 11(10):947. ISSN 1999-4915. doi:10.3390/v11100947

Contributions: The review was designed, written, and visualized by all three authors equally.

Persson, B. D., John, L., Rafie, K., **Strebl, M.**, Frängsmyr, L., Ballmann, M. Z., Mindler K., Havenga, M., Lemckert, A., Stehle, T., Carlson, L.-A., and Arnberg, N. (2021). *Human Species D Adenovirus Hexon Capsid Protein Mediates Cell Entry Through a Direct Interaction with CD46*. Proceedings of The National Academy of Sciences, 118(3):e2020732118. ISSN 0027-8424. doi:10.1073/pnas.2020732118

Contributions: MS purified, crystallized and solved the structure of the HAdV-56 fiber knob together with KM and performed the structural analysis of the fiber knob domain.

Sutherland, D.M., **Strebl, M.**, Koehler, M., Welsh, O. L., Yu, X., Hu, L., dos Santos Natividade, R., Knowlton, J. J., Taylor, G. M., Moreno, R. A., Wörz, P., Lonergan, Z. R., Arvamudhan, P., Guzman-Cardozo, C., Alsteens, D., Wang, Z., Prasad, B. V. V., Stehle, T., Dermody, T. S. (2021). *The Human Neuronal Receptor NgR1 Bridges Reovirus Capsid Proteins to Initiate Infection*. BioRxiv, doi:10.1101/2021.07.23.453469 (this publication is not peer-reviewed, but in preparation for a peer-review journal)

Contributions: MS purified NgR1 together with PW. Furthermore MS performed cryoEM data processing, 3D reconstructions and structural analysis. He contributed the respective parts of the manuscript.

Unpublished Manuscripts

Strebl, M., Caraballo, R., Johansson, E., Persson, D., Bachmann, P., Liaci, A. M., Danskog, K., Arnberg, N., Elofsson, M., Stehle, T. (unpublished). *Structure-guided Design of Trivalent Sialic Acid Inhibitors Improves Potency and Target Range Against Human Adenovirus Infection*

Contributions: MS purified, crystallized and solved the fiber knob-inhibitor complex structures together with PB and AML. He performed the analysis of all structural data and wrote the manuscript with input from RC, EJ, and TS.